HYDROGEN INTERACTIONS IN ZIRCONIUM ALLOYS FOR NUCLEAR APPLICATIONS

A Thesis

by

JOHN CALVIN MARTINEZ

Submitted to the Office of Graduate and Professional Studies of
Texas A&M University
in partial fulfillment of the requirements for the degree of

MASTER OF SCIENCE

Chair of Committee,	Sean McDeavitt
Committee Members,	Lin Shao
	Carl Gagliardi
Head of Department,	Yassin A. Hassan

May 2015

Major Subject: Nuclear Engineering

ABSTRACT

The absorption of hydrogen in zirconium-based nuclear fuel cladding alloys is one of the most significant contributors to its degradation during long-term storage. The goal of this work was to perform a detailed study of the behavior of hydrogen in two zirconium-based alloys used in nuclear applications. Specimens were prepared through low temperature cathodic charging using an electrochemical hydrogen insertion technique. Analysis was carried out through electron microscopy, X-ray diffraction, and differential scanning calorimetry.

The two alloys studied in this work were HANA-4 and Zircaloy-4. The electrochemical charging system was operated at 65 ± 5 °C, using a 0.2 – 0.4 A/cm^2 current density, in a 0.2 M sulfuric acid solution. An electrode of platinum mesh was used as the anode. Specimens were hydrogen charged to 170 wppm, Zircaloy-4, and 1600 wppm, HANA-4. The resulting hydride phases were measured through X-ray diffraction. The observed hydride phases were ε-hydride in HANA-4 and δ-hydride in Zircaloy-4.

Annealing was carried out at 530 °C, 440 °C, and 350 °C on sections of both alloys. The heat treatment resulted in a range of bulk hydrogen concentrations. Differential scanning calorimetry was then utilized to measure the hydride dissolution temperature in each coupon. These measurements however proved inconclusive, as the differential heat flow signals of charged and uncharged samples were difficult to distinguish.

DEDICATION

This work is dedicated to my wonderful wife, Lauren Ashley, my family, my research advisor, Dr. Sean McDeavitt, and to the advancement of scientific knowledge; for the glory of Jesus Christ and the furthering of His kingdom.

ACKNOWLEDGEMENTS

I would like to thank Dr. Sean McDeavitt for bringing me into his research group, for his patience, guidance, and friendship over the course of this project. I also thank Dr. Shao for his help with understanding the behavior of zirconium alloys in a reactor, and for his part in my research committee. Thanks are also due to Dr. Gagliardi, who has been a mentor and a friend, during both my undergraduate work and my graduate studies. Many thanks also go to Dr. Delia Perez, her energy and spirit contributed a great deal to this project, as well as her technical expertise and penchant for understanding manuals that no one else could. I would also like to thank Dr. Luis Ortega for his instruction on running the DSC, as DSC measurements are a significant part of this work. I am also grateful to Dr. Kinnison, without his guidance and support I never would have moved into nuclear engineering. I learned many things from him about working as a professional in a research environment. I also owe a great deal of thanks to Dr. Guilemette for his help, not only with the XRD, BSE, and SE imaging, but for explaining it all to me in great detail. Many thanks go to all my colleagues in the FCML for their encouragement, advice, and friendship. Special mention must be given to Ryan Brito, Daniel Custead, and Justin Peters, all of whom participated in this work as undergraduates. My utmost gratitude goes to my wife, Lauren, for her loving support and encouragement in the most difficult times; I would not have made it without her. While the sample designation LAE officially stands for Lead Anode Electrolysis, the acronym was taken from her maiden name. And finally, I would like to thank my parents for all the many things they have done for me, enabling me to reach this point. I am especially grateful for my father's assistance in the design and construction of the level control system employed for the last series of hydrogen charging runs. And I am most grateful for funding from the Department of Energy, through the NEUP-IRP Program.

NOMENCLATURE

BCC	Body Centered Cubic
BSE	Back Scattered Electron
DHC	Delayed Hydride Cracking
DC	Direct Current
DSC	Differential Scanning Calorimetry
EAN	Electrolysis-Acid-No Thermal Gradient
EOL	End of Life
FAST	Fuel Aging, Storage, and Transportation
HANA	High-performance Alloy for Nuclear Applications
HBF	High Burnup Fuel
HCP	Hexagonal Close Packed
HDT	Hydride Dissolution Temperature
HTC	High Temperature Cathodic-Charging
HZrH	Zirconium Hydride in HANA-4
HTSS	HANA-4 TSS
IRP	Integrated Research Program
LAE	Lead-Anode-Electrolysis
LCS	Low-Temperature Cathodic-Charging System
MDC^2	Materials Development and Characterization Center
MST	Maximum Slope Temperature

NRC	Nuclear Regulatory Commission
PCT	Peak Cladding Temperature
PT	Peak Temperature
SE	Secondary Electron
SIMS	Secondary Ion Mass Spectrometry
SNF	Spent Nuclear Fuel
SRNL	Savanah River National Laboratory
TSS	Terminal Solid Solubility
TSS_d	Terminal Solid Solubility for Dissolution
TSS_p	Terminal Solid Solubility for Precipitation
UHP-Ar	Ultra High Purity Argon
wppm	Weight Parts Per Million
XRD	X-ray Diffraction
Zr4H	Designation for Zircaloy-4 samples during charging
ZTSS	Zircaloy-4 TSS

TABLE OF CONTENTS

Page

LIST OF FIGURES

FIGURE Page

FIGURE Page

LIST OF TABLES

TABLE Page

CHAPTER I

INTRODUCTION

Zirconium alloys have a crucial function in the nuclear power industry. Due to the high corrosion resistance and favorable neutronic properties of zirconium alloys, they have been widely employed as cladding for fuel in light water and heavy water nuclear reactors [1]. The cladding is the first containment barrier in reactor design. It holds the fuel in place, within the fuel bundles that make up the core, and confines fission products within the fuel. Criticality in a reactor is a function of materials and geometry. Thus, the geometric stability of the fuel, provided by the cladding, is an important part of criticality control. The cladding; therefore, performs an important role in the complete life cycle of nuclear fuel. The performance of zirconium based cladding alloys has been the subject of much investigation over the years [1-6]. Performance issues range from corrosion and degradation of mechanical properties during burnup to hydrogen embrittlement and delayed hydride cracking during post irradiation storage. To address these issues, new cladding alloys and fabrication techniques are being developed to extend the service life of the fuel cladding [7-9]. A partial list, of zirconium cladding alloys and their compositions, is given in Table 1.1 below.

Table 1.1

Compositions of Various Zirconium Alloys

Alloy	**Sn wt%**	**Fe wt%**	**Cr wt%**	**Nb wt%**	**Ni wt%**	**Mo wt%**	**O wppm**
Zircaloy-2	1.5	0.12	0.1		0.05		1250
Zircaloy-4	1.3	0.2	0.1				1250
Zr-2.5Nb				2.4-2.8			900-1300
Zirlo	1.1	0.1		1.1			1200
M5		0.038		1.0			0.135
Excel	3.8			0.8		0.9	N/A*
E110		0.009		1.0			600
HANA-4	0.4	0.2	0.1	1.5			N/A**

[7] K.W. Song *et al*, (2008).
[8] D. Khatamian, *et al*,(1995).
[9] M. Billone, *et al*, (2008).
* Not reported in [8] Khatamian *et al*, (1995)
** The HANA-4 material used in this study was found to contain 1000 wppm O.
*** wppm: Parts per million by weight, equivalently μg/g.

To further the understanding of the impact of hydrogen on zirconium and its alloys, the zirconium alloys HANA-4 and Zircaloy-4 were employed in the experiments performed in this study. The work was funded by the Department of Energy and conducted as part of the Fuel Aging and Transportation (FAST) Integrated Research Program (IRP).

The HANA-4 alloy is one of six HANA, ‘High-performance Alloy for Nuclear Applications’ alloys being developed at the Korean Atomic Energy Research Institute (KAERI) in South Korea. HANA-4 is being developed as part of a national research program to develop materials for high burnup fuel (HBF) [7]. Zircaloy-4 is an established alloy and has been used for many years in pressurized light-water reactors (PWRs) [10]. It was developed through a nuclear technology research and development program by the U.S. Navy [10, 11].

The objectives of this research are particularly concerned with the impacts of hydrogen on zirconium alloys used in nuclear applications. Hydrogen absorption is one of the most significant contributors to the degradation of the cladding throughout its service lifetime. Hydrogen is absorbed by zirconium through corrosion. The oxidation of the cladding in water evolves hydrogen, a fraction of which is absorbed by the cladding. Hydrogen has a low solubility in zirconium, only about 1 wppm (wppm: Parts per million by weight, equivalently μg/g) at room temperature and ~200 wppm at 400 °C [12]. When the absorbed hydrogen exceeds the solubility limit, excess hydrogen precipitates as a second phase, zirconium hydride. Hydrogen accumulates in the cladding during burnup, with bulk hydrogen concentrations reaching between 350 and 800 wppm in high-burnup fuel [5]. High burnup is the term applied to fuel assemblies with burnup greater than 45 GWd/MTU [5], where GWd/MTU is a unit of energy released per metric ton of uranium in the fuel. At reactor operating temperatures 250 – 300 °C for CANDU [13], 285 °C for BWR, and 275 - 315 °C for PWR, less than 100 wppm of hydrogen can be maintained in solid solution [12, 14]. Therefore, a significant portion of the hydrogen in high burnup fuel is precipitated as hydride during in core service. Upon cooling, after removal from the core, nearly all the hydrogen is precipitated as hydride.

The hydride phase is brittle and its presence reduces the ductility and fracture toughness of the cladding [9, 15, 16]. The severity of the embrittlement is increased when hydrides are radially oriented. This makes the dissolution of hydrides a concern, because of the potential reorientation of hydrides upon re-precipitation [16, 17]. The presence of hydrogen in solution or in hydrides can lead to component failure through a process known as delayed hydride cracking (DHC).

Delayed hydride cracking is a below yield stress failure mechanism. It poses a significant threat to the integrity of the cladding. Because DHC results from hydride precipitation at the tip of a crack or flaw, it is directly connected to the terminal solid solubility of hydrogen in the zirconium alloy being considered. As the terminal solid solubility describes the conditions under which hydride dissolution and precipitation occurs, knowledge of the TSS for an alloy is important when considering its susceptibility to DHC [8].

While the terminal solid solubility (TSS) of hydrogen in irradiated and un-irradiated material is known and has been widely reported for many zirconium alloys such as Zircaloy-2, Zircaloy-4, Zr-2.5%Nb, and others [8, 14, 18-20], TSS data is not widely available for the HANA alloys. As several studies have already been made to evaluate other characteristics of HANA-4 and Zircaloy-4: steam oxidation under loss of coolant accident conditions (LOCA) [21], corrosion [22], and creep [7]; one of the goals of this work is to add to this growing evaluation by taking the first step toward measuring the TSS of hydrogen in HANA-4. The corresponding measurements made in Zircaloy-4 enable baseline comparison.

In order to study the impacts of hydrogen at the elevated concentrations found in high burnup fuel, hydrogen was inserted into the zirconium alloy specimens through cathodic charging. Charging resulted in 170 – 220 wppm H in Zircaloy-4, and 800 – 1600 wppm H in the HANA-4 alloy. The sections of the charged specimens were annealed at 540 °C to create uniformly distributed hydrides within these samples. Charged and annealed samples were characterized through electron microscopy and X-ray diffraction (XRD). The XRD measurements showed a change from the high-density ε-hydride (ZrH_2) phase, post charging, to the lower density δ- hydride ($ZrH_{1.66}$) phase, post annealing, in the HANA-4 specimens. The phases measured in the Zircaloy-4 specimens changed from the post charging δ- hydride to α-zirconium in the annealed sample; even though the specimen contained 170 wppm H.

To measure and compare the terminal solid solubility of these two alloys, the hydride dissolution temperature was measured for samples prepared under select annealing conditions. Annealing was carried out at 530 °C, 440 °C, and 350 °C. Measurements of the hydride dissolution temperature in this study were performed using differential scanning calorimetry (DSC), following the work of Khatamian [23] and others [20, 24]. However, these measurements were inconclusive. In uncharged specimens of both alloys, there was a feature in the DSC curve at ~350 °C, making it difficult to measure hydride dissolution in the samples annealed at that temperature. While the high and middle temperature measurements in HANA-4 contained features near the annealing temperatures, 530 °C and 440 °C respectively, the features in the low temperature measurement could not be separated from that mentioned above in the uncharged specimen. In Zircaloy-4 only in the sample annealed at 440 °C was a corresponding feature observed, no features corresponding to the annealing temperature were observed in the highest temperature measurement. In the low temperature measurement, as in HANA-4, no feature near the annealing temperature could be distinguished from the uncharged specimen.

The following chapters provide a more in depth look at relevant background information, the methods employed, and results of this study. Chapter II provides an overview of background information motivating this study. Chapters III and IV discuss the experimental methods and results; with discussion and conclusions given in chapters V and VI.

CHAPTER II

BACKGROUND

Hydrogen absorption is one of the limiting factors on cladding lifetime, due the resulting degradation. This Chapter presents a sequence of discussions describing relevant phenomena and literature that provide the foundation for the work performed here. Section 2.1 describes the hydrogen-zirconium binary phase diagram. Section 2.2 introduces the terminal solid solubility behavior of hydrogen in zirconium. Section 2.3 describes in more detail how hydrogen is absorbed into Zr-based nuclear cladding during normal operation, and Section 2.4 describes laboratory methods of charging zirconium alloys with hydrogen. Sections 2.6 and 2.7 discuss hydrogen embrittlement and hydride reorientation, which leads to delayed hydride cracking, Section 2.8.

2.1 The Hydrogen-Zirconium Binary Phase Diagram

The hydrogen zirconium system has been studied for over 60 years, yet ambiguity remains regarding the nature and formation of certain hydride phases [25-28]. Figure 2.1 shows the Zr-H binary phase diagram, as reported by Zuzek and Abriata, 1990 [28].

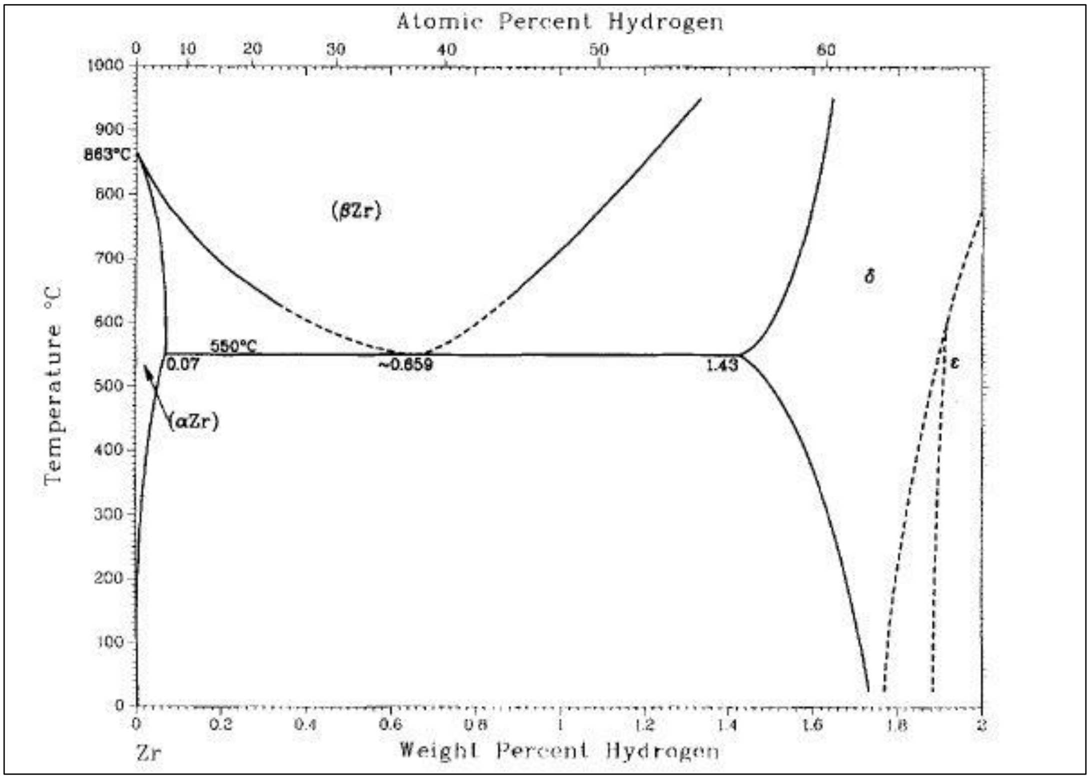

Fig. 2.1 Zr-H Phase Diagram[28].

There are five primary phases in the Zr-H system, see Figure 2.1, in the region from 0 – 1000 °C, and 0 – 2 wt% hydrogen. These are: α-Zr, β-Zr, γ-ZrH, δ-$ZrH_{1.66}$, and ε-ZrH_2 [29]. The γ phase is not shown in the phase diagram because it is considered by many to be a metastable phase [28-30], though some authors argue for its stability as an equilibrium phase[27].

Lanzani [26] suggested that the stability of the γ phase may be dependent on the purity of the zirconium and which alloying elements are present. The δ-hydride is reported to preferentially precipitate in zirconium alloys with elevated concentrations of α stabilizers (e.g., O, Hf, Sn), while the γ-hydride preferentially precipitates in high purity zirconium or alloys containing β stabilizers [26].

The formation of the γ- and ε-hydride phases is proposed to result through martensitic like transformations of the δ-hydride [30]. Unlike diffusionless martensitic transformations, theses transformations require a change in hydrogen concentration [30]. Only the 1 to 1 stoichiometric composition for the γ-hydride (ZrH), is exact, since the δ and ε phases have a broad range of stable stoichiometries [30].

Pure Zirconium in the α-Zr phase has a hexagonal close packed (HCP) crystal structure, and is stable below the β transition temperature, 863 °C [28, 31]. The β phase, is body centered cubic (BCC) and metastable below 863 °C [28, 30]. Certain alloying elements, such as hydrogen and niobium, act as β stabilizers, lowering the β transition temperature and inhibiting decomposition of the β phase [26, 32]. The β-Zr phase is reported to have a greater affinity for hydrogen than α-Zr and an increased terminal solid solubility [32-34]. Higher TSS means more hydrogen can be absorbed before the precipitation of embrittling hydrides, resulting in a longer component lifetime in-core [32].

As described in §2.3, hydrogen absorption by the cladding takes place at elevated temperatures. The hydride phases precipitated in the cladding upon cooling is dependent upon the hydrogen concentration and the rate at which it is cooled [35]. Because higher hydrogen concentrations, and cooling rates less than 10 K/min, lead to preferential precipitation of the δ-hydride phase, the δ-hydride phase is the dominant phase present in the cladding of spent nuclear fuel (SNF) during wet storage [5, 26, 29, 35]. By adopting cooling rates less than 10 K/min, the author was able create the δ-hydride phase in annealed portions of cathodically charged zirconium alloy sections, replicating the dominant hydride phase in SNF.

2.2 Terminal Solid Solubility

The terminal solid solubility (TSS) is an important property of the Zr-H system. Terminal solid solubility represents the phase boundary between dissolved hydrogen in solution and the precipitation of hydrides as a second phase. It is termed the terminal solid solubility because it marks the initiation and termination of the phase transformations mentioned above [36]. The terminal solid solubility of hydrogen in Zircaloy, as measured by DSC, is given below in Figure 2.2.

In the measurement shown below there are two curves. This is because there is a hysteresis between the terminal solid solubility for dissolving hydrides (TSS_d) and precipitating hydrides (TSS_p). The lower curve is the dissolution solvus, and gives the temperature at which all the hydrogen is in solid solution, for a given hydrogen concentration. The upper curve is the precipitation solvus and it denotes the temperature at which hydrogen precipitates to form the hydride phase or phases [36, 37].

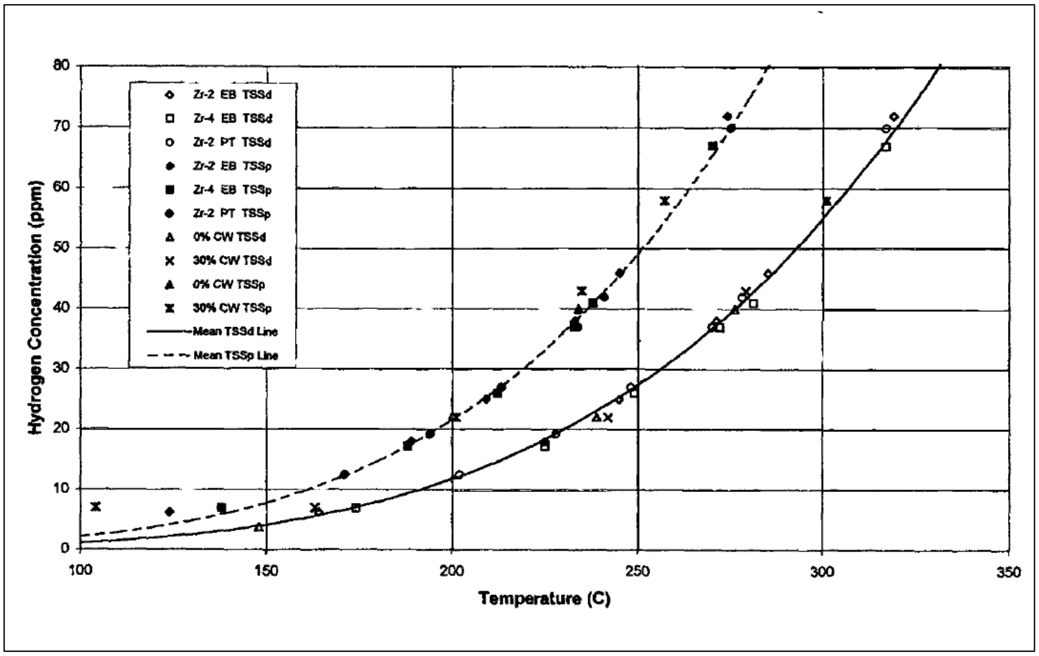

Fig. 2.2 Terminal solid solubility of hydrogen in Zircaloy material. Measured by DSC. Reprinted, with permission from ASTM STP 1354 Zirconium in the Nuclear Industry: Twelfth International Symposium, 100 Barr Harbor Drive, West Conshohocken, PA 19428. [37]

The hysteresis between the solvi is the result of a difference in matrix accommodation energies for precipitating and dissolving hydrides. Because the hydride phases are less dense than α-phase zirconium, there is 17% volume change when α-Zr transforms to δ-hydride. The zirconium matrix must be expanded to accommodate the increase in volume associated with hydride growth [2, 38]. The matrix accommodation energy is the work that must be done expanding the matrix.

The accommodation energy depends on the elastic modulus and the shape of the precipitated hydride. As the yield stress is temperature dependent, the matrix accommodation energy is also temperature dependent [30, 38, 39]. This hysteresis is crucial to observations of crack velocity in delayed hydride cracking [2, 38].

It has been observed that TSS may be impacted by the addition of particular alloying elements [14, 32, 33] and irradiation damage [20]. In assessing the impact of irradiation on TSS, Vizcaino *et al*, [20], reported a significant increase in TSS for Zircaloy-4 irradiated for 10 full effective power years in a heavy water power reactor (HWPR). Une *et al*, [18], reported no change in TSS between un-irradiated Zircaloy-2 and Zircaloy-2 irradiated for 3 – 5 cycles in a commercial boiling water reactor (BWR). Both studies used DSC to measure the TSS in their respective materials; however, the in-core service times differed for the irradiated materials [18, 20].

The variation in TSS between un-alloyed zirconium and the Zircaloys is slight, prompting Kearns [14] to represent TSS for these materials as a single curve, *Eq.* (2.1).

$$TSS_d = 1.2 \times 10^5 e^{-\frac{Q}{RT}} \tag{2.1}$$

$Q = 8550 \frac{Cal}{mol}$ Q is the activation energy.

$R = 1.987 \frac{Cal}{mol \cdot K}$ R is the Universal Gas Constant

$T = Temperature\ in\ K$

Equation (2.1) is referred to as the Kearn's line, and is referenced in many TSS studies [18, 20, 33, 37]. Une *et al* [24] found no difference in TSS between Zircaloy-2 and high Fe (0.26wt%) Zircaloy. However, Khatamian *et al* [8] found that the TSS for the Excel alloy, composition in Table 1.1, was significantly higher than for either Zircaloy-2 or Zr-2.5wt%Nb alloys. This result led to several studies by Khatamian [32-34] to re-evaluate niobium bearing alloys. Khatamian [32-34] reported an increase in the TSS of niobium bearing alloys, finding that niobium increased the TSS by stabilizing the β-Zr phase, which exists as a small fraction in an α + β mix, nominally 90% α and 10% β. Khatamian and Ling [34] reported that the solubility limits of hydrogen in the β phase is two orders of magnitude higher than in α-Zr. Due to its higher solubility, the presence of β phase Zr was found to significantly increase TSS (Figure 2.3) [32-34].

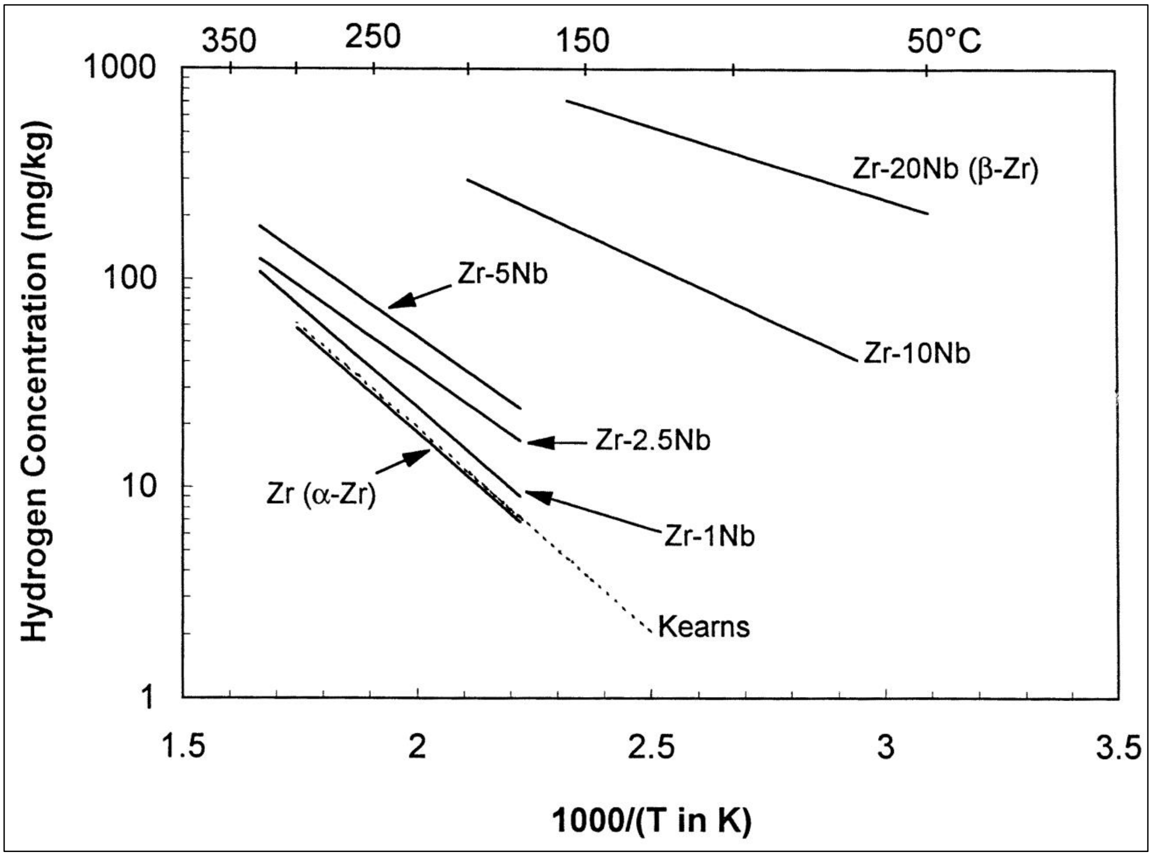

Fig. 2.3 Increase in TSS_d with increasing niobium content in Zr-Nb alloys [32].

Figure 2.3 shows that increasing niobium content results in increased TSS_d. As mentioned in §2.1, the β phase is metastable below 900 K. Khatamian and Ling [33, 34] found that the TSS decreased as the fraction of BCC β phase transformed back to the HCP α phase by aging at 400 – 500 °C for 1 – 100 hrs, Figure 2.4 [33, 34].

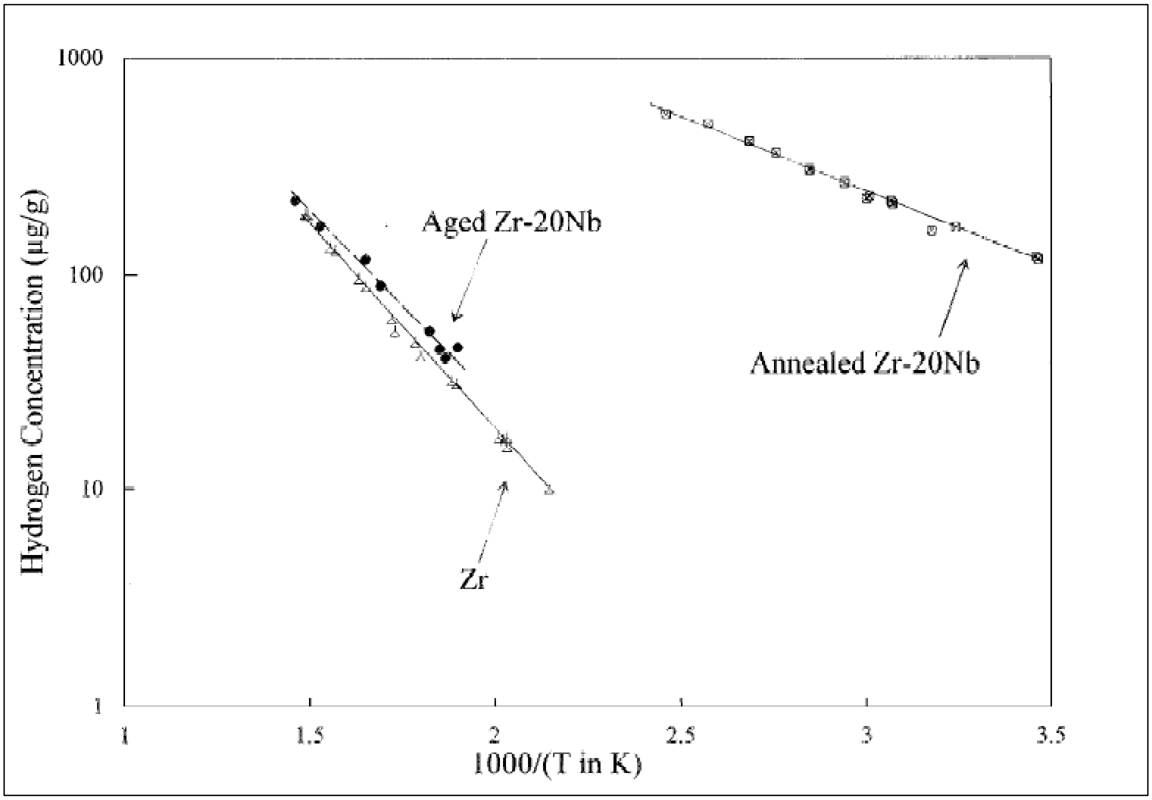

Fig 2.4 Change in TSS for Zr-20Nb with β-Zr fraction. Annealed, fully regenerated β-phase. Aged, fully decomposed to α phase [34].

Figure 2.4 shows that the TSS for Zr-20Nb approaches that of pure zirconium as aging decomposes the β phase to α-Zr. This is why the Zircaloys, in which only the α-Zr phase is present, retain a TSS equivalent to that of unalloyed α zirconium [5, 33, 34]. The niobium stabilization of the β-Zr phase raises the TSS in Zr-Nb alloys by partitioning the hydrogen into the β phase, with its greater hydrogen solubility limit.

As the TSS of different alloys may vary, due to its dependence on crystal structure and alloying elements, it is essential that an alloys TSS be known, in order to know the conditions under which hydride dissolution and precipitation occur [8, 14, 40].

2.3 Hydrogen Absorption During Reactor Operation

As noted in Chapter I, the corrosion of zirconium alloy components during reactor operation is a critical performance-limiting phenomenon. The extreme harshness of the in-core environment poses significant challenges to cladding performance. The performance degradation during irradiation negatively impact the integrity of the cladding and its post irradiation performance in wet and dry storage. The severity of degradation to cladding integrity is closely related the level of burnup in the fuel [5].

The mechanical properties of the cladding are influenced by the absorption of hydrogen into the cladding through corrosion; which can be represented as a function of burnup [22, 41]. On the waterside of the cladding, corrosion occurs primarily in the form of oxidation: $2H_2O + Zr \rightarrow ZrO_2 + 4H$ [12, 41]. See Figure 2.5.

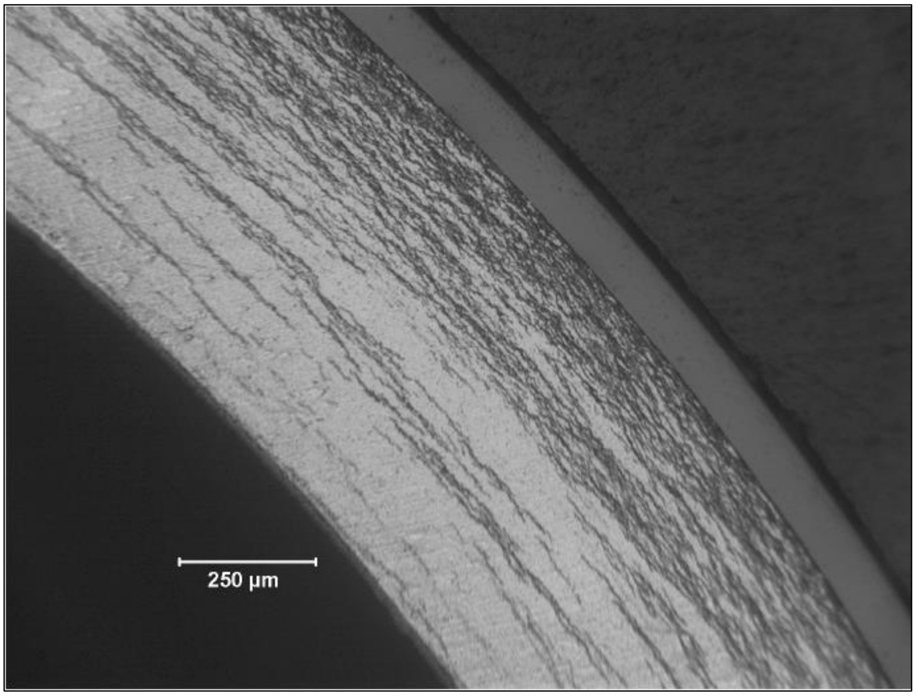

Fig. 2.5 Example of hydrogen absorption during aqueous corrosion: 740 wppm H [9].

During the waterside-oxidation process, a thick oxide layer forms on the outer surface of the cladding, dark region in Figure 2.5. A portion of the evolved hydrogen is absorbed into the cladding and diffuses under the influence of stress and thermal gradients. In Figure 2.5, the absorbed hydrogen has precipitated to form circumferential hydrides. The majority of the hydrides have precipitated near the outer surface, but hydrides are present throughout the specimen. The evolved hydrogen, not absorbed by the cladding, is carried away by the coolant [9].

The ratio of hydrogen absorbed to total hydrogen evolved during the oxidation process is called the hydrogen pickup fraction [12]. The hydrogen pickup fraction depends on alloying constituents and fabrication methods [9, 42]. When the amount of hydrogen absorbed by the cladding exceeds the precipitation solvus, zirconium hydride is precipitated as a second phase [29, 35, 43, 44]. In order to limit hydrogen uptake by the fuel cladding, the Nuclear Regulatory Commission (NRC) limits total cladding oxidation to 0.17 times the total cladding thickness before oxidation (10 CFR 50). However, within these limits, high burnup fuel accumulates between 350 wppm and 800 wppm H, leading to hydrogen embrittlement and the potential for component failure through delayed hydride cracking [5].

2.4 Methods of Charging Zirconium Alloys with Hydrogen

Zirconium alloys typically have a small amount of hydrogen impurities after fabrication. The amount of hydrogen varies by alloy. Some Zircaloy-4 alloys have around 20 wppm hydrogen [45]; while other alloys, such as HANA-4, typically have less than 10 wppm hydrogen after fabrication [21]. These trace amounts of hydrogen have little effect on cladding properties and behavior. Therefore, hydrogen must be inserted into samples, in order to study the elevated hydrogen concentrations seen in cladding at the end of life (EOL) in reactor operation.

There are four methods to insert hydrogen into zirconium reported in literature. These are: cathodic charging, gas phase insertion, aqueous corrosion, and diffusion through a weld from a metal in which hydrogen has a higher activity [12]. As cathodic charging was the method of hydrogen insertion selected for this project; the basic principles of this method are presented in detail below.

Cathodic charging requires simplistic equipment: a reaction vessel, direct current (DC) power supply, and a suitable electrolyte and electrode pair. Cathodic systems for charging zirconium with hydrogen are roughly divided between two categories: low temperature cathodic charging, as seen in Hindle and Slattery [46] and Lepage *et al*, [40], see Figure 2.6, and high temperature cathodic charging systems (HTC), such as those used by John *et al* [47] and Choi *et al* [48].

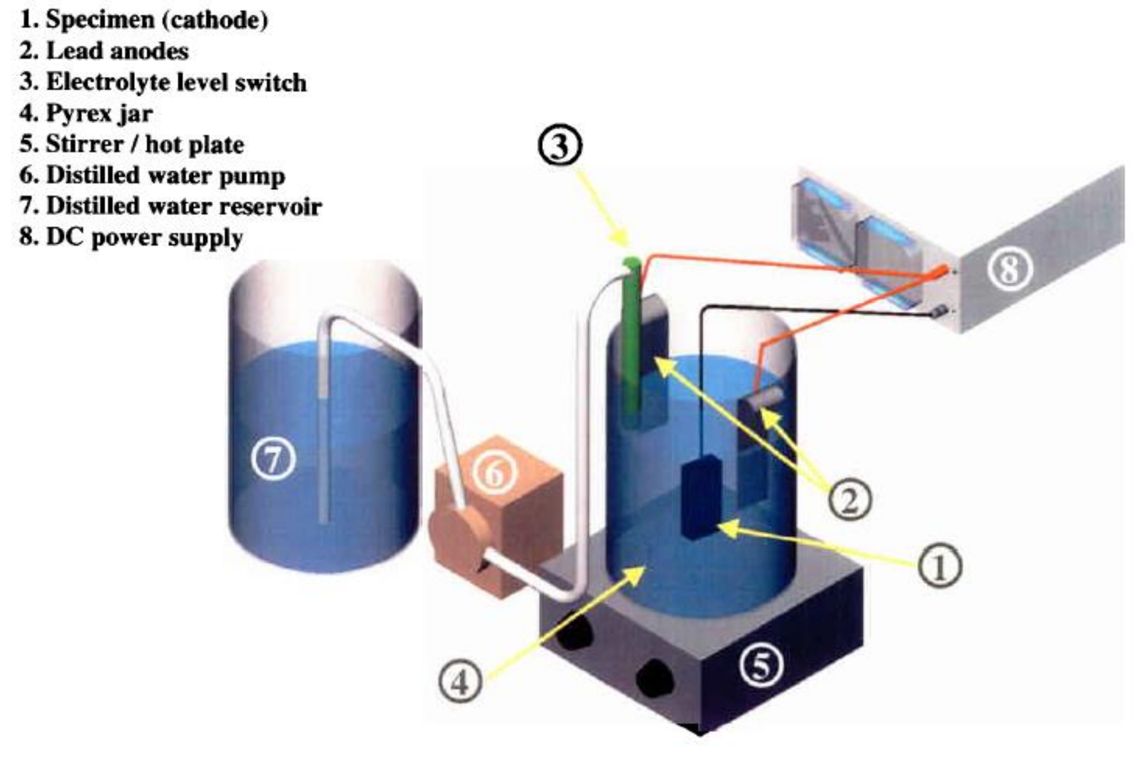

Fig 2.6 System diagram for Low Temperature Cathodic Charging [40].

Low temperature charging takes place below 100 ℃ [40, 46]. A variety of electrolytes can be used in these systems. Sulfuric acid (H_2SO_4) was chosen as the electrolyte in this project, as done in [40, 43, 46]. Potassium-hydroxide (KOH) is another commonly used electrolyte for this purpose [49, 50]. In both cases hydrogen is evolved through the decomposition of water during electrolysis [43]. An example of sample charged through low temperature cathodic charging is presented in Figure 2.7.

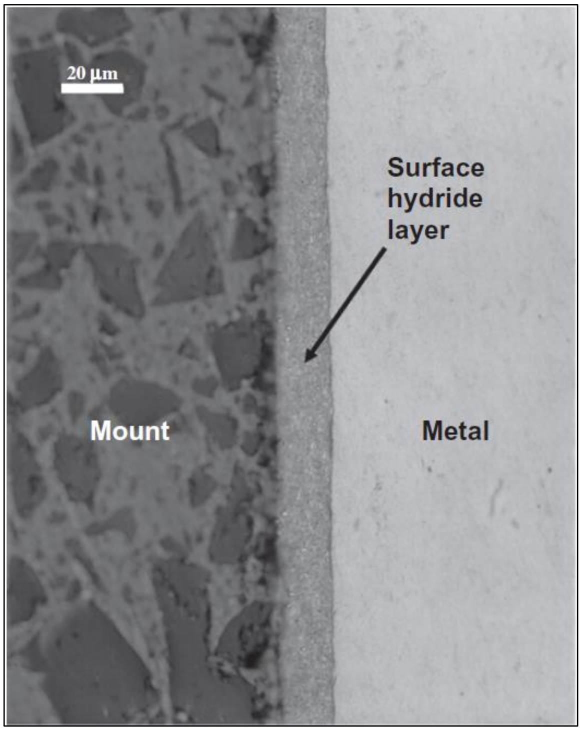

Fig. 2.7 Example of surface hydride layer from low temperature cathodic charging [23]

As seen in Figure 2.7, low temperature cathodic charging results in the creation of a dense surface hydride layer. The hydride concentration in the rim appears uniform.

The HTC process uses an aqueous salt or molten salt electrolyte, with temperatures greater than 250 ℃, see Figure 2.8.

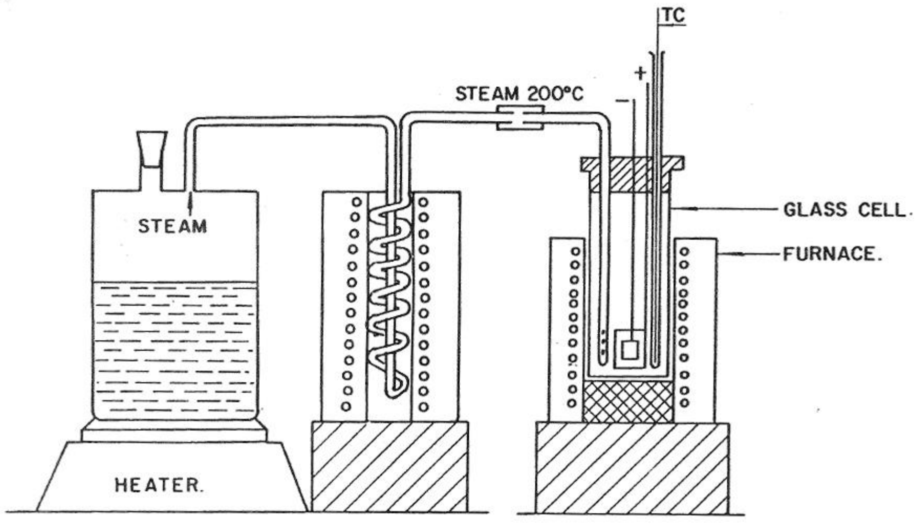

FIG. I.

HIGH TEMPERATURE CATHODIC CHARGING SET UP.

Fig 2.8 System diagram for High Temperature Cathodic Charging [47].

As seen in the diagram above, HTC requires the addition of a steam line and an additional heater [47]. John *et al*, [47] tested nine salt mixtures as electrolytes using potassium sulfate (K_2SO_4), potassium hydrogen sulfate ($KHSO_4$), sodium sulfate (Na_2HSO_4), and sodium hydrogen sulfate ($NaHSO_4$). An example of a specimen charged by high temperature cathodic charging is given in Figure 2.9.

.

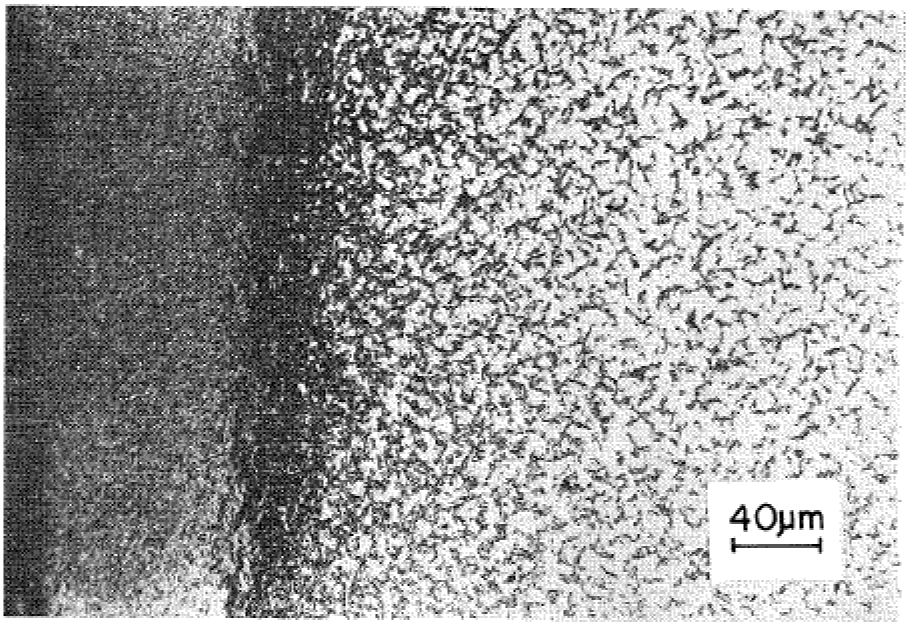

Fig 2.9 Example of surface hydride layer from high temperature cathodic charging [47].

Due to increased hydrogen mobility at the higher operating temperature of high temperature cathodic charging systems, hydrides form well into bulk, far from the surface. This results in a hydride concentration gradient, and hydrides being precipitated in a less localized manner than seen in specimens charged at lower temperature.

Equation (2.2), from Lepege *et al*, [40] gives the minimum thickness of the hydride rim required to produce the desired bulk hydrogen concentration, for a sample of known thickness. It is noted in [40] that if the hydride layer is present on both sides of the sample, only half the thickness per side is required.

$$T_{hydride}(\mu m) = 7.232 \times 10^{-2}\, H_{Zr}\, T_{Zr}(mm) \tag{2.2}$$

$T_{hydride} = Thickness\ of\ the\ hydride\ layer\ in\ \mu m$

$H_{Zr} = hydrogen\ level\ required$

$T_{Zr} = Thickness\ of\ Zirconium\ alloy\ sample\ in\ mm$

Rearranging *Eq.* (2.2), the bulk hydrogen concentration that may be obtained in a sample can be estimated from the observed hydride rim thickness, *Eq.* (2.3).

$$H_{Zr} = \frac{T_{hydride}(\mu m)}{7.232\times10^{-2}(T_{Zr}(mm))} \tag{2.3}$$

The form found in $Eq. (2.3)$ was one method used to estimate bulk hydrogen concentration in charged samples.

In addition to *Eq.* (2.3), hydrogen concentration estimates were made using *Eq.* (2.6). Equation (2.6) is derived from *Eq.* (2.4) and *Eq.* (2.5). This method requires knowing the rim thickness and the hydride phase present in the sample. Equation (2.4) is the definition of wt% for hydrogen. Equation (2.5) approximates the mass of hydrogen based on rim thickness, the volume of the hydrided region, and the density of the hydride phase present in the sample. When combined with *Eq.* (2.4), to form *Eq.* (2.6), it can be seen that the apparent volume dependence drops out, as the hydride volume and zirconium volume have the same length. Thus the volume terms in *Eq.* (2.6) effectively become area fractions.

$$wt\%\ H = \frac{m_H}{m} \tag{2.4}$$

$$= \frac{m_H}{m_{ZrH_x} + m_{Zr}}$$

$$= \frac{m_H}{\rho_{ZrH_x} V_{ZrH_x} + \rho_{Zr} V_{Zr}}$$

$$m_H = x\ \rho_{ZrH_x} V_{ZrH_x} \left(\frac{M_{M_H}}{M_{M_{ZrH_x}}}\right) \tag{2.5}$$

where:

$m = Total\ mass$

$x = Stoichiometric\ factor\ of\ hydride\ phase$

$\rho_{ZrH_x} = Density\ of\ hydride\ phase$

$V_{ZrH_x} = Volume\ of\ hydride\ phase$

$M_{M_H} = Molar\ mass\ hydrogen$

$M_{M_{ZrH_x}} = Molar\ mass\ of\ hydride\ phase$

Thus:

$$H\ wt\% = \frac{x\ \rho_{ZrH_x} V_{ZrH_x} \left(\frac{M_{M_H}}{M_{M_{ZrH_x}}}\right)}{\rho_{ZrH_x} V_{ZrH_x} + \rho_{Zr} V_{Zr}} \tag{2.6}$$

where:

$\rho_{Zr} = Density\ of\ Zirconium$

$V_{Zr} = Volume\ of\ Zirconium$

2.5 Hydride Homogenization

The homogenization process involves annealing the charged sample in a furnace. The annealing time should be sufficient for the hydrogen to approach an equilibrium concentration throughout the specimen. Literature reports annealing in air, an inert atmosphere, or under vacuum [23, 29, 40, 46, 49, 51].

Homogenization is governed by the terminal solid solubility behavior described in §2.2. During heating the hydrides at the rim begin to dissolve as the temperature increases. The hydrides continue to dissolve until the TSS_d at the homogenization temperature is reached. See Figure 2.10.

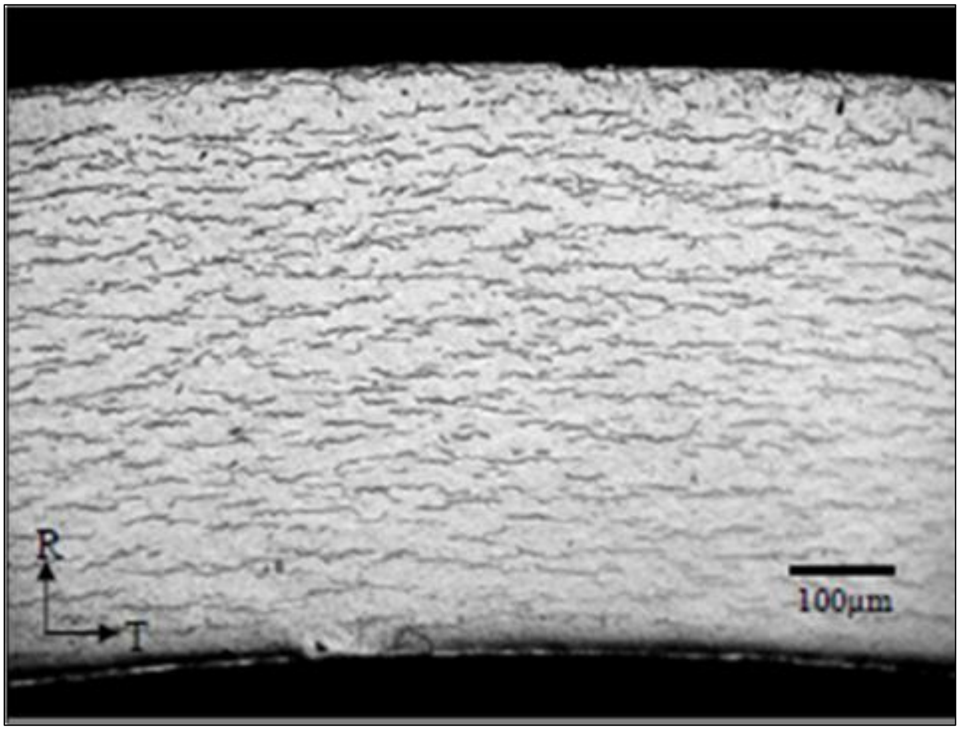

Fig. 2.10 Example of homogenous hydride distribution. (200 wppm H) [3]. Reproduced with permission of the IAEA.

As the hydrogen dissolves into solution, it diffuses throughout the sample; eventually reaching a uniform distribution [52]. Upon cooling this results in the uniform precipitation of hydrides in the sample.

2.6 Hydrogen Embrittlement

The absorption of hydrogen results in a degradation of mechanical properties, known as hydrogen embrittlement. When combined with the potential for hydride assisted cracking (delayed hydride cracking) the cladding is put at risk of failure in reactor operation and extended storage [5, 53].

Hydrogen embrittlement is the degradation of mechanical properties due to the formation of hydrides in the cladding [5]. Embrittlement of Zircaloy or other nuclear cladding increases with burnup as the associated increase in oxidation leads to higher hydrogen content. As noted in Chapter 1, for reactor operating temperatures around 315 °C, less than 100 wppm of hydrogen is soluble. Continued hydrogen absorption creates an increased weigh fraction of zirconium hydride, and increasing embrittlement.

Upon precipitation the zirconium hydride forms platelets with highly textured radial or circumferential orientation, the orientation is related to the internal stress of the cladding tube. An example of circumferential hydrides in cladding is given in Figure 2.11, and radial hydrides are shown in Figure 2.12.

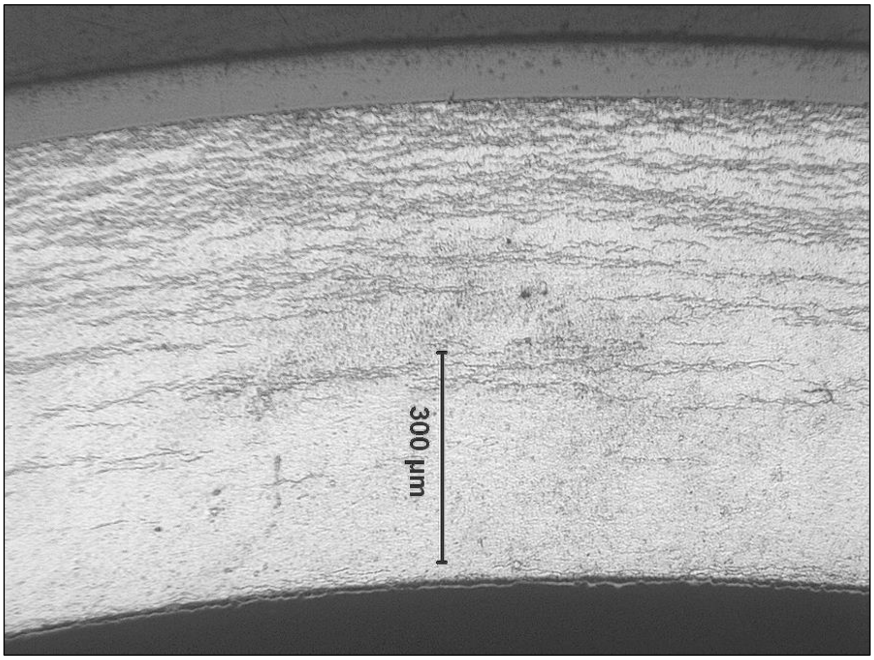

Fig 2.11 Outer oxide layer with a gradient of circumferential hydrides in the bulk [9].

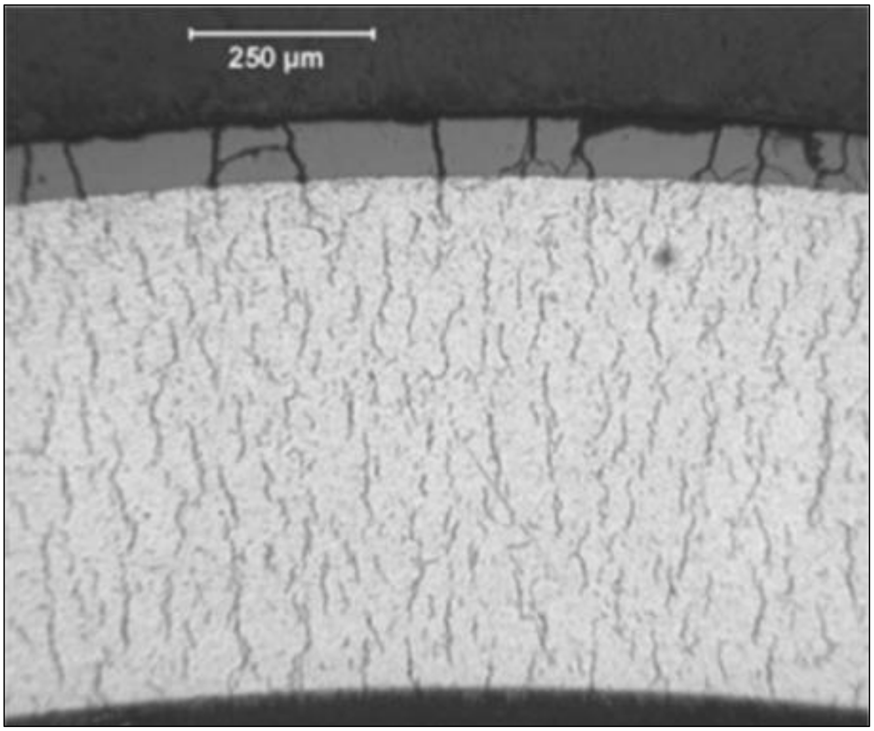

Fig. 2.12 Outer oxide layer with radial hydrides in the bulk [5].

The severity of embrittlement is strongly related to the orientation of the hydrides [16]. Radial hydrides negatively impact the integrity, ductility and fracture toughness of the cladding. The presence of hydrides results in loss of ductility and a rapid decrease in yield strength at temperatures up to 150 °C [54]. These effects are increased at low temperatures, making it a concern during dry storage. The rate of embrittlement increases rapidly at elevated temperatures, making it an important factor in evaluating cladding performance under a postulated loss of coolant accident (LOCA) or during the drying process [5, 9].

The susceptibility of zirconium cladding alloys to hydrogen embrittlement has been reduced by improving their corrosion resistance and controlling the preferred hydride orientation. Corrosion resistance was improved through a combination alloy composition and fabrication techniques [1, 7, 15, 46, 55-57]. Research in the 1960's, showed that the hydride orientation in zirconium alloys is dependent on internal stress, grain structure, and texture[55]. Hindle and Slattery [46] determined that even though tube fabrication processes consist of several steps, the last step is most important for determining the orientation of precipitated hydrides. As a result, current cladding production methods are designed to reduce embrittlement by preferentially precipitating circumferentially oriented hydrides, through control of the texture and residual stress in the material after fabrication [5, 46, 53, 55]. New alloys and techniques continue to be developed to improve the performance and lifetime of cladding alloys for HBF [7, 8].

2.7 Hydride Reorientation

Although cladding fabrication methods directly impacts the preferential precipitation of circumferential hydrides, as discussed in the previous section, a change in the stress field can lead to the reorientation of hydrides [16]. Reorientation occurs when previously precipitated hydrides dissolve back into solution and then re-precipitate under the influence of the current internal tensile stress. Such dissolution is caused by an increase in cladding temperature, which can occur during normal operation, reactor starts and stops, a loss of cooling accident, and during vacuum drying, when fuel is being transferred to dry storage. It has been observed that for hydride reorientation to occur the applied stress must exceed a threshold value [16, 53]. The reorientation stress threshold has been measured for various zirconium alloys to lie between $75MPa - 220MPa$ in the temperature range from 250 – 550 °C. This variation is due to differences in microstructural texture and hydrogen concentration, though may depend on other factors as well [17, 53, 58].

The reorientation process is of particular concern during the fuel drying process. After an extended storage period in a spent fuel pool, fuel assemblies are moved from the wet condition, placed in a dry storage canister (still underwater), which is then sealed and drained. The canister then undergoes several cycles of evacuation and backfilling with high purity argon gas.

At the time of transfer and drying, nearly all the hydrogen in the cladding will be in the form of circumferential hydrides [1]. The evacuation of the canister leads to a rise in cladding temperature due to residual decay heat in the fuel. Because evacuation removes convection as a means of heat transfer, it is physically possible for the decay heat to raise the cladding temperature above 450 ℃ [5]. This would cause a significant portion of hydrogen, about 300 wppm in Zircaloys, to dissolve back into solution [58]. Hydrogen dissolved upon heating is available to re-precipitate as radial hydrides upon subsequent cooling. The drying process also changes the internal stress state of the cladding, Figure 2.13.

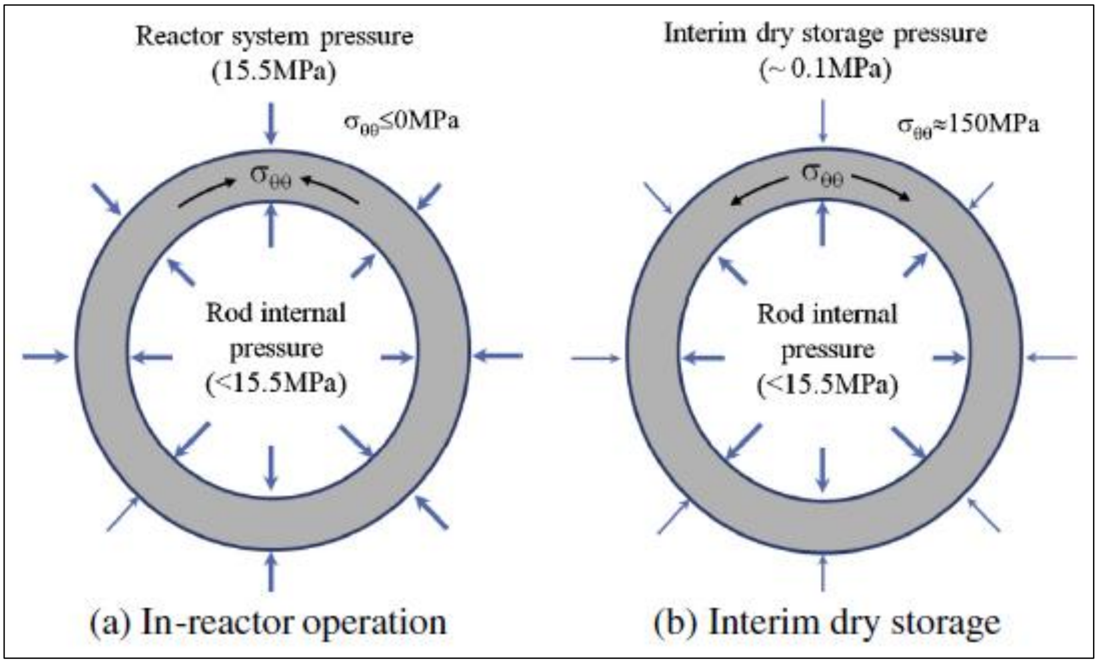

Fig 2.13 Change in cladding stress state from compressive to tensile hoop stress [17].

Figure 2.13 illustrates that, while in the reactor core and during wet storage, external pressure balances the internal pressure in the fuel rod, and the cladding retains its compressive hoop stress. When the canister is evacuated the internal rod pressure exerts a tensile hoop stress on the cladding. Upon cooling, hydrides precipitate such that the platelet normal is aligned parallel to the internal tensile stress as radial hydrides [16, 17, 58]. Thus re-precipitation during the drying process puts the cladding at significant risk of forming radial hydrides and suffering severe embrittlement. To reduce the potential for embrittlement, the Nuclear Regulatory Commission (NRC) has established a 400 ℃ limit on peak cladding temperature (PCT) at any point during storage or the drying process [5, 59],

2.8 Delayed Hydride Cracking

As noted above, used nuclear fuel cladding becomes embrittled by zirconium hydride formation. As the fuel assemblies are moved into dry storage, the drying process has the potential to cause hydride reorientation in response to internal stresses. As the fuel ages in storage, a further challenge arises as hydrogen may continue to migrate within the cladding and a phenomenon known as Delayed Hydride Cracking (DHC) becomes operative [2]. As a failure mode, DHC is a below yield strength failure due to stable crack growth through a hydride embrittled region. Delayed hydride cracking has been responsible for several failures of zirconium components within reactors, and is a further concern during interim dry storage [2, 60]. Figure 2.14 illustrates the DHC process.

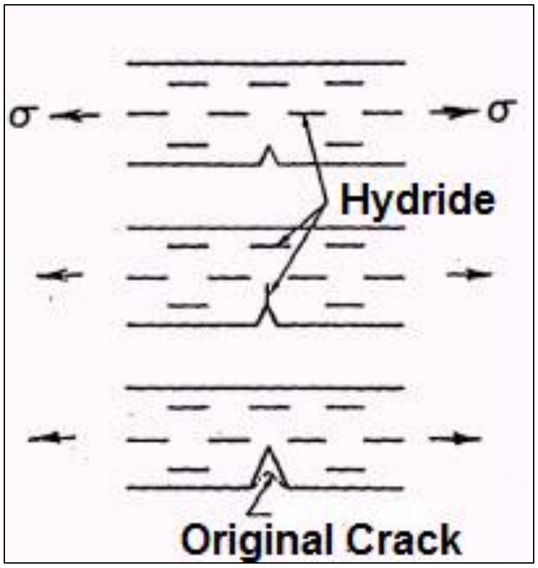

Fig 2.14 Illustration of the DHC process. Begins with a crack or flaw creating a region of high stress intesnsity (top). Brittle hydride precipitates at crack tip (middle). The hydride fractures and the crack grows through the embrittled region (bottom). [2] Reproduced with permission of the IAEA.

2.8.1 Models of Delayed Hydride Cracking

There are two models for the thermodynamic basis of delayed hydride cracking (DHC). The older model, referred to by some, McRae *et al* [60], as the diffusion first model (DFM), was developed by Dutton and Puls in 1975 [61]. Over the years this model has been developed and refined by many authors as more accurate results were obtained for terms affecting the solvus, and other parameters important to modelling DHC [61].

More recently, a new model has been proposed by Kim *et al* [62-65]. This model is referred to in literature as Kim's Model, Kim's New Model, or as the precipitation first model (PFM) [60, 62, 64, 65]. The two models present a different physical basis for DHC and make different predictions about the process through which DHC is begun.

The DFM predicts that the difference in chemical potential for hydrogen, between the stressed and unstressed regions, will result in hydrogen diffusion to the high stress region, to restore the chemical potential to equilibrium. The diffusion of hydrogen to the stressed region raises the local hydrogen concentration at the crack tip until either chemical equilibrium or the precipitation solvus is reached. If the concentration reaches the precipitation solvus, hydrogen precipitates to form hydrides or grow on an existing crack tip hydride, eventually allowing the crack to grow through the embrittled region [60, 61]. A complete derivation of the DFM is given by Puls [39], and a discussion of the DFM with supporting experimental evidence is given by McRae *et al* [60]. The DFM was also extended to cover the case of a thermal gradient by Sagat *et al*, [66].

In the precipitation first model (PFM), proposed by Kim [65], the stress state induces precipitation of hydrides at the crack tip, without raising the hydrogen concentration to the precipitation solvus at the test temperature or lowering the solvus itself [62]. The precipitation of hydrides at the crack tip leads to a lower concentration of hydrogen in solution at the crack tip. This concentration gradient provides the driving force for diffusion of hydrogen from the bulk leading to hydride growth and DHC [62]. It is suggested by Kim that dislocations, generated in the plastic zone of the crack tip assist the precipitation of hydrides, even though the precipitation solvus has not been reached [62]. Kim *et al* has proposed that a transformation from γ hydride, ZrH, to δ

hydride, $ZrH_{1.66}$, may also play a role in creating the concentration gradient between the crack tip and the bulk [64].

These two differing models have been mentioned for completeness, the following description of delayed hydride cracking is given in terms of the diffusion first model, as this model is more prevalent in the literature regarding delayed hydride cracking [2, 60, 66-68].

2.8.2 Description of Delayed Hydride Cracking

Delayed hydride cracking (DHC) begins at an initial crack tip or defect [69]. The stress concentration at the crack tip lowers the chemical potential of hydrogen. The difference in chemical potential between the stressed and unstressed regions drives the diffusion of hydrogen to the crack tip [2, 60-63, 67, 69]. The hydrogen concentration increases at the crack tip, in the stressed region. Under a sufficient stress intensity, the driving force from the chemical potential difference is strong enough to for the hydrogen concentration to reach the precipitation solvus[2]. The precipitation of additional hydrogen, migrating from the bulk, embrittles the region of increased stress-concentration, resulting in fracture upon reaching a critical condition. The critical condition leading to fracture and crack growth is related to the length of the hydride and the applied stress intensity factor. This process is then repeated at the new crack tip [2].

Delayed hydride cracking is a threshold phenomenon, as mentioned above, in order for cracking to occur the stress intensity at the tip of the crack must exceed a threshold value [2, 67]. Once cracking has begun; however, the crack growth rate, or crack velocity, is nearly independent of the stress intensity factor at the crack tip, see Figure 2.15 below [2].

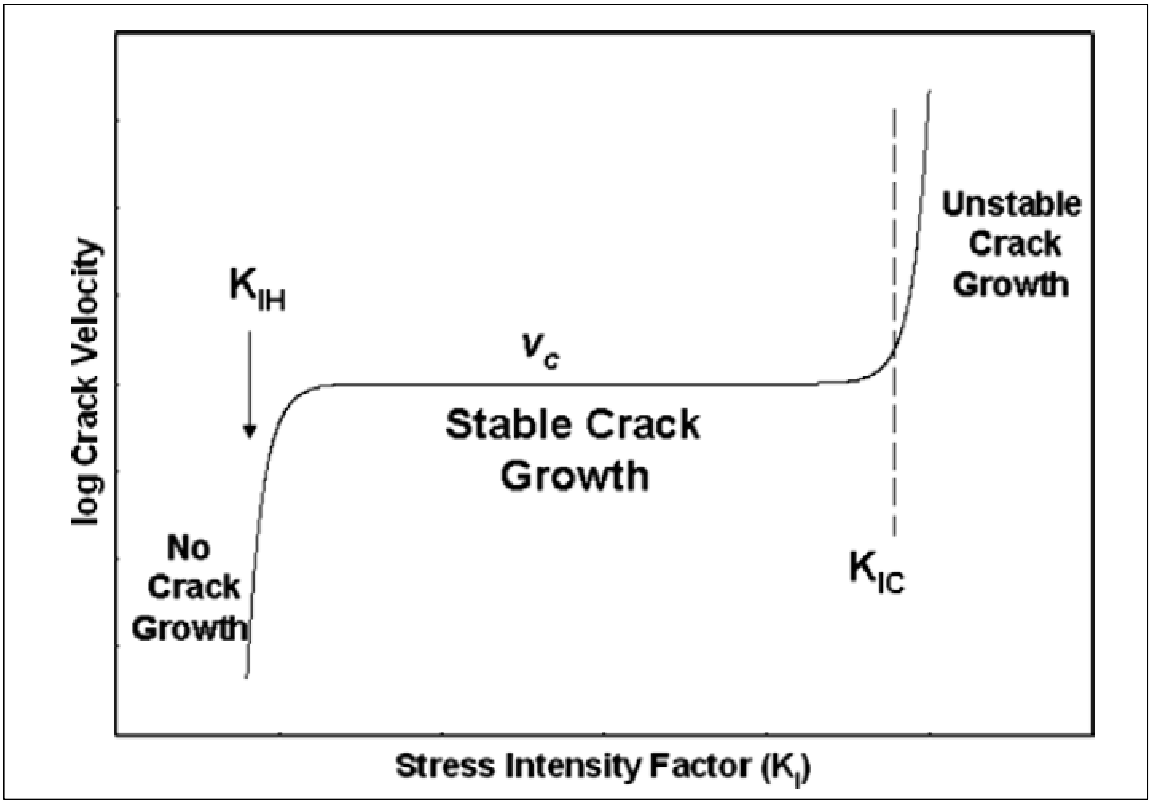

Fig. 2.15 DHC crack velocity dependence on stress intensity. (Fig 2.2 in [2]).

The stress intensity factor is a concept from fracture mechanics used to describe the stress state at a crack tip or flaw. In delayed hydride cracking, the stress is dependent on the solubility of hydrogen in the cladding, temperature, and the yields stress of the material [2, 69]. The embrittlement, caused by the precipitation of hydrides, allows the crack to grow by stages through the embrittled region until it is arrested in the

Zr-matrix [2]. After each fracture the crack holds stable during what is termed ‘the incubation time’. During the incubation time hydrogen diffuses to, and precipitates at, the new crack tip until the hydride reaches the critical length (estimated to be between 1.92 and 5.33 μm) and the fracture repeats [2, 3, 38]. The incubation time is controlled by the rate of hydrogen diffusion, from the bulk, to the crack tip. Equation (2.7) is an analytical equation for the average crack velocity during DHC [2].

$$V = GD_H C_H e^{\frac{V_H^h \Delta p}{RT}} \tag{2.7}$$

Where:

G is a geometric function that includes geometry factors as well as the molar volumes of zirconium and zirconium hydride;

D_H is the diffusion coefficient of hydrogen in zirconium(a function of temperature);

C_H Is the solubility of hydrogen in zirconium in a stress free state;

V_H^h is the partial molar volume of hydrogen in zirconium;

Δp is the difference in hydrostatic tensile stress between the crack tip and the bulk at a distance equal to the characteristic hydride spacing away from the crack tip;

R is the gas constant;

T is the absolute temperature.

2.8.3 Influence of Terminal Solid Solubility

While hydrides provide the mechanism for crack propagation, delayed hydride cracking can occur even when no hydrides are present in the bulk [60]. This is because the hydrogen concentration only needs to locally exceed the solvus at the crack tip for hydrides to form there.

Delayed hydride cracking is a complicated phenomenon with many dependencies, as detailed above. The dependencies on stress intensity, hydride length, hydrogen concentration, and temperature, are all influenced by the nature of the TSS of the hydrogen zirconium system [2, 38, 64, 69].

The hysteresis in TSS curves for precipitating and dissolving hydrides, described in section 2.2, is responsible for the sensitivity of DHC crack velocity to test temperature and direction of approach to test temperature; that is, whether the test temperature is approached by heating or cooling [2, 3, 38, 64]. Measurements of DHC crack velocity have shown that specimens tested at the same temperature will have different crack velocities if they differed in maximum temperature reached during the test [2].This relationship is shown in Figure 2.16.

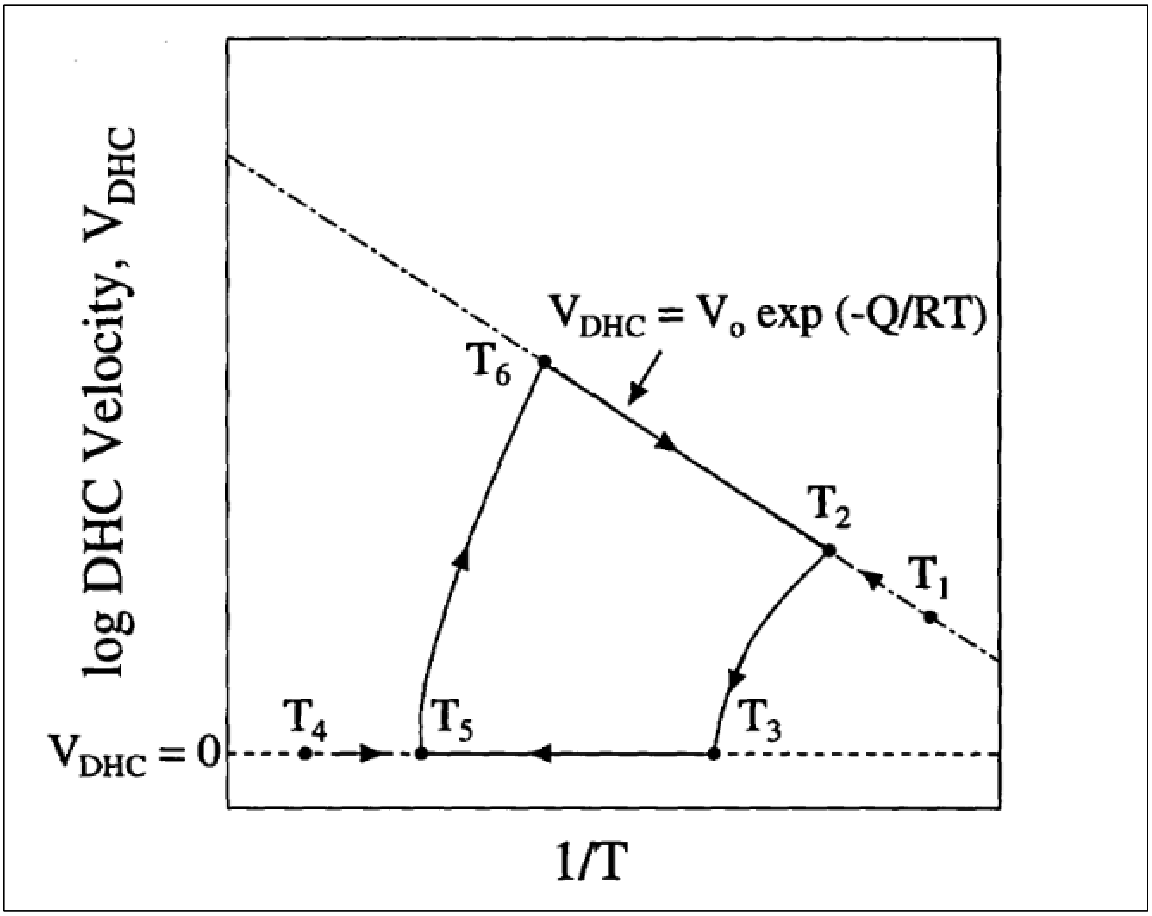

Fig 2.16 The sensitivity of DHC crack velocity to the thermal history [70].

The highest crack velocities are measured, upon cooling, in the specimens with the most hydrogen in solution at the maximum temperature during testing. This is because the crack velocity depends on the amount of hydrogen available to diffuse to the crack tip, and concentration of hydrogen in solution is governed by TSS [2]. What Figure 2.16 shows, is that reaching the test temperature on heating (approaching test temperature from below) results in lower crack velocities than if the test temperature is reached upon cooling (approached from above) [2]. If the crack velocity is measured on heating at successively higher temperatures, then it follows T_1, T_2, T_3, T_4. After T_2 there is insufficient driving force to concentrate hydrogen at the crack tip and precipitate or grow the hydride, so the cracking velocity goes to zero. If the test temperature is approached from above the crack velocity follows T_4, T_5, T_6, T_2. At T_4 all hydrogen is in solution, precipitation cannot occur until the specimen is cooled to near the precipitation solvus. At T_5 the specimen is near enough to the precipitation solvus to precipitate hydrides at the crack tip, and the crack velocity becomes measureable. Cooling from T_4 to T_6 results in the highest crack velocity because the T_6 is very close to the precipitation solvus, increasing the driving force for hydrogen diffusion to the crack tip. At T_6 only a small increase in hydrogen content is required to precipitate hydride at the crack tip [2, 38, 60, 67, 68, 70]. Therefore, accurate knowledge of the TSS is necessary to preclude DHC from occurring under reactor operating conditions [8].

CHAPTER III

EXPERIMENTAL

This chapter describes the materials, equipment, and procedures employed in the conduct of this research. The materials used for this study are described in section 3.1. Section 3.2 describes the cathodic charging system and the modifications made to it over the course of this study. Section 3.3 provides a detailed operating procedure for the cathodic charging system. The equipment and procedure for homogenizing hydrogen in charged specimens is given in section 3.4. Analytical methods used to characterize samples are described in 3.5.

3.1 Materials

Two zirconium alloys were selected for this study: Zircaloy-4 and HANA-4. Zircaloy-4 is a Zr-Sn alloy, and the industry standard cladding for PWR's [3]. Because of this, Zircaloy-4 has been extensively studied [14, 15, 20, 21, 44, 52, 71]. HANA-4 is a newer cladding alloy being developed by the Korean Atomic Energy Research Institute (KAERI) for high burnup fuel applications [7, 56, 72-74]. The designation, HANA, stands for' High-performance Alloy for Nuclear Applications'. HANA-4 is one of six HANA alloys [7, 56, 72]. Unlike the Zircaloys, HANA-4 is Zr-Nb alloy, with small amounts of tin, iron, and chromium. The respective compositions of Zircaloy-4 and HANA-4 are given in Table 3.1.

Table 3.1

Major Alloying Elements of Zircaloy-4 and HANA-4 in wt%.

Alloy	HANA-4		Zircaloy-4	
	Reference[7]	Measured	Reference[15]	Measured
Cr	0.1	0.06	0.07 - 0.13	0.07
Fe	0.1 - 0.2	0.12	0.18 - 0.24	0.12
Nb	1.5	1.47		
Sn	0.4	0.35	1.2 – 1.7	1.32
O	Not Reported	0.10	0.09 – 0.16	0.13
H	~ 7 wppm	0.001	> 0.003	0.001

Measurements of alloy composition performed by IMR Test Labs, 131 Woodsedge Dr. Lansing, NY. 14882.

The measurements of alloy composition were performed by IMR test labs. The composition was measured by a combination of the following techniques: combustion-infrared absorbance, inert gas fusion-thermal conductivity, and inert gas fusion-infrared absorbance. The full reports are provided in Appendix B.

The Zircaloy-4 sheet material was procured as part of the larger research program[1]. A strip was cut from the sheet, and this strip was used to fabricate specimens to be charged with hydrogen and undergo post charging analysis. An illustration of the sample size and geometry is given in Figure 3.1. Measurements were made with a high precision caliper and averaged as a normal distribution to obtain uncertainties.

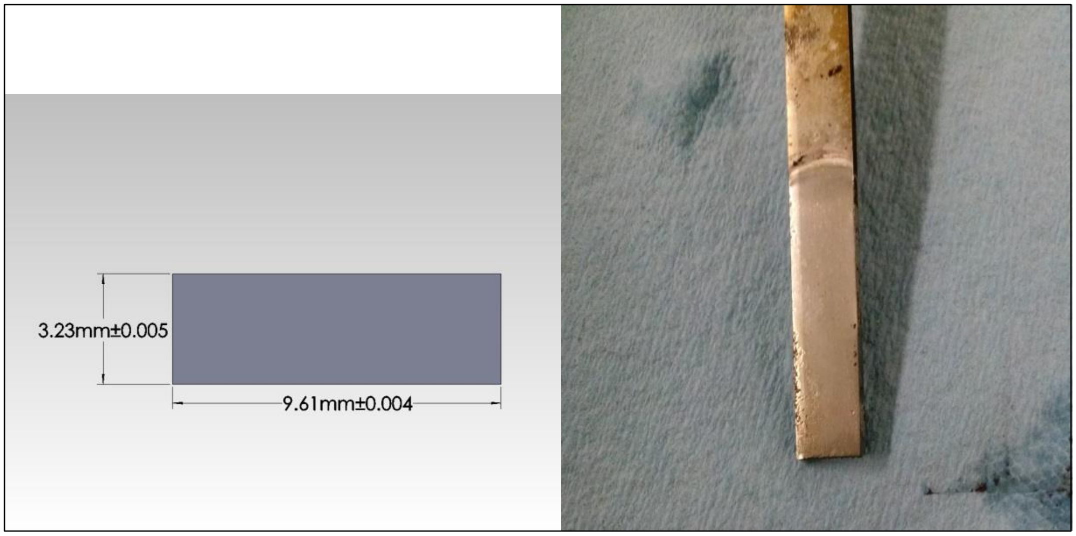

Fig. 3.1 Zircaloy-4 Material. (Left) Dimensions. (Right) Post Charging.

The HANA-4 material was also provided by a member of the larger research program[2] and was received as 30 cm long cladding tubes. The tube dimensions were measured with a high precision caliper and statistically averaged as before. The inner diameter was measured to be 8.20 ± 0.06 mm, and the outer diameter as 9.53 ± 0.01 mm;

---

[1] Purchased by Dr. Yong Yang at the University of Florida.
[2] Received from KAERI through Dr. K.L. Murty at North Carolina State University.

with wall thickness of 0.62 mm. Examples of as received and post charging HANA-4 are shown in Figure 3.2.

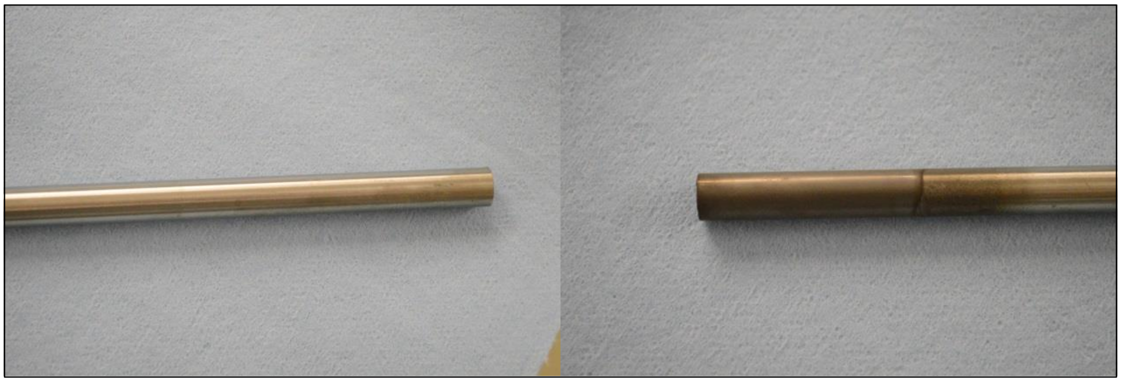

Fig. 3.2 HANA-4 Material. (Left) As Received. (Right) Post Charging 680 $A \cdot h$.

The geometric difference in the form of the as received alloys proved to have a significant impact on attempts at comparison. The solid cross section of the Zircaloy-4 samples resulted in a lower surface area per gram of material. Therefore, hydride rims of a similar thickness correspond to a much lower bulk hydrogen concentration in the Zircaoly-4 specimens as compared to those in HANA-4. The geometric difference impacted the electric potentials (Figure3.3) during charging and the Zircaloy-4 annealing times, as these samples had a longer diffusion path to reach homogenization than the HANA-4 samples.

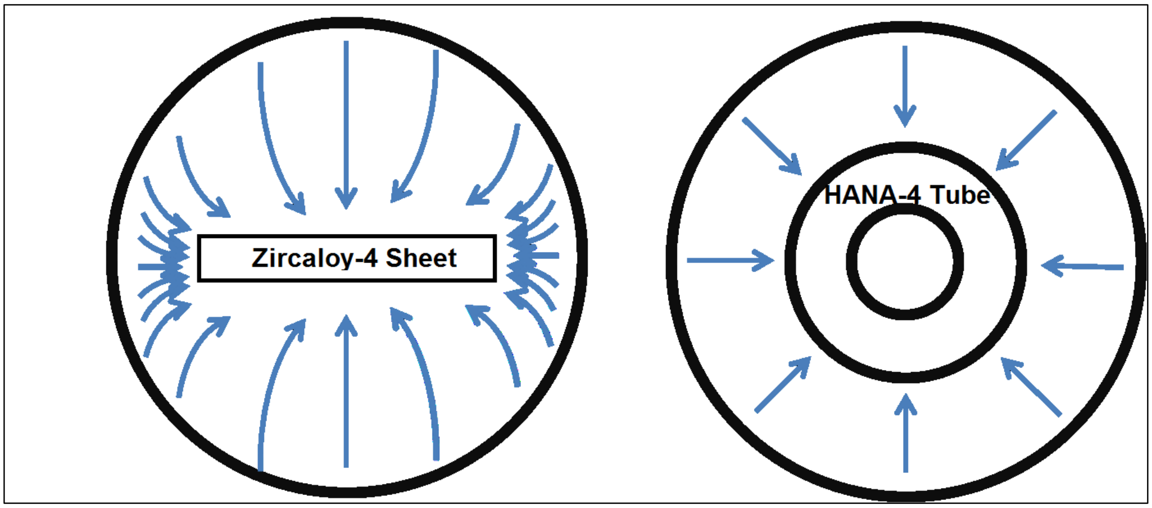

Fig 3.3 Illustration of differences in electric field strength during charging. [75]

Figure 3.3 illustrates the differences between the Zircaloy-4 sheets and HANA-4 tubes during charging.

Specimens were prepared for charging by pickling for 3 minutes in a solution comprised of 50 % H_2O, 45 % HNO_3 and 5 % HF; percentages are by volume. The pickling solution and procedure was taken from Berry *et al* [76]. Pickling was chosen over mechanically cleaning, with 1200 grit emery paper, as suggested by Lepage *et al* [40], because pickled samples have been reported to have a hydriding rate two to four times higher than samples cleaned by grinding [2].

3.2 Cathodic Charging

A number of system configurations were tested based on literature sources by this author. The first design employed in this study was developed by Kuhr [77], and that system was based on work by John *et al*, [47] and Choi, [71].

Electron microscopy and x-ray mapping were employed to assess the effectiveness of this system. Early results showed that the system was not inserting enough hydrogen into the samples to form a visible surface hydride layer; at magnifications up to 2000X. This led to the further modification of this system; which was heavily influenced by Lepage *et al* [40] and Hindle and Slattery[46]. The original system and that used for the principle experiments in this research are described in the following sections.

3.2.1 Initial Cathodic Charging System

The electrochemical hydrogen charging system, developed by Kuhr [77] consisted of a: pyrex reaction vessel, platinum mesh electrode, alumina (Al_2O_3) sample holder, hotplate (with a magnetic stirrer), 10 volt DC power supply, four K-type thermocouples, and an automated data recording system. Figure 3.4. A list of model numbers for commercial components is given in Table 3.2.

Table 3.2

Components of the Cathodic Charging System

Power Supply	TDK-Lambda ZUP 10-80
Hot Plate	SCILOGEX MS7-H550-Pro 7x7
DAQ	Omega OM-USB-TC-AI DAQ

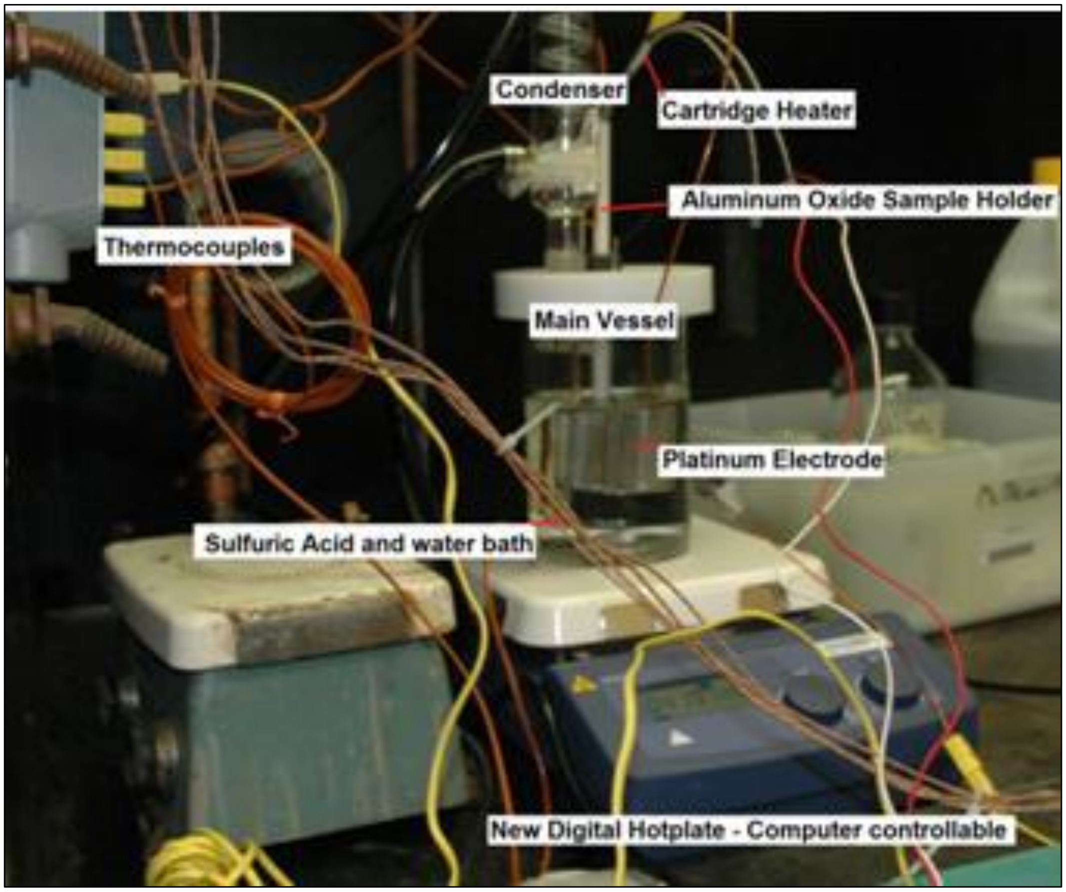

Fig 3.4 Initial cathodic charging system (ECH-TG System). Designed by Kuhr [77]

This setup allowed a cartridge heater to be inserted into the alumina sample holder. This was part of the original work by Kuhr [77], the cartridge heater was not utilized in any experiments in this work. In later experiments by Kuhr [77], an aluminum sleeve was placed between the sample holder and the zirconium alloy sample.

The thermocouples were placed to measure the hotplate, solution, and condenser inlet and outlet temperatures. The four temperature signals and the voltage and current signals from the power supply were recorded by an Omega OM-USB-TC-AI DAQ. The operating parameters and system components were modified due to repeated failure to achieve the desired result.

3.2.2 Final Cathodic Charging System

Initial modifications to the system focused on reducing components in the reaction vessel. The aluminum sleeve, between the sample and sample holder, was removed before the first experiment in this work. Further changes were introduced after several unsuccessful attempts at hydrogen charging.

The final configuration of the hydrogen charging system, Figure 3.5, designated the low-temperature cathodic-charging system (LCS), is shown below.

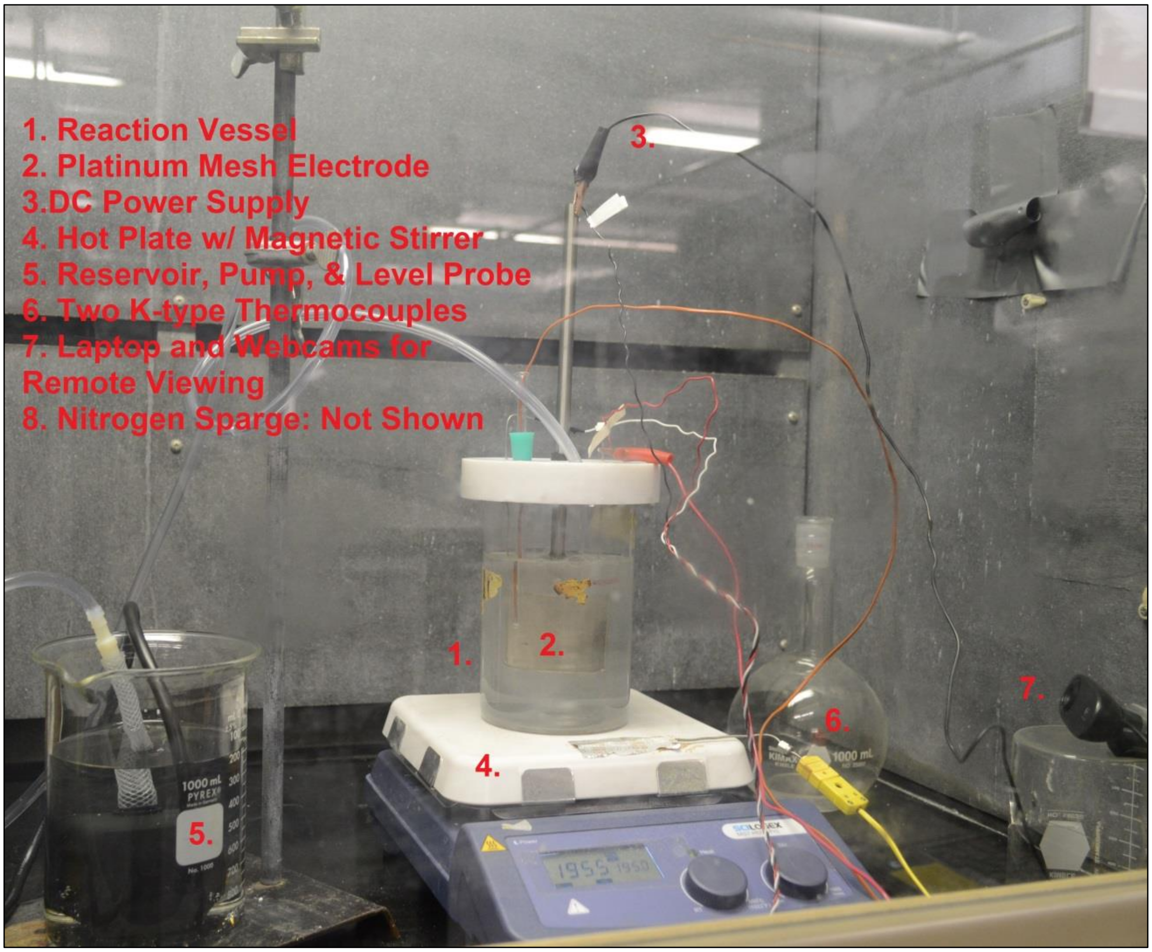

Fig. 3.5 Final cathodic charging system (LCS System).

As shown above, the LCS retained the reaction vessel, platinum mesh electrode, hot plate, and power supply. The other components were replaced or removed. The condenser was replaced with a makeup water supply system, after the system was moved to a fume hood without the necessary plumbing for it. The condenser thermocouples were removed with the condenser, leaving only two thermocouples, which were used to monitor the solution and hot plate temperatures during electrolysis. The aluminum oxide sample holder was removed as a potential barrier to hydrogen insertion. It was also incompatible with the HANA-4 and Zircaloy-4 geometries. A nitrogen gas sparge was added to remove excess oxygen from the solution, prior to electrolysis. The automated data acquisition system was abandoned after the DAQ malfunctioned. Instead, temperatures and voltages were recorded manually.

The makeup water supply system created for this work consisted of a reservoir, pump, and a solid state relay connected to a probe. The relay controlled the pump, turning it on when the probe lost contact with the solution and turning it off when contact was restored. A schematic of the pump controller is provided in Appendix E.

With the removal of the aluminum oxide sample holder it was necessary to modify the connection between the sample and the power supply. Examples of the connection methods used are shown in Figure 3.6.

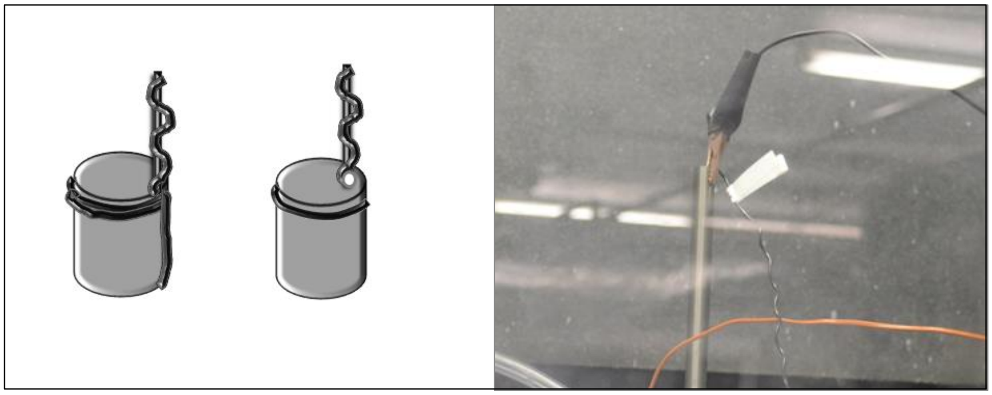

Fig. 3.6 Methods of connecting samples to the power supply.

Initially, the connection between the sample and power supply was established by wrapping a zirconium wire around the specimen to be charged. Pliers were used to twist the zirconium wire, in an attempt to pull it tight against the sample surface. This is illustrated on the far left in Figure 3.6. An effort was made to improve the connection by drilling a hole in the sample tube and passing the wire through before wrapping, illustrated in the middle of Figure 3.6. This proved to be more effective than the first method; however, the absence of the sample holder made it difficult to center the sample within the platinum anode. Both issues were resolved in the final connection method, show at right of Figure 3.6. By using a longer section of sample, the power supply was able to be connected, via an alligator clip, directly to the sample. The sample was held at the desired height inside the reaction vessel by a Viton stopper in the Teflon lid. This enabled good electrical contact between the sample and the power supply, while allowing easy adjustment of the position of the sample with respect to the platinum anode. This method was only used during the charging of the HANA-4 and Zircaloy-4 samples.

The nitrogen sparge was constructed from a piece of stainless steel tubing, closed at one end, with holes drilled in the lower portion of the tube (see Figure 3.7).

Fig. 3.7 Nitrogen sparge.

It was introduced as the result of suspected oxygen contamination of charged samples. Analysis via x-ray mapping of a rim structure on the outer surface of a sample revealed elevated oxygen content in the rim. The presence of oxygen made the nature of the observed structure uncertain. It was suggested by personnel at Savannah River National Laboratory (SRNL) that bubbling nitrogen through the solution before electrolysis may remove excess oxygen from the electrolyte solution. The nitrogen sparge was used for 30 – 60 minutes prior to placing the sample in the electrolyte.

3.3 Operating Conditions

The original operating conditions followed those used by Kuhr [77]. The system employed $50 \text{ wt\%}$ sulfuric acid (H_2SO_4), as the electrolyte, and the solution temperature was set between $85 - 120\ ℃$. The current density was fixed at $0.5 \frac{A}{cm^2}$. Charging times were between 6 – 25 hrs, 20 – 79 A-hrs.

After EAN-7 operating conditions were changed to follow those reported by Lepage *et al* [40]. A 0.2 M sulfuric acid (H_2SO_4) electrolyte, solution temperature 65±5 °C, and current density $0.2 \frac{A}{cm^2}$. Eventually, charging times were increased to greater than 95 hrs, ranging from 95 – 219 hrs, 325 – 680 A-hrs.

Due to some ambiguity regarding what surface area to use for current density calculations, actual current densities varied. For tube specimens, the surface area used was the active surface. Early tests showed hydride formation on both the inner and outer surfaces of tubes, and so the surface area calculations included both surfaces. With the change in connection methods, utilizing the longer tube sections for HANA-4, charging only affected the outer surface. As only the outer surface area was active during charging, in this configuration, the current density was effectively doubled on the active surface. This was discovered post charging, thus the HANA-4 samples were created with an effective current density that was roughly twice the targeted current density. This necessitated an increase in the target current density for the final Zircaloy-4 sample, in order to maintain consistency in charging parameters between HZrH-2 and Zr4H-3.

3.3.1 Cathodic Charging Procedure

System Preparation:

1. Anode Preparation:
    a. Different anodes may be used, preparation may vary.
        i. If using a platinum, Pt, anode, clean the anode by rinsing with ethanol in a sonic bath for 5 minutes, followed by 10 minutes with distilled water in a heated sonic bath.
        ii. If using a lead, Pb, anode; clean Anode surface by removing the surface layer with sand paper or an abrasive flap wheel on a hand drill. (This must be done in the fume hood.)
2. Electronics:
    a. Turn on power supply and hot plate/magnetic-stirrer.
        i. For 65 °C, set the hot plate temperature to 200 °C.
        ii. Temperature may need slight adjustment based on current.
    b. Open Stirrer software, the short cut is named “Stirrer Software” and select the appropriate com port, currently com port 4.
        i. Open remote viewing software, currently TeamViewer 9.0.
3. Nitrogen Tank:
    a. Fill an appropriately sized container with water. Place nitrogen sparge in the container. Ensure all valves on the nitrogen system are closed. Open the main valve (Tank Valve). Then carefully open the regulator valve. When desired nitrogen flow is achieved, close the main valve. The regulator is now set to a safe operating pressure.
4. Electrolyte Solution:
    a. This procedure requires a 0.1-0.2 Molar solution of H_2SO_4. This is achieved by mixing distilled water with concentrated H_2SO_4.
    b. Before mixing, know the concentration of the H_2SO_4 and how to mix a 0.2 Molar solution.
        i. If using 1.0 molar (Equivalent to 2.00 Normality) then the ratio of water to acid is 8 ml H_2O to 2 ml H_2SO_4.
    c. Typically, 600 ml of electrolyte is used.
    d. To mix H_2O and H_2SO_4, pour the required amount of H_2O into the reaction vessel. Next, carefully and slowly add the required amount of H_2SO_4 to the reaction vessel. (The mixing of H_2O and H_2SO_4 is very exothermic.)

   e. Once electrolyte is mixed, insert the nitrogen sparge for 30 – 60 min.
   f. While nitrogen sparge is running, calculate current needed to achieve desired current density over sample surface.
      i. $\rho = \frac{I}{S_{A_{eff}}}$, where $\rho =$ Current Density, $I =$ Current, and $S_{A_{eff}} =$ Effective Surface Area of the Sample.

5. Setting up the Anode:
   a. Turn off and remove nitrogen sparge at this point.
      i. Remove the sparge and place it in a beaker of distilled water.
      ii. Turn on the sparge to clean any fluids out of the line.
      iii. Turn off, dry and store sparge.
   b. If using Platinum
      i. Pass the wire on the Pt anode through the appropriate hole in the lid of the reaction vessel.
      ii. Set position of anode relative to sample.
   c. If using Lead.
      i. The Pb anode, typically 2 – 4 strips of Pb, are placed around the reaction vessel according the marks around its rim.
      ii. Connect the anode strips together, in series, with alligator clips.
   d. Connect anode wire from power supply to the anode.
6. Final Check:
   a. With anodes in place, check that all thermocouples are appropriately positioned.

Sample Preparation:

1. Attach Cathode to Power Supply:
   a. On small samples, this should be done with zirconium wire by spot welding or drilling and tapping with screws to connect the wire to the sample. For a large section, wait till step 4.
2. Cleaning:
   a. Chemical:

        i. Carefully mix 5 ml of HF, 45 ml HNO_3, and 50 ml H_2O in an appropriate plastic container.[3]
        ii. Place sample in solution and wait 3 minutes.
        iii. Remove sample from solution and place in water to quench pickling process.
    b. Manual
        i. Clean sample by removing surface oxide layer with sand paper. Be sure not to heat up sample while removing surface layer, as an increased temperature increases the oxidation rate.
3. Sample is now clean, be careful not to touch or otherwise contaminate sample. Place sample in solution as soon as possible.
4. Once sample is in solution, attach the cathode wire to the power supply.

Run the System by engaging the power supply.

3.4 Homogenization Procedure

In this work, homogenization was carried out in an inert argon atmosphere. Large samples were annealed in a tube heater, contained in an argon atmosphere glove box. Samples to be characterized by DSC were homogenized in a flowing argon environment with a Netzsch 409 STA (simultaneous thermal analysis) unit.

Homogenization times were calculated from $Eq.$ (3.1) provided in Lepage *et al* [40], using hydrogen diffusion data from Kearns [51] *Eq.* (3.2). Equation (3.1) is the solution to the diffusion problem of hydrogen through a plate, of thickness $2L$, with hydride on both surfaces. The solution represented by *Eq.* (3.1) corresponds to a mid-plane concentration that is 97% of the TSS_d [40].

---

[3] HF will dissolve glass/pyrex containers.

$$t = 1.5\frac{L^2}{D} \tag{3.1}$$

$t = Diffusion\ time\ (s)$

$2L = Thickness\ of\ the\ plate\ (cm)$

$D = Diffusion\ Coefficient\ \left(\frac{cm^2}{s}\right)$

The diffusion coefficient used in $Eq.$ (3.2) is the average diffusion coefficient, reported by Kearns [51], for zirconium, Zircaloy-2, and Zircaloy-4. This coefficient was also used for diffusion calculations in HANA-4; diffusion data for HANA-4 was not available.

$$D = D_0 \mathrm{e}^{-\frac{\mathrm{Q}}{\mathrm{RT}}} \tag{3.2}$$

$D = 7.00 \times 10^{-3} \left(\frac{cm^2}{s}\right)$

$Q = 10650\ \left(\frac{cal}{mol}\right)$

$R = 1.987\ \left(\frac{cal}{mol \cdot K}\right)$

$T = Temperature\ (K)$

Samples were annealed four to eight times longer than the calculated homogenization times, in order to assure that the desired homogenization conditions were achieved.

3.5 Characterization Methods

3.5.1 Electron Microscopy: Sample Preparation

The effects of cathodic charging, and subsequent heat treatments, were checked by imaging sections of the treated samples. A combination of back scattered electron (BSE) and secondary electron (SE) microscopy was used for metallographic examination. Optical microscopy was limited to examination of samples during polishing prior to electron imaging.

Electron imaging, BSE/SE, was performed using the CAMECA SX50 electron microprobe in the Department of Geology and Geophysics, at Texas A&M University. This instrument was capable of analysis via x-ray mapping for elements above atomic number 12. Analysis via X-ray mapping led to the discovery of oxide formation on some early samples; which led to the changes in the system described in §3.2.2 Optical imaging was performed using a Hirox KH-1300 digital microscope.

The preparation of samples for metallographic analysis proceeded as follows. Charged Specimens were sectioned, mounted in epoxy, and mechanically polished. Some samples were chemically etched, particularly the annealed samples; as etching reveals the hydrides during imaging. Samples that were examined by electron microscopy required the application of a carbon coating, via sputtering, prior to imaging.

Samples were sectioned with a LECO VC-50 diamond saw, and mounted in a cold set epoxy. Once cut and mounted in epoxy, the sample is ground with silicon-carbide paper through a progression of finer grit [78]. The procedure varied over the project, in an attempt to attain a cleaner polish. However, it nominally consisted of a progression from: 180, 240, 320, 400, 600, and 800 to 1200 grit silicon carbide papers; on the CAMI scale. Each grinding step should take less than 5 minutes [75]. Grinding was followed with rough polishing, using a 3μm diamond suspension on a micro-cloth. The final polish was applied with a 1 μm diamond suspension. It is unnecessary to proceed to a finer polish, as the chemical etching leaves a surface roughness that is on the 1200 scale. Some researchers do not polish beyond 1200 for this reason [79].

The etchant used to prepare samples for metallographic examination was taken from Raynaud [80] and Colas *et al* [53, 79]. The etchant consists of 10 parts H_2O, 10 parts HNO_3, and 1 part HF. The sample is swab etched for 5 seconds, then submerged for 10 seconds. The sample is them removed and immediately washed with cool water.

Measurements of rim thickness were made by recording the length of lines drawn perpendicular to the surface with MS Paint. The average length was determined and multiplied by a conversion factor from pixels to μm, derived from the length of the scale bar.

3.5.2 X-ray Diffraction

Further analysis of as received, post charging, and post annealing material was carried out, via X-ray diffraction (XRD). The system used was a Rigaku Geigerflex Powder X-ray Diffractometer, located in the Department of Geology and Geophysics at

Texas A&M University. The X-ray analysis employed CuKα X-rays. The X-ray beam section is approximately 1 cm^2 and 90% of the diffracted intensity comes from a layer 2–11 μm under a solid flat surface, depending on 2θ.

3.5.3 Differential Scanning Calorimetry

Hydride dissolution measurements were performed via DSC with two different thermal analysis units; the results were inconclusive and often dissolution was not observed, as reported in §4.4. The first instrument, was a Netzsch 409 STA, and the second, was a TA SDT Q600. Both systems are of the heat flux design and both simultaneously carry out DSC and TGA (thermogravimetric analysis) measurements. See Figures 3.8 and 3.9.

A heat flux DSC uses a single furnace. The sample and the reference are maintained in thermal contact, and the respective temperatures and heat flow between them are measured. In a heat flux system, during an exothermic event, the sample temperature is higher than the reference. The sample temperature is being measured against the reference, thus exothermic events result in an increase in sample temperature over the reference and positive difference between the sample and reference temperatures. Thus exothermic events are naturally plotted as positive peaks on a heat flux DSC; though the direction may be changed if the operator desires.

Fig. 3.8 Netzsch 409 STA

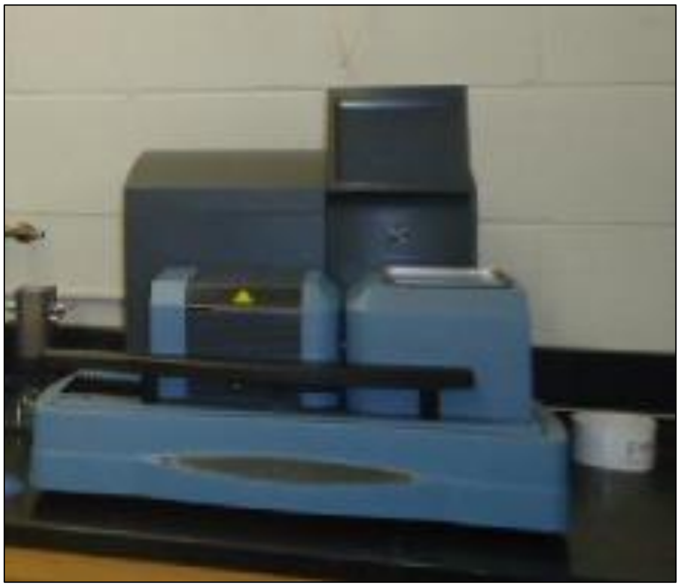

Fig. 3.9 TA Q600 DSC/TGA.

3.5.4 DSC Measurement of the Hydride Dissolution Temperature

When the terminal solid solubility for dissolution (TSS_d) for an alloy is known, specimens of known concentration may be prepared through the following procedure. First, the alloy specimen is cathodically charged until the hydride rim is thick enough to supply the desired hydrogen concentration, after subsequent annealing. The specimen is then annealed at a temperature corresponding to that concentration; taken from TSS_d. Any excess hydrogen, in the rim, is removed by dry grinding with 600 grit paper; after the homogenization step [23, 29, 40]. When the TSS_d is unknown, it can be determined by preparing several samples in the same manner, with a range of homogenization temperatures. The temperatures are selected over the range for which TSS_d is to be measured. Once the samples are prepared, the hydride dissolution temperature (HDT) and corresponding hydrogen contents are measured [8, 20, 23, 24]. Plotting hydrogen concentration (C_H) against HDT, as log C_H vs inverse temperature (1/T), linear regression may be used to determine a best fit for the TSS_d curve [18, 20, 33, 34]. Thus, measuring HDT for HANA-4 and Zircaloy-4, is the first step toward determining TSS for these alloys.

3.5.5 Homogenization for DSC Measurements

Three temperatures, 350 °C, 450 °C, and 540 °C were selected, at which specimens of both alloys would be homogenized. Temperature selection was governed by the desire to study specimens with hydrogen concentrations between 300 and 800 wppm, as this matches the hydrogen content of cladding from high burnup spent nuclear fuel (SNF) [5]. Table 3.3 lists the diffusion parameters, calculated, and actual annealing times used to create samples for hydride dissolution temperature (HDT) measurement.

Table 3.3

Diffusion Parameters and Annealing Times

Sample	T_{Target} °C	$T_{Meas.}$ °C	D cm^2/s	L (cm)	t_c (min)	t (min)
HTSS-1	540	533	9.59×10^{-6}	0.062	15	240
HTSS-2	450	442	4.22×10^{-6}	0.062	25	250
HTSS-3	350	346	1.28×10^{-7}	0.062	75	375
ZTSS-6	540	530	9.59×10^{-6}	0.024	1.5	60
ZTSS-7	450	438	4.22×10^{-6}	0.024	3.4	60
ZTSS-3	350	345	1.28×10^{-7}	0.162	510	2040

After homogenization the specimens are subjected to an appropriate temperature profile in a DSC to measure the HDT. Details of the DSC measurements are given in Chapter 4. Sections for HDT measurements were cut from charged and uncharged specimens of both alloys. Measurements in HANA-4 were given the identification key HTSS, and those in Zircaloy-4 ZTSS.

The sections were cut to fit into the sample cups of the Netzsch 409 STA unit which have a 6 mm diameter. For the HANA-4 alloy, sections were cut from a thin ring of tubing. The Zircaloy-4 sections were cut so as to provide sufficient hydrogen concentration for comparison with the HANA-4 samples.

The samples were sectioned using the diamond saw. Sections of HANA-4 were then straightened, by hammering, to remove curvature. This allowed better contact between the specimen and the STA 409 sample cup. It also aided the uniform removal of residual surface hydride, after homogenization by annealing. The Zircaloy-4 sections were cut in two manners; illustrated in Figure 3.10.

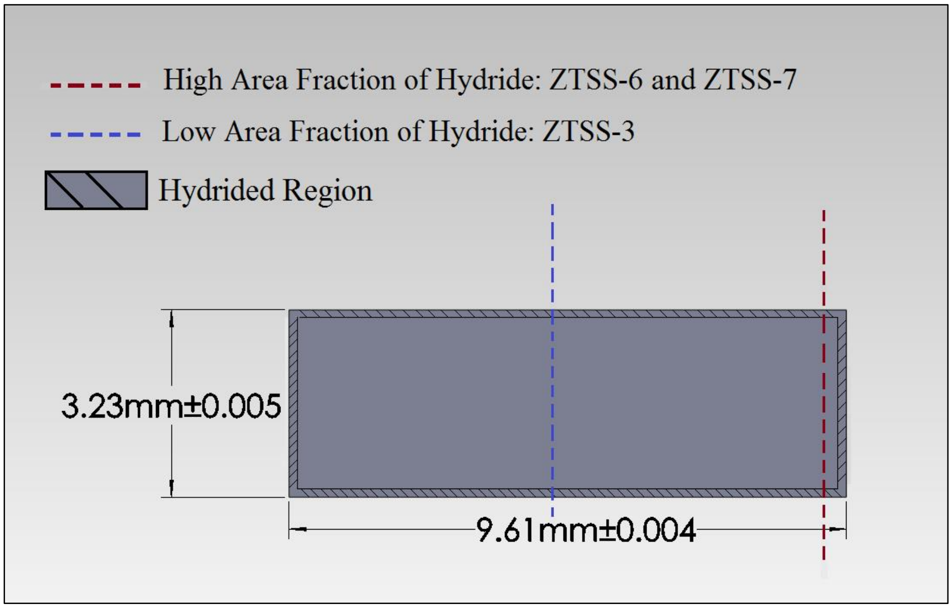

Fig. 3.10 Methods of sectioning Zircaloy-4 for TSS measurements.

Specimen ZTSS-3 was cut from the end of Zr4H-3, cross section shown in Figure 3.10. The blue line in Figure 3.10 shows roughly where ZTSS-3 was cut, to enable it to fit into the DSC sample cups. This method of sectioning limited the potential bulk concentration of the sample to less than the estimated 170 wppm; because, hydride was only present on three of the outer surfaces. This method of cutting has a higher volume fraction of bulk zirconium. However, it was noted that the potential bulk hydrogen in a thin section depends on the thickness (volume fraction) of the hydride rim and the thickness of the specimen. (See *Eq.* (2.3)). The hydride thickness is fixed, post charging. Therefore, in order for a sample to have a higher bulk concentration, the volume fraction of the zirconium must be reduced. Specimens ZTSS-6 and ZTSS-7 were cut down the red line, taking advantage of the observation above. This created a plate with hydride on one side, and by controlling the thickness of the plate the potential bulk concentration was increased to an estimated 860 wppm.

3.5.6 Operating Conditions Netzsch 409 STA

Prior to performing measurements, the Netzsch 409 STA was calibrated for temperature and enthalpy. The calibration was performed using the melting points of six metal standards: indium, tin, bismuth, zinc, aluminum, silver, and gold. The calibration procedure followed the Netzsch Calibration Manual. Prior to calibration, it was necessary to select the operating conditions that would be used during the sample measurements. The purge flow and protective flow rates were selected to match those suggested in the Netzsch operations manual. Vizcaino *et al* [20] reported that heating rates, 5-30° K/min, had negligible impact on the system. However, it was also noted that an increased heating rate, improved signal definition [20, 24]. The choice of heating/cooling rate attempted to balance the sensitivity of the measurement with hydride precipitation kinetics. Therefore, 10 K/min was chosen as the heating/cooling rate. As noted in §2.1, a cooling rate greater than 10 K/min changes the primary hydride precipitate from δ to γ hydride [18, 29, 35]. As δ hydride is the primary hydride phase found in SNF, it was desirable to retain it as the primary phase in the samples [5, 26]. However, other studies have reported heating and cooling rates greater than 10 K/min [20, 23].

The operating conditions used with Netzsch, during annealing and HTD measurements, are given in Table 3.4. Each sample was measured once. Upon completion of this first test series, ZTSS-3 was measured again, with variable heating and cooling rates. Parameters for the HDT measurements with the Netzsch 409 are given in Table 3.5.

Table 3.4

Netzsch 409 STA Operating Conditions

Sample	$\dot{T}$ K/min	Purge Flow	Protective Flow	Gas
HTSS-1-3 ZTSS-6,7, and 3	10	20 mL/min	10 mL/min	UHP-Ar
ZTSS-3 Mk. II	30, 20, 10	20 mL/min	10 mL/min	UHP-Ar

Table 3.5

HDT Measurement Parameters for Netzsch 409

Sample	Mass mg	T_{set} °C	T_{max} °C	T_{anneal} °C	No. Cycles	Reference
HTSS-1	31.9	565	546	533	6	Empty
HTSS-2	29.6	550	532	442	4	Empty
HTSS-3	32.6	550	531	346	4	Empty
ZTSS-6	7.3	565	544	530	4	Empty
ZTSS-7	9.2	500	484	438	4	H free Zircaloy-4
ZTSS-3	38.2	400	401	345	4	Empty
ZTSS-3-Mk II	38.2	400	392	----	6	Empty

3.5.7 Operating Conditions TA SDT Q600

The second series of hydride dissolution temperature (HDT) measurements was performed with a TA Q600 DSC/TGA, at Texas A&M University's Materials Development and Characterization Center (MDC^2). The calibration and operation of the unit was handled by the MDC^2 staff[4]. The heating and cooling rate for these measurements was changed to 20 K/min; following the recommendation of Vizcaino *et al* [20], who reported that the dissolution peak was not observed at 5 °K/min, and was not well defined at 10 K /min. Vizcaino *et al* reported that 20 K/min resulted in a well-

---

[4] Dr. Anup K. Bandyopadhyay

defined dissolution peak. The measurement conditions used with the TA Q600 are given in Table 3.6. These measurements utilized the same samples as the measurements performed with the Netzsch unit. To distinguish between measurements on the different instruments the suffix Q added to sample designations after measurement with the TA Q600.

Table 3.6

HDT Measurement Parameters for TA Q600

Sample	Mass* mg	$T_{Meas.}$ °C	$\dot{T}$ °C/min	No. Cycles	Reference
HTSS-1Q	330.458	545	20	3	Empty
HTSS-2Q	334.851	480	20	3	Empty
HTSS-3Q	331.774	380	20	3	Empty
HTSS-0Q	353.426	480	20	3	Empty
ZTSS-6Q	325.844	545	20	3	Empty
ZTSS-7Q	322.772	480	20	3	Empty
ZTSS-3Q	327.426	380	20	3	Empty
ZTSS-0Q	323.717	480	20	3	Empty

*Mass includes mass of sample cup

CHAPTER IV

RESULTS

Table 4.1

Charging Parameters and Results for all Samples

Experiment	Electrolyte		Current Density	Run Time	Hydride	H
Sample	Temp.	Concentration	$\frac{A}{cm^2}$	$A \cdot h$	μm	$wppm$
EAN-S	120 °C	50 wt % H_2SO_4	0.5	20.10		
EAN-1	120 °C	50 wt % H_2SO_4	0.5	26.43		
EAN-2	120 °C	50 wt % H_2SO_4	0.52	33.60		
EAN-3	120 °C	50 wt % H_2SO_4	0.487	17.46		
EAN-4	120 °C	50 wt % H_2SO_4	0.5	75.20		
EAN-5	85 °C	50 wt % H_2SO_4	0.508	72.94		26**
EAN-6	90 °C	50 wt % H_2SO_4	N/A	*		0
EAN-7	90 °C	50 wt % H_2SO_4	N/A	*		0
EAN-8	65 °C	0.2 M	0.21	79.31		81**
LAE-1	65 °C	0.16 M	0.096	6.49	3.1 ± 0.7	58
LAE-2	65 °C	0.16 M	0.195	8.03	5.8 ± 0.7	109
EAN-9	75-80 °C	0.16 M	0.200	326.80	17	326
ZrH-1	75-80 °C	0.2 M	0.240	340.21	6.3 outer 8.1 inner	270
ZrH-2	75-80 °C	0.2 M	0.240	575.47		0
HZrH-1	65-71 °C	0.2 M	0.387***	342.00	33.8 ± 1.8	754
HZrH-2	65-69 °C	0.2 M	0.387***	679.98	51.2 ± 1.0	1227
Zr4H-1	63-68 °C	0.2 M	0.266	344.72	19.3 ± 1.2	82-110
Zr4H-2	63-68 °C	0.2 M	0.266	>584.4	12.3 ± 0.3	53
Zr4H-3	63-69 °C	0.2 M	0.37	680.21	14.9 ± 1.2	64-85

* Potentiostatic Tests.

** Hydrogen Concentrations Measured at UIUC.

*** The target current density was 0.2 $\frac{A}{cm^2}$.

4.1 Charging System Definition

The first six samples charged in this configuration were EAN-S through EAN-5. The designation EAN stands for, Electrolysis-Acid-No Thermal Gradient. Post charging analysis on these samples showed no indication of a hydride layer being deposited on the sample surface (Figure 4.1).

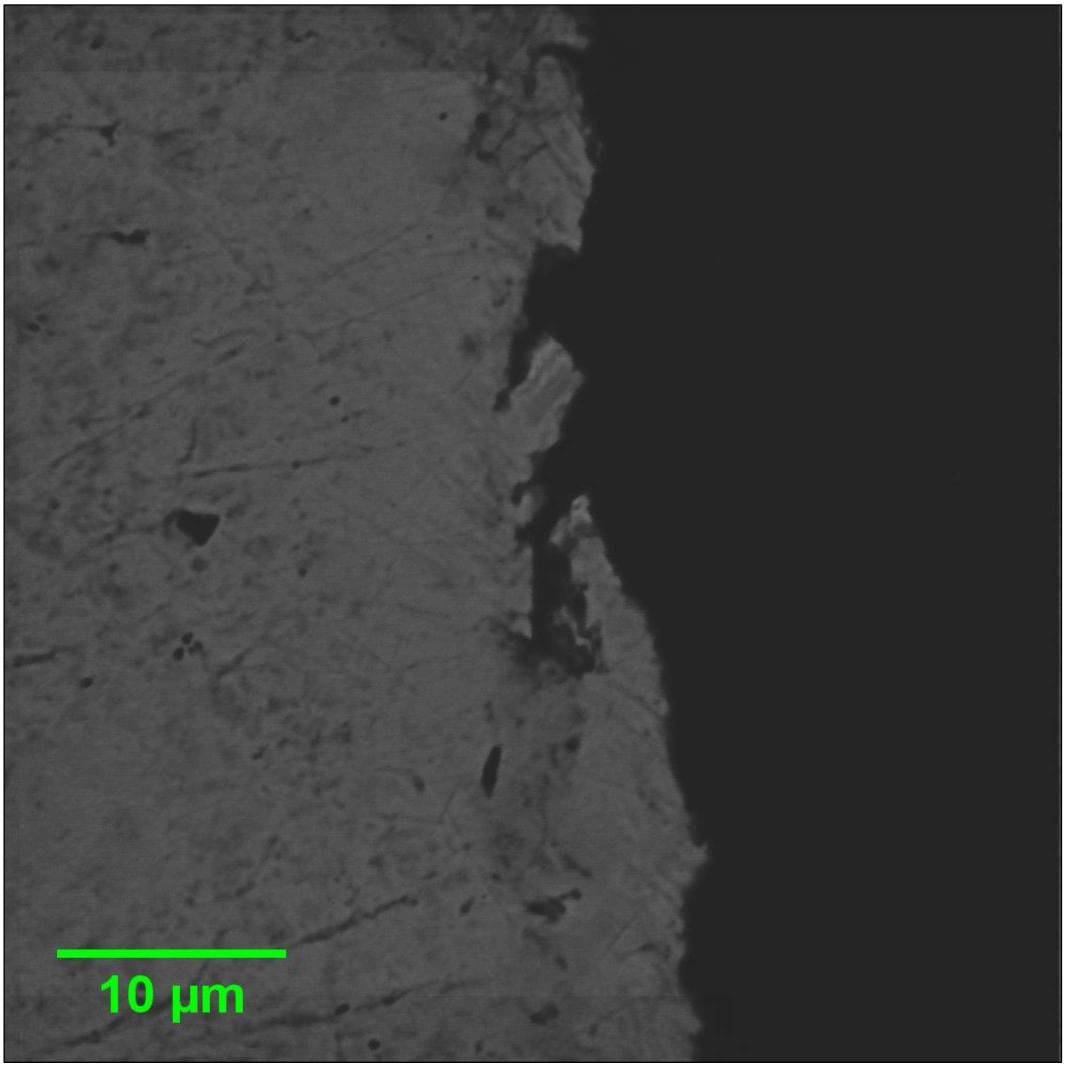

Fig. 4.1 EAN-4: Un-etched micrograph of outer sample surface. 75 A-hrs.

From Table 4.1, sample EAN-4 was charged for 75 A – hrs, at 0.5 A/cm^2, in a 120 °C 50 wt% H_2SO_4. In the above micrograph it is plain that no hydride formation is evident in the rim. After the first six runs proved unsuccessful, two more samples, EAN-6 and EAN7, were run as crude potentiostatitic tests to characterize the relationship of current to voltage in the system, for two different sample holder materials. See Figure 4.2.

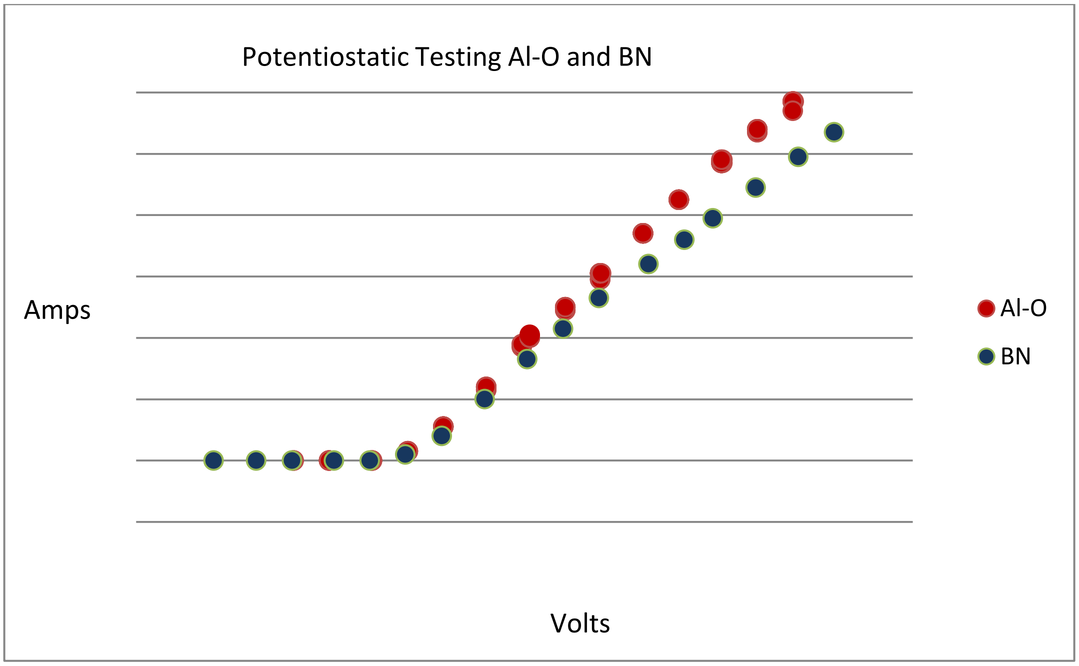

Fig. 4.**2** Potentiostatic testing results.

The two sample holders were made of alumina (Al_2O_3), which was used for all previous samples in the EAN series, and boron-nitride (BN) which was used for some samples in previous work by Kuhr [77]. These tests both terminated in when the current, in excess of 10 amps, caused the zirconium wire connecting the power supply to the sample to fail.

The results indicated that the sample holders were not parasitic to the hydride reaction; which had been considered as a reason for the failure of previous charging runs.

In light of the failure to attain a hydride rim on previous samples, the charging conditions were modified according to Lepage *et al* [40]. In the updated charging procedure the electrolyte concentration was reduced to a $0.2\ M$ sulfuric acid solution, (H_2SO_4), and the solution temperature was reduced to 65 ± 5 ℃; with a target current density of $0.2 \frac{A}{cm^2}$. Two tests were performed under these conditions, LAE-1 and LAE-2, in which strips of lead, Pb, were employed as the anode.

Electron microscopy of these samples hinted at the formation of small hydride rim, less than $6\ \mu m$, which corresponds to an estimated bulk hydrogen concentration of $\sim 110\ wppm$ (Figure 4.3).

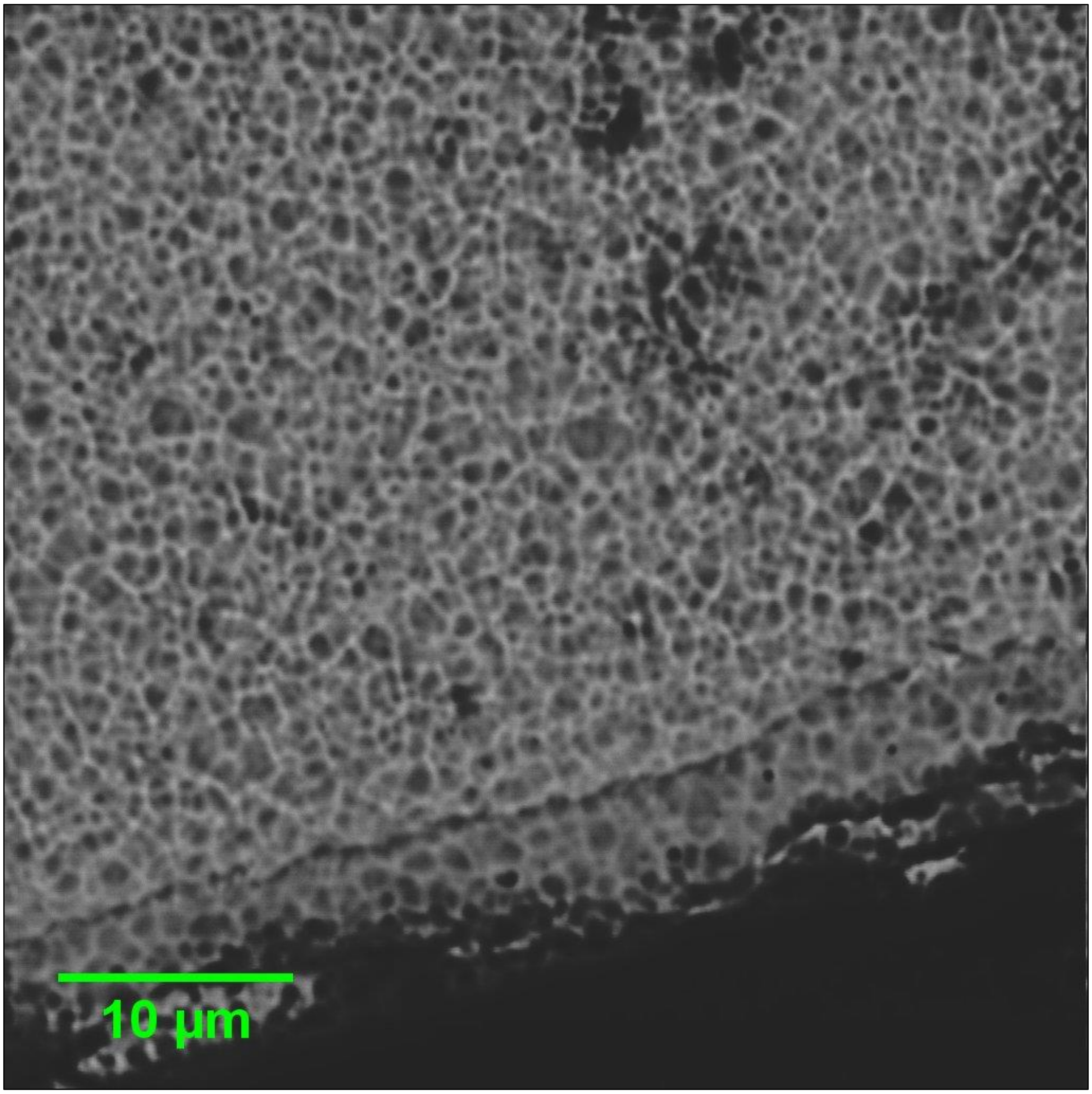

Fig. 4.3 LAE-2:Etched micrograph, first indication of hydride formation, 8 A-hrs.

In order to increase the bulk hydrogen concentration the charging time was increased from less than $24\ hr$ to greater than $96\ hr$. All subsequent runs were employed the platinum mesh anode, used previously, so as to avoid potential complications from the rapid oxidation of the lead strip anodes. The alumina sample holder tube was also removed for this test. Post charging analysis of the first such sample, EAN-9, revealed a 17 μm hydride rim; approximately 330 $wppm$ of bulk hydrogen concentration, Figure 4.4.

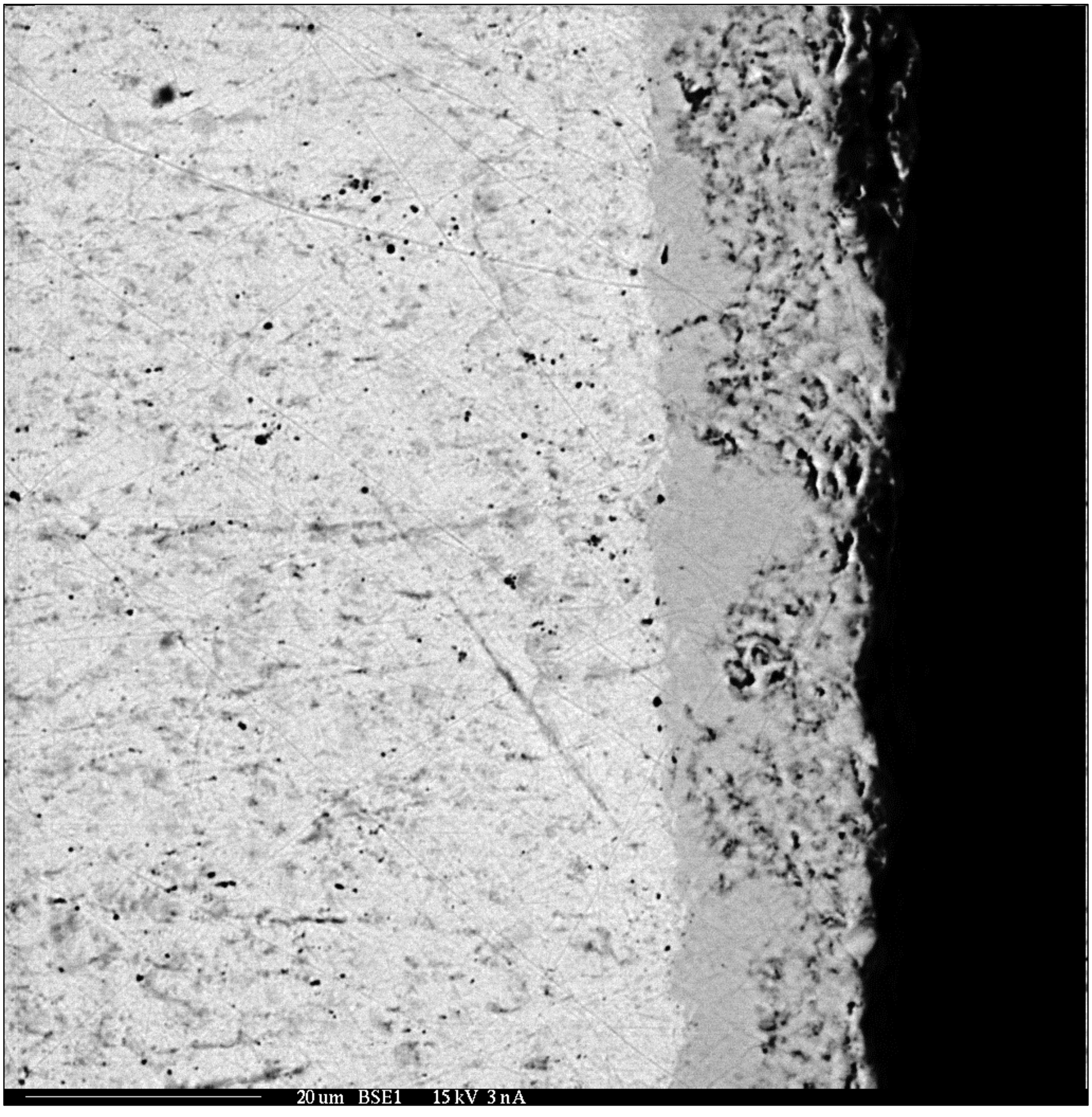

Fig. 4.4 EAN-9: Un-etched micrograph, 17 µm hydride rim, 326 A – hrs.

After the successful charging of EAN-9, two further samples, ZrH-1 and ZrH-2, were created to demonstrate repeatability and to set the charging parameters to be used for Zircaloy-4 and HANA-4. The first specimen, ZrH-1, showed good agreement with EAN-9; however, the hydride layer was split between the inner and outer surfaces. The second, ZrH-2, showed no indication of hydride formation. It is thought that connection between the zirconium wire and the sample was inadequate, which may be the primary reason for previous failures. A second possibility lies in the Alumina sample holder, which was reintroduced in ZrH-2, to prevent the sample on the cathode with from making contact with the anode.

4.2 Parametric Study

After achieving successful hydrogen insertion in EAN-9 and ZrH-1, the focus of the study shifted from proving the charging method to a parametric study of hydrogen charged Zircaloy-4 and HANA-4. Table 4.2 reproduces the list of charging conditions, resulting hydride thicknesses, and estimated bulk hydrogen concentrations for these samples. The hydrogen concentration estimates are based on $Eq. (2.3)$, taken from [40].

Table 4.2

Charging Parameters and Results

Experiment	Electrolyte		Current Density	Run Time	Hydride	H
Sample	Temp.	Concentration	$\frac{A}{cm^2}$	$A \cdot h$	μm	$wppm$
HZrH-1	65-71 °C	0.2 M	0.39**	342.0	33.8 ± 1.8	840
HZrH-2	65-69 °C	0.2 M	0.39**	680.0	51.2 ± 1.0	1260
Zr4H-1	63-68 °C	0.2 M	0.27	344.7	19.3 ± 1.2	160-220*
Zr4H-2	63-68 °C	0.2 M	0.27	>584.4	12.3 ± 0.3	110***
Zr4H-3	63-69 °C	0.2 M	0.37	680.3	14.9 ± 1.2	130-170*

* The larger value includes hydride contribution from all four faces.

** The target current density was 0.2 $\frac{A}{cm^2}$. The effective current density was twice the target current density; because, the inner surface was inactive during charging.

*** Charging was interrupted by a power failure.

To carry out this study, two HANA-4 samples, HZrH-1 and HZrH-2 and two Zircaloy-4 samples, Zr4H-1 and Zr4H-2 were created. However, during the charging of Zr4H-2, power was lost for indeterminate amount of time and the number of amp-hours charged was unknown. A third Zircaloy-4 sample, Zr4H-3 was run to replace Zr4H-2.

As the thickest hydride rim, and higher potential bulk hydrogen concentration was achieved in sample HZrH-2, it was decided that characterization and analysis would focus on HZrH-2 and Zr4H-3. Zr4H-3 was charged with the same current density and for an equivalent number of amp-hours as HZrH-2. Thus, the target current density for Zr4H-3 was increased to 0.4 $\frac{A}{cm^2}$.

Examples of as received and charged HANA-4 and Zircaloy-4 are shown in Figure 4.5 and Figure 4.6.

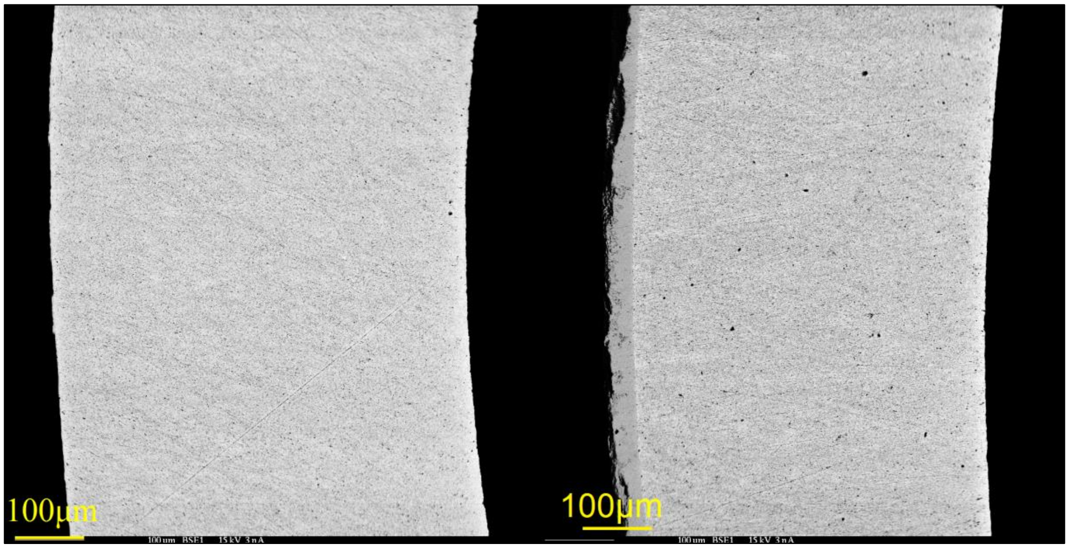

Fig. 4.5 Pre and post charging HANA-4 (BSE). (Left) As received HANA-4. (Right) Hydrogen charged HANA-4.

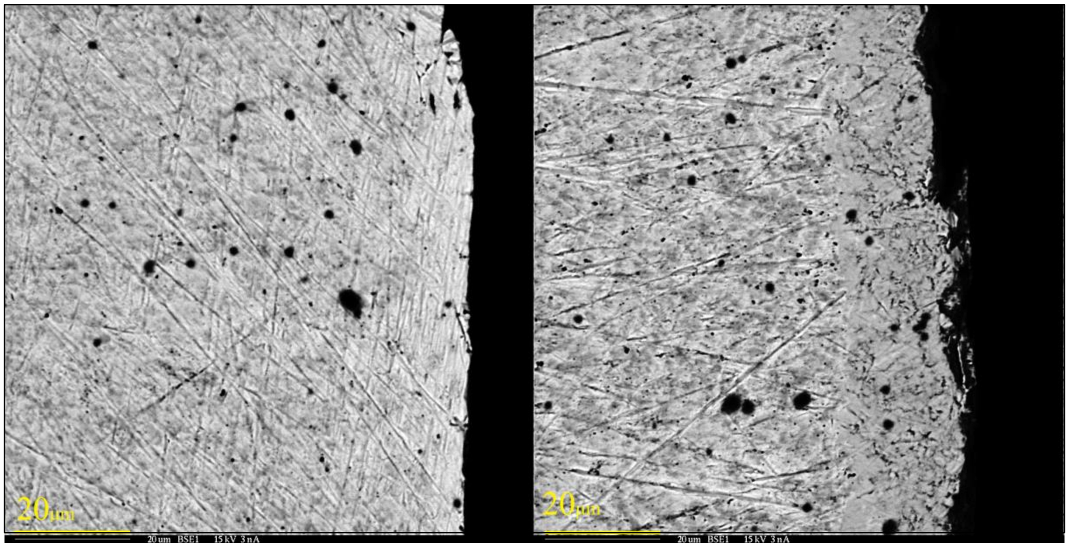

Fig. 4.6 Pre and post charging Zircaloy-4 (BSE). (Left) As received Zircaloy-4. (Right) Hydrogen charged Zircaloy-4.

4.2.1 Parametric Studies in HANA-4

Charging HZrH-2 for 680 *A-h*, with a current density of $0.39\,\frac{A}{cm^2}$, resulted in a 51 ± 1μm hydride rim. A back scattered electron (BSE) image of the charged specimen is shown in Figure 4.7. This specimen was not chemically etched prior to imaging.

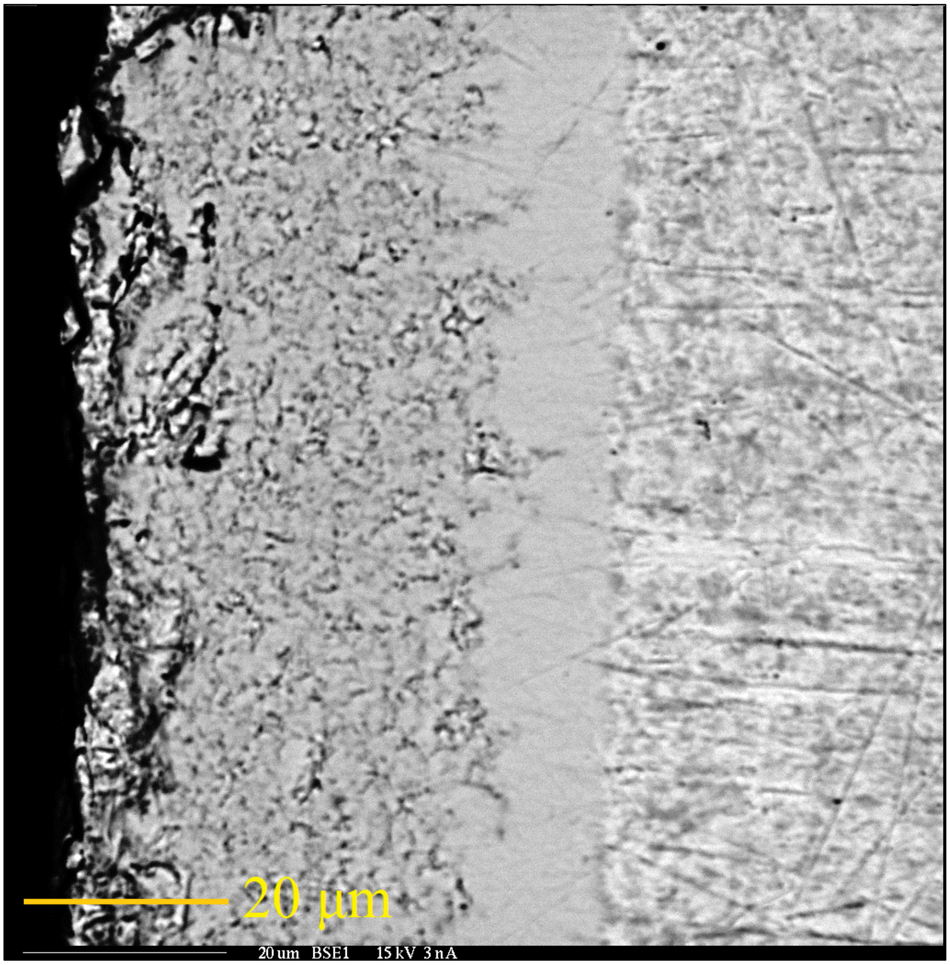

Fig. 4.7 HZrH-2: 51µm thick hydrided region, 680 A-h, 0.39 A/cm^2.

The image shows three distinct phase regions in the sample. The inner region, at right, is the bulk zirconium alloy. The darker region, to the left, is a dual zoned hydride rim. The hydrided region exhibits two topologies: rough and porous at far left, and smooth toward the middle of the image. The rough area is may be the region of greatest hydrogen concentration, as hydrogen ingress occurs from the outer surface and hydrogen diffusion is slow at the charging temperature 65 °C. The roughness is likely due to material loss from the brittle hydride phase during the grinding step in metallographic preparation.

A portion of the charged sample, HZrH-2, was annealed for 1 hour at 540 °C. The annealing process comprised ramping from ambient to 540 at 25 °C/min, followed by a 60 minute hold, and furnace cooling back to room temperature. This homogenization was only partially successful, as seen in Figure 4.8. Annealed specimens were chemically etched to provide greater contrast between the bulk and the hydrides. Etching used the solution and technique described in §3.4.

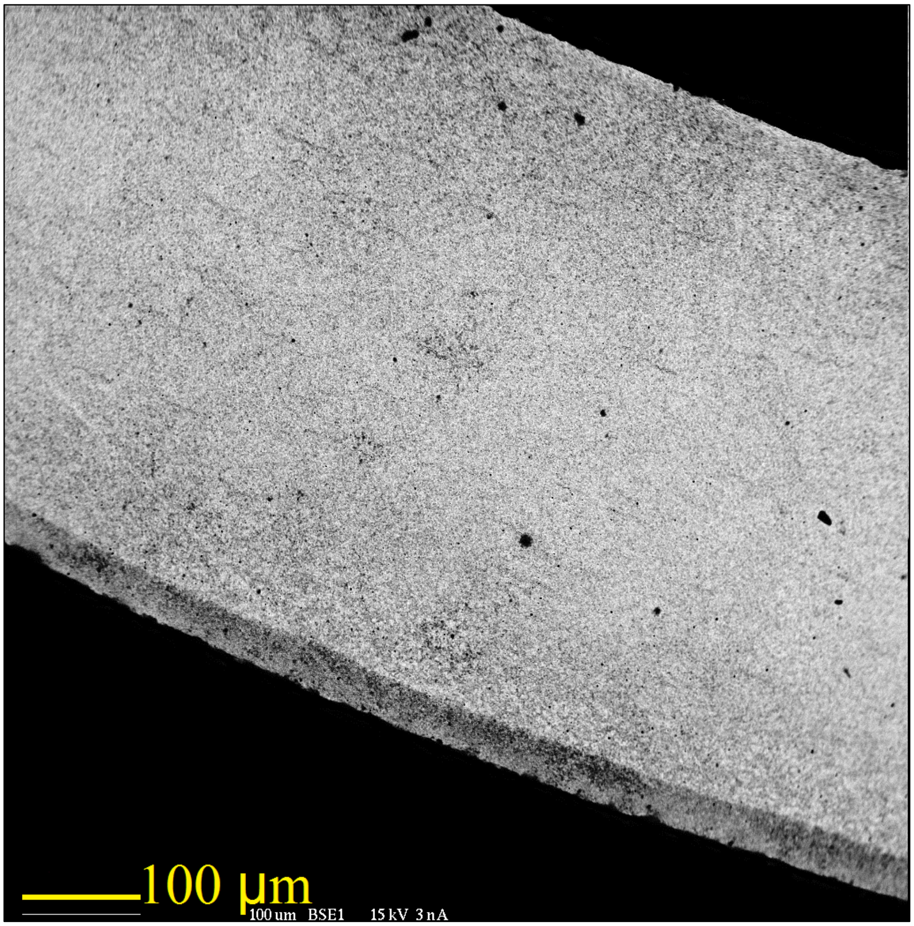

Fig. 4.8 HZrH-2: Post annealing 60 min at 540 °C.

From the figure, it is apparent that the majority of hydrogen remained in the hydride rim. A small number of faint hydride platelets are visible in the bulk; however, analysis of the image revealed that the hydride thickness at the rim was unchanged. This was not expected. The hold time, 60 minutes, was chosen to be a factor of four greater than the 15 minutes that should have been sufficient to reach 97% of the equilibrium concentration throughout the sample, as done by Khatamian [23]. The 15 minute diffusion time was calculated using *Eq.* (3.1) and the average diffusion coefficient for zirconium, Zircaloy-2, and Zircaloy-4 reported coefficient reported by Kearns [51], *Eq* (3.2).

A possible explanation for this unexpected outcome could be that there was more hydrogen in the rim than could diffuse to the bulk under the applied annealing conditions. The bulk hydrogen content, obtainable from the rim, was estimated to be between 1260 and 1600 wppm. Estimates were made using *Eq.* (2.3) and *Eq.* (2.6) respectively. Using TSS_d data for the average of zirconium, Zircaloy-2, and Zircaloy-4 from Kearns [14] Eq(2.1), TSS_d at 540 °C is 600 wppm , which means that it would be expected for the Zr solution to saturate at 600 wppm if HANA 4 were to behave in a similar manner to Zricaloy 4. However, the relatively small number of hydride platelets visible in Figure 4.4, suggests a bulk concentration well below the possible 600 wppm (see Figure 2.10 for comparison).

A second piece of HZrH-2 was annealed, because of the incomplete hydride redistribution seen in the previous sample, the annealing conditions were changed to 4 hrs at 550°C, Figure 4.9.

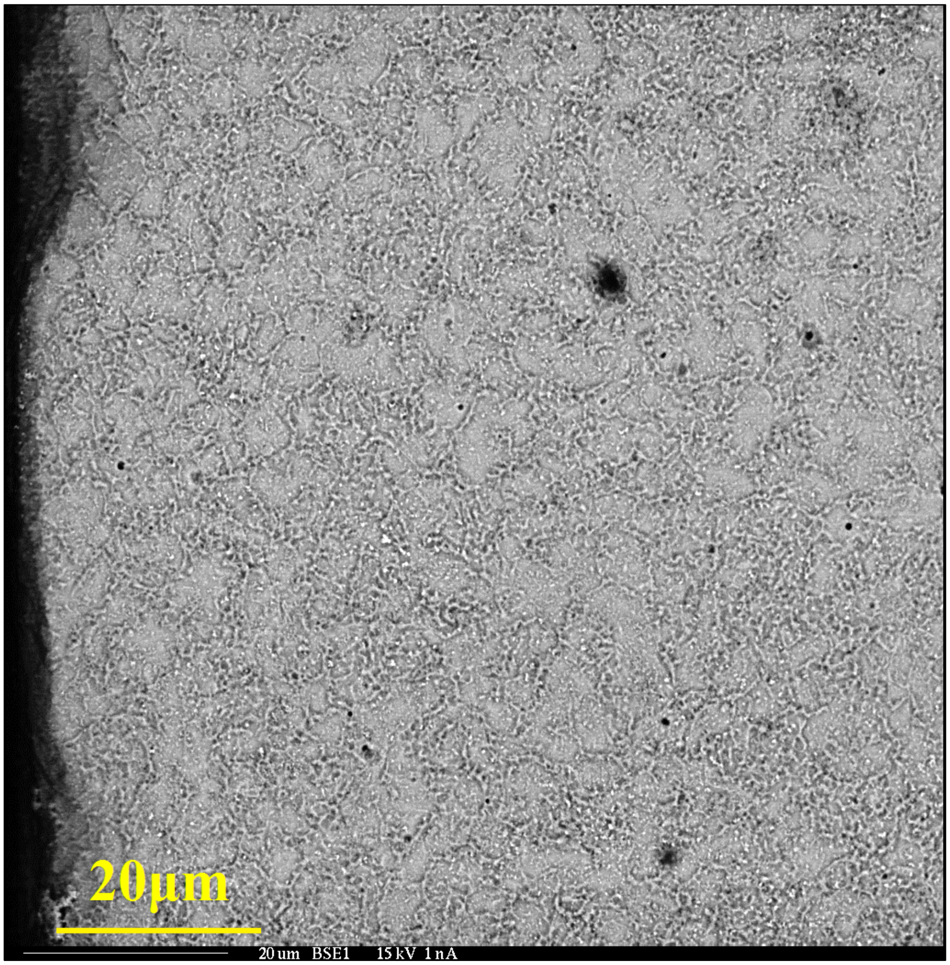

Fig. 4.9 Post annealing rim removal, prior to H measurement. Annealed 550 °C for 4 hrs.

The sample shown in Figure 4.9 was cut from the material sent to IMR Test labs for hydrogen content measurement. This sample was ground with silicon carbide papers, post annealing, to remove any remaining rim prior to hydrogen concentration measurements by IMR. From the figure it is clear that grinding has completely removed any hydride rim that might have remained after the extended anneal.

4.2.2 Parametric Studies in Zircaloy-4

The Zircaloy-4 sample, Zr4H-3, charged with the same current density, for an equivalent number of A-hrs as HZrH-2, see Table 4.2 for details, developed a thinner hydride rim,15±1 μm, as seen in Figure 4.10.

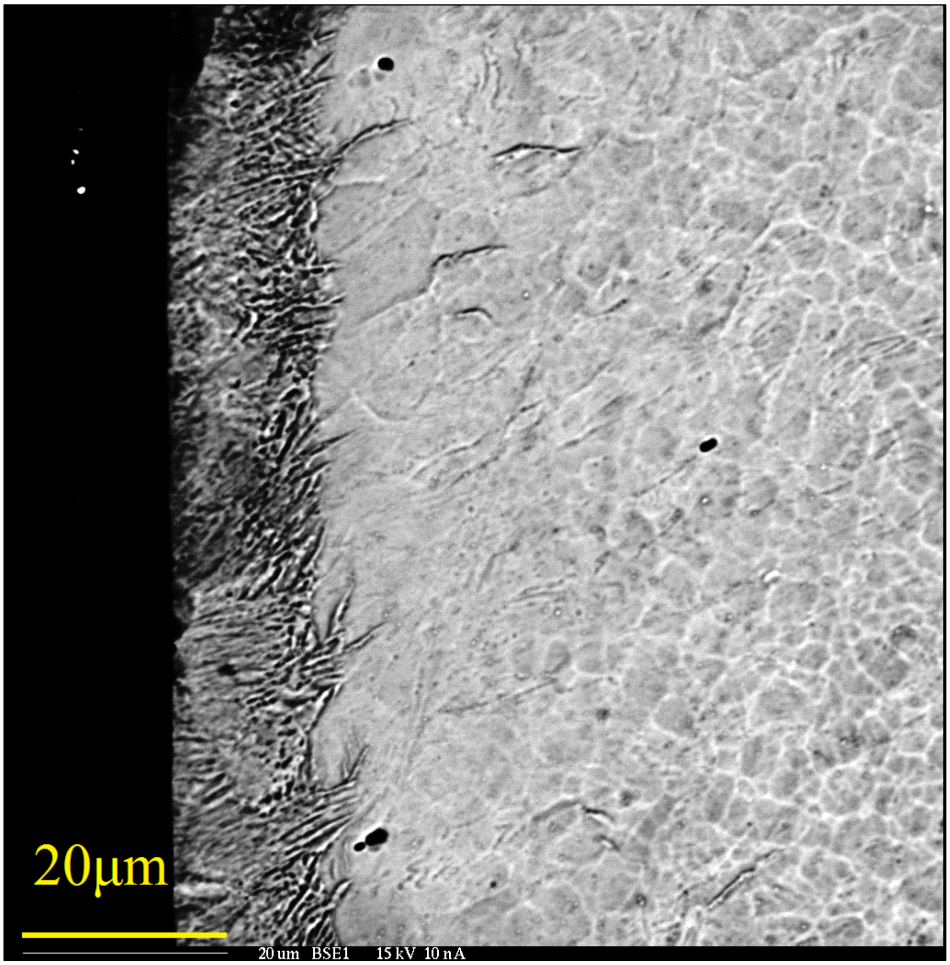

Fig. 4.10 Zr4H-3: 15μm thick hydrided region, 680 A-h, 0.39 A/cm^2.

As with the HANA-4, a diffusion time was calculated, using *Eq*. (3.1) and the Kearns [51] data. The estimated diffusion time was multiplied by four, yielding a furnace dwell time of 270 mins. Similarly, a ramp rate of 25 °C/min was used, and the sample was furnace cooled to room temperature. However, unlike the HZrH-2 sample, the homogenization successfully produced a uniform distribution of readily visible hydride platelets leaving no visible hydride rim behind, Figure 4.11.

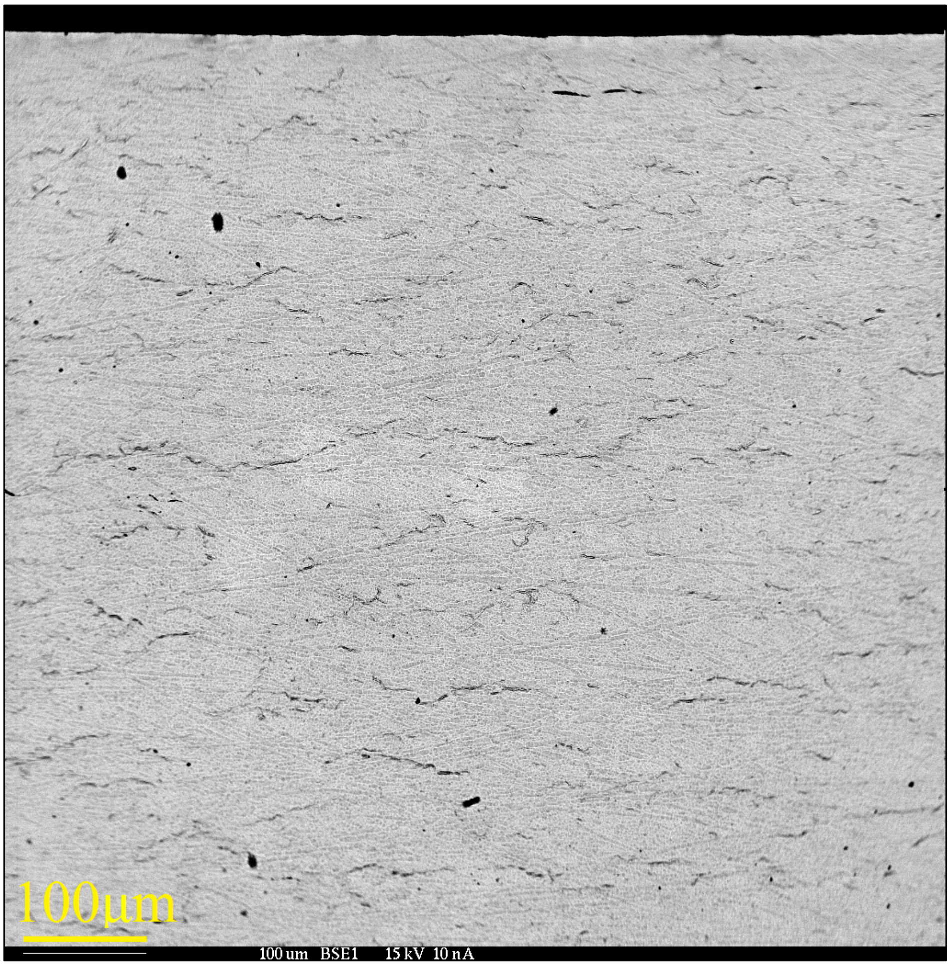

Fig. 4.11 Zr4H-3: Post annealing, 270 min at 540 °C.

In contrast to the HZrH-2 sample, where the estimated bulk concentration from the rim exceeded the solvus concentration from Kearns TSS_d data, Zr4H-3 had an estimated hydrogen concentration of 170-200 wppm, by Equations (2.3) and (2.6). A concentration of even 200 wppm is well below the solvus concentration of 600 wppm at 540 °C. Hence, the homogenization parameters were sufficient to dissolve the hydride rim, and redistribute the hydrides in a uniform manner.

4.3 X-Ray Diffraction

Charged samples were further characterized through X-ray diffraction. Table 4.3 lists the peaks for phases of interest; within the range of measurement. File numbers 05-0665 (α-Zr), 34-657 (β-Zr), 34-0690 (γ-ZrH), 34-0649 (δ-$ZrH_{1.66}$), and 17-314 (ε-ZrH_2) from the Joint Committee on Powder Diffraction Standards (JCPDS) were used to index the diffractograms. The zirconium-oxide peaks listed in Table 4.1 were taken from the Standard X-ray Diffraction Powder Patterns, published by the National Bureau of Standards [81].

Table 4.3

XRD Peaks for Zirconium, Zirconium Hydride, and Zirconium Oxide

Zirconium and Zirconium Hydrides Peaks: Range 48-72 in 2θ								
Zr	Intensity	δ-ZrH$_{1.66}$	Intensity	γ-ZrH	Intensity	ε-ZrH$_2$	Intensity	ZrO
α-48.0	17	54.2	37	54.3	24	51.9	12	56.1
β-51.5	17	64.6	43	56.6	11	55.3	18	67.1
α-56.9	17	67.8	12	62.9	16	62.5	20	70.6
α-63.5	18			67.0	14	67.8	8	
β-64.3	33			69.0	13	68.6	8	
α-66.8	3							
α-68.5	18							
α-69.6	12							

X-ray diffractograms for post annealing HZrH-2 and Zr4H-3 are given in Figures 4.12 and 4.13, respectively.

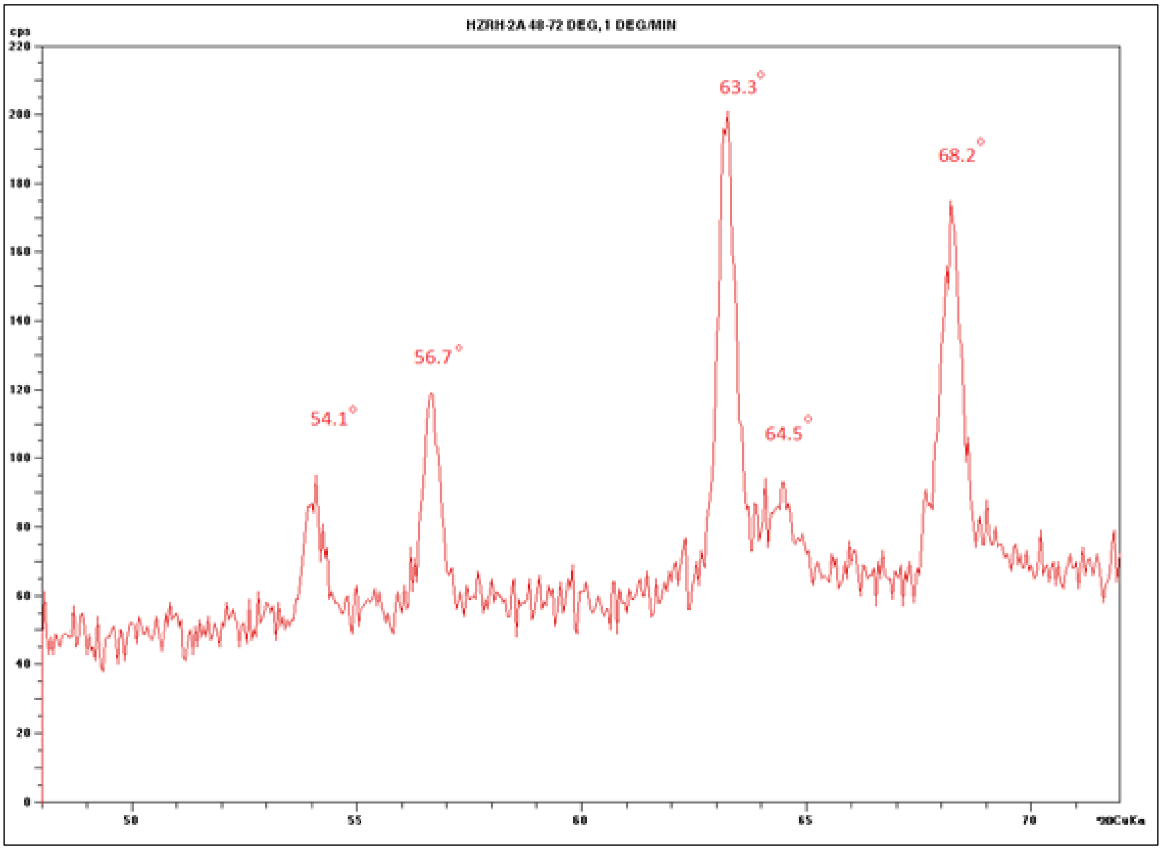

Fig. 4.12 Post annealing HANA-4: 48° – 72° in 2θ. Sample, HZrH-2

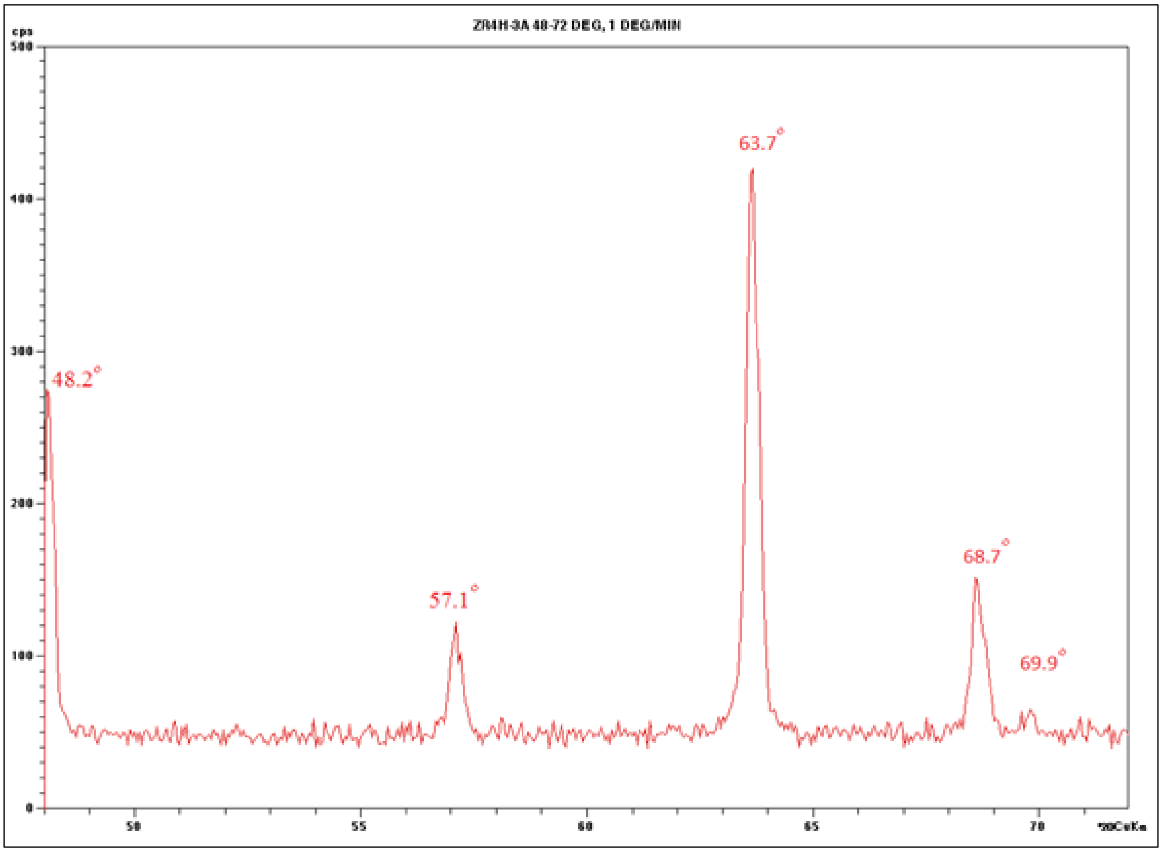

Fig. **4.13** Post annealing Zircaloy-4: 48° – 72° in 2θ. Sample Zr4H-3A.

Additional X-ray diffraction plots of HZrH-2 and Zr4H-3, pre and post charging, are provided in Appendix A. The phases identified and the peaks measured, pre and post charging, for each sample are given in Table 4.4.

Table 4.4

Phases Identified as Received and Post Charging: Angle in 2θ

α-Zr		ε-ZrH2		δ or δ+α	
HZrH-0*	Zr4H-0*	HZrH-1	HZrH-2	Zr4H-1	Zr4H-3
	48.0	52.1	52.2	54.2	54.1
56.7	56.9	54.9	55.0	64.3	64.2
63.2	63.5	62.7	62.8	67.8	68.0
68.2	68.5	67.6	67.2	68.7	

*Numerical designation zero indicates as received alloy.

Uncharged HANA-4 and Zircaloy-4 both exhibited pure α-Zr peaks in their diffraction patterns. Although HANA-4 is reported to contain β-Zr, no β peaks were observed. This is likely due to the volume fraction of the β-Zr being below the detection limit. For charged and annealed samples the presence of β-Zr is potentially masked by hydride peaks, see Table 4.1. Charged HANA-4 had sufficient hydrogen concentration in the rim that XRD revealed pure ε-hydride peaks, corresponding to a hydrogen wt% > 1.8, see Figure 2.1 for Zr-H phase diagram. By comparison, the δ or δ+α phase was identified for the Zircaloy-4 specimens, which corresponds to a large region of the phase diagram, 0 wt%< C_H < ~1.7 wt%; where C_H is hydrogen concentration.

The observed hydride phases in both HANA-4 and Zircaloy-4 were transformed after annealing. Due to the closely spaced peaks of the Zr-H system, it was difficult to determine exactly which phases were present. It appears that some of the metastable γ-phase may have formed in the HANA-4 samples during cooling. The post annealing Zircaloy-4 appears to be pure zirconium, despite metallographic evidence to the contrary. Post annealing peaks and corresponding phases are given in Table 4.5.

Table 4.5

Phases Identified Post Annealing: Angle in 2θ

γ+δ or α+δ		α	
HZrH-1A	HZrH-2A	Zr4H-1A	Zr4H-3A
54.0	54.1	48.2	48.2
56.7	56.7	57.1	57.1
63.2	63.3	63.7	63.7
64.5	64.5	68.7	68.7
68.2	68.2	69.9	69.9

4.4 Hydrogen Concentration Measurements

4.4.1 External Laboratory Measurements

Charged sections from annealed portions of HZrH-2 and Zr4H-3 were sent to IMR Test Labs, 131 Woodsedge Dr. Lansing, NY. 14882, for hydrogen content measurement. The full reports are given in Appendix B. The HANA-4 required the remaining hydride rim to be removed, as the goal was to measure the bulk concentration after annealing at 550 °C for 4 hrs (Figure 4.9). This was not necessary for the Zircaloy-4, as BSE imaging showed no remaining rim under identical annealing conditions (540 °C 270 min) Figure 4.11. Measurement of hydrogen concentration was performed via inert gas fusion-thermal conductivity. The measurement required a minimum of 2 grams of material. The results of the hydrogen concentration measurements by IMR are given in Table 4.6.

Table 4.6

Measured Hydrogen Content

Sample	Hydrogen wt%	Hydrogen wppm	Est. H wppm *Eq*(2.6)
HZrH-2	0.16	1600	1600
Zr4H-3	0.017	170	200

Measurements of alloy composition performed by IMR Test Labs, 131 Woodsedge Dr. Lansing, NY. 14882.

These measurements are in good agreement with the hydrogen concentration estimates based on observed hydride thickness and the density of the observed hydride phase, yet unexpectedly high for the annealed HANA-4 sample HZrH-2. As noted in the discussion of Figure 4.9, the Kearn's line [14] *Eq* (2.1), gives the TSS_d of Zircaloy-4 at 540 °C as 600 wppm hydrogen. The presence of 1600 wppm hydrogen in the annealed portion of HZrH-2 suggests that HANA-4 may have a significantly higher TSS than Zircaloy-4.

4.5 Annealing and Differential Scanning Calorimetry

4.5.1 Measurements with Netzsch 409 STA

As discussed in §3.5.5 , the Netzsch 409 was used to load hydrogen from the charged rim into the bulk of the sample as preparation for hydride dissolution temperature (HDT) measurement. It was also used for the first series of HDT measurements in both alloys. Measurements with the Netzsch 409 proved to be inconclusive, as the DSC signal was dominated by the baseline behavior of the system, see Figure 4.14.

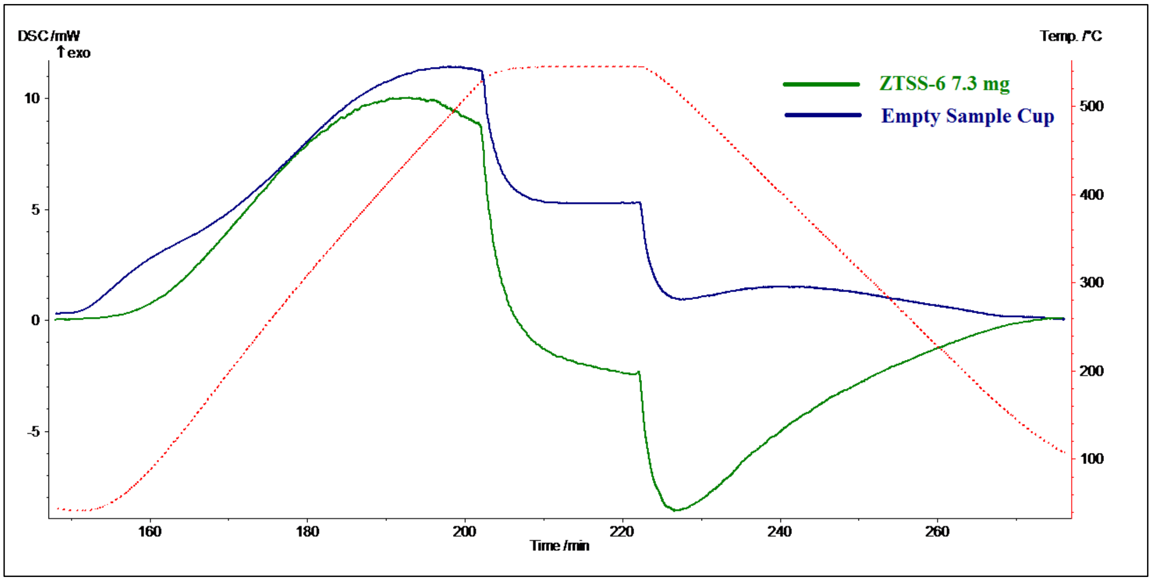

Fig. 4.14 Typical heat flow response over 1 cycle, Netzsch STA 409. With sample and empty.

As seen in Figure 4.14, the sample curve, green, and empty system curve, blue, follow a similar pattern. All significant changes in the signals are related to changes in the temperature profile, red. This behavior was typical of results obtained with the Netzsch. None of the HDT measurements attempted with the Netzsch instrument were successful, as no dissolution or precipitation peaks could be definitively identified in the DSC signal. The heating curves for each alloy are shown in Figures 4.15 and 4.16.

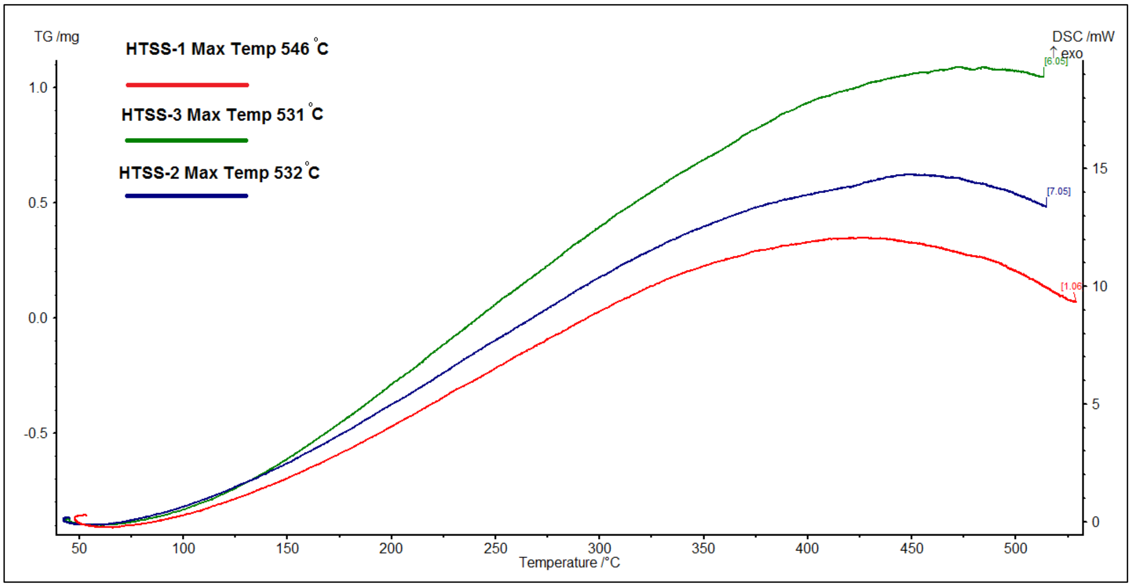

Fig. 4.15 Heating curves, HTSS-1, HTSS-2 and HTSS-3: heating/cooling 10 °C/min.

In both alloys the heating curves appear smooth; giving no indication of a hydride dissolution peak. The heating curves for Zircaloy-4 are given in Figure 4.16.

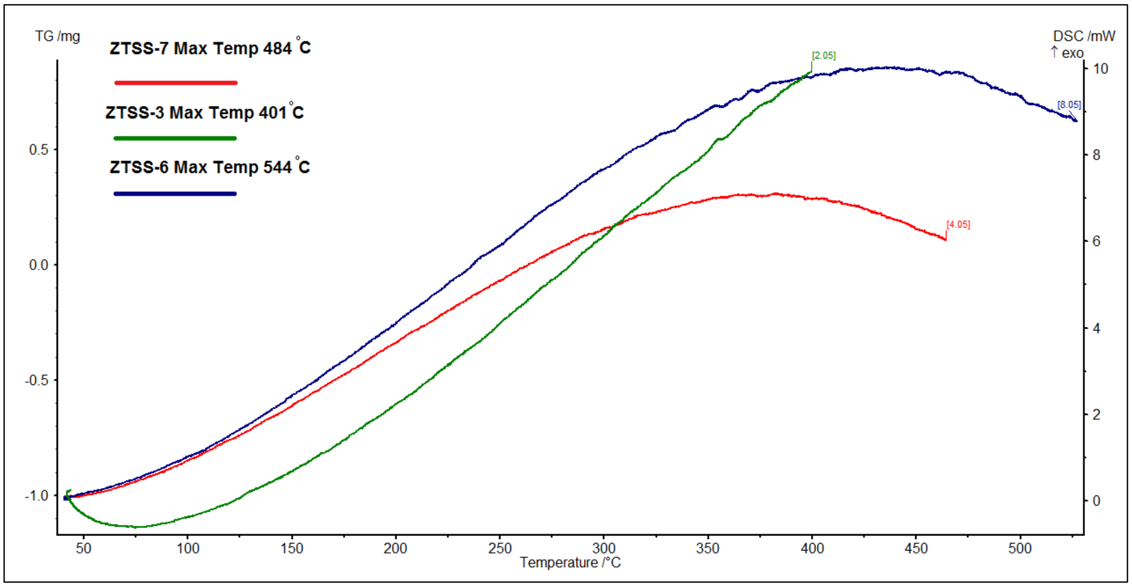

Fig. 4.16 Heating curves, ZTSS-1, ZTSS-2 and ZTSS-3: heating/cooling 10 °C/min.

Samples HTSS-2 and HTSS-3, exhibited small exothermic peaks during cool down from max temperature, of the HDT measurement, Figure 4.17. Likewise, sample ZTSS-3 contained a similar exothermic peak during the homogenizing anneal, but no peaks were seen during the cooling portion of the HDT measurements for this sample, see Figure 4.18.

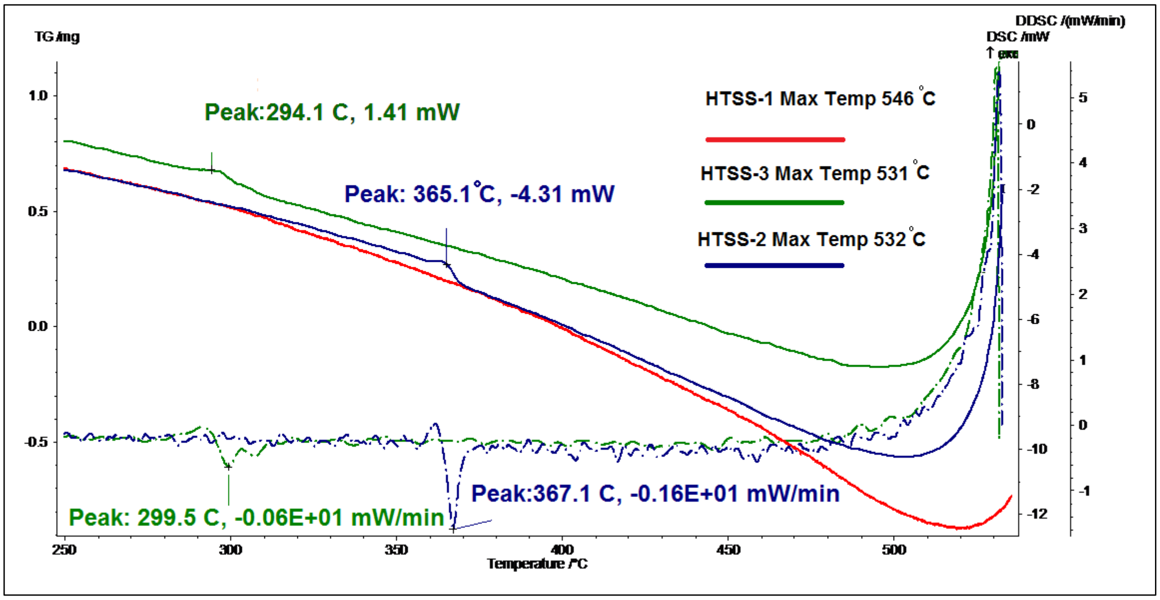

Fig. 4.17 Cooling curves, HTSS-1, HTSS-2 and HTSS-3: heating/cooling 10 °C/min..

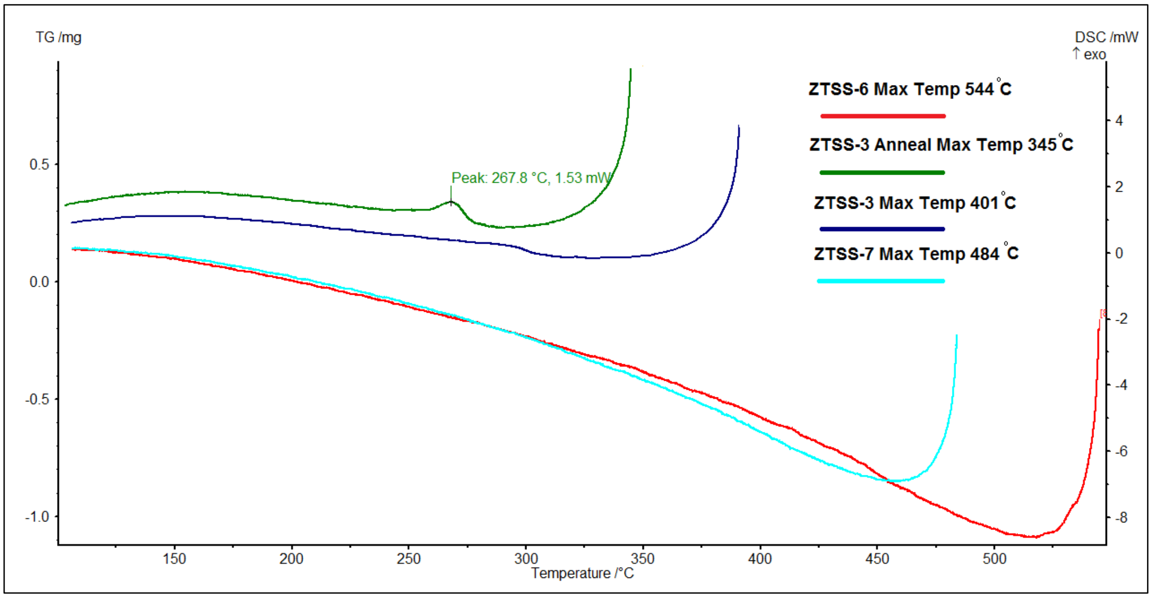

Fig. 4.18 Cooling curves, 10 °C/min: Zircaloy-4.

These small peaks are unlikely to be hydride precipitation peaks; especially in light of the HDT measurements made with the TA Q600. Other reasons suggesting they are not dissolution peaks include the following: they are not present in all samples, nor are they present in all the runs of a single sample. As noted above, ZTSS-3 exhibited a cooling peak during the annealing, but did not in either of the two HDT measurement runs. Additionally, these peaks are very small and blunted compared to precipitation peaks reported in literature [8, 18, 20].

The peak temperatures (PT) and maximum slope temperatures (MST), for these peaks are listed in Table 4.7.

Table 4.7

Netzsch: Peaks Observed During Cooling

Sample	PT °C	MST °C
HTSS-2	365.1	367.1
HTSS-3	294.1	299.5
ZTSS-3	267.8	273.6

4.5.2 Measurements with TA SDT Q600 DSC/TGA

The results from the TA Q600 DSC/TGA measurements are markedly different from those performed on the Netzsch STA 409, in that some changes in the DSC signal are independent of the temperature profile, Figure 4.19. The results of these measurements are presented below; for HANA-4 and Zircaloy-4. For completeness, an attempt was made to analyze the peak temperature (PT), onset temperature (Onset), and maximum slope temperature (MST) for all significant features in the DSC signal. However, the hydride dissolution temperature is the primary feature of interest, with secondary consideration being given to the hydride precipitation temperature, in this study.

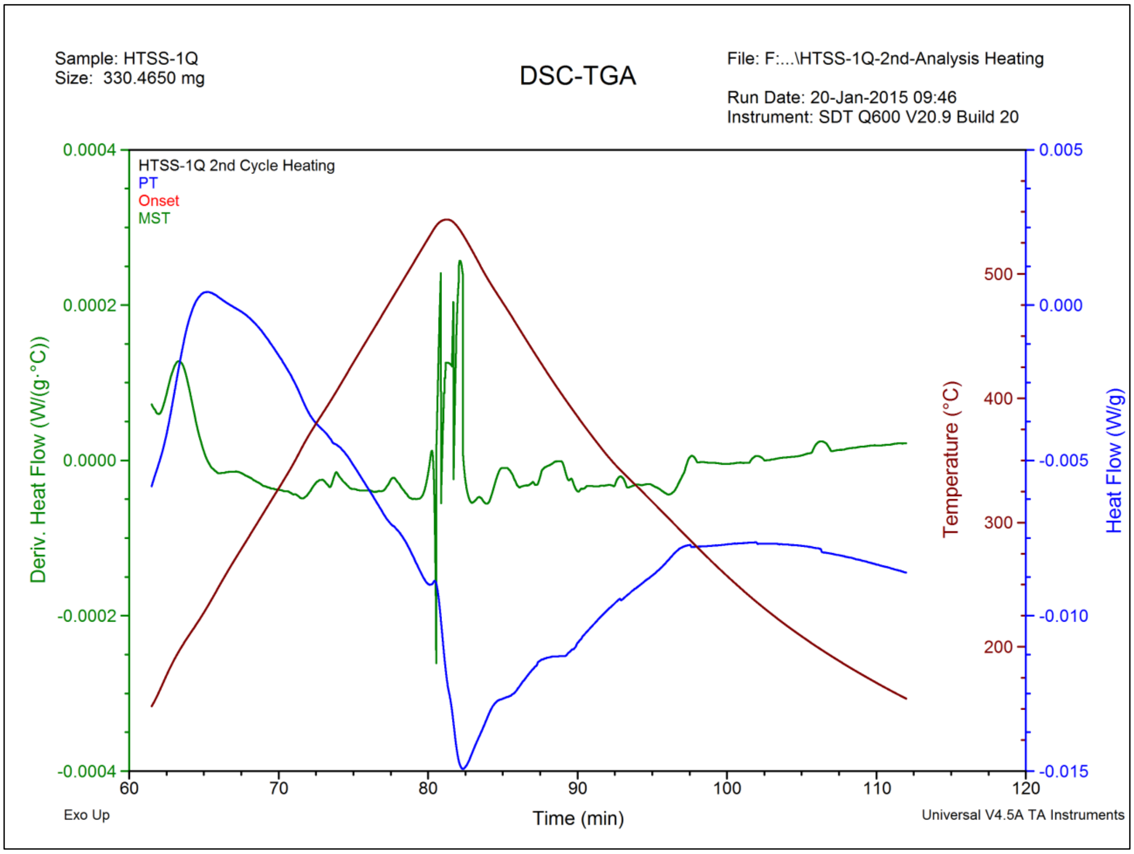

Fig. 4.19 Example of DSC signal over 1 cycle: TA Q600.

Hydride dissolution is an endothermic event, and occurs upon heating above the dissolution temperature, TSS_d. Hydride precipitation is an exothermic event, and occurs upon cooling at a temperature below the dissolution temperature. These are the criterion by which potential hydride dissolution and precipitation peaks were judged.

Characteristics of peaks, observed during heating, that are close to the annealing temperature are given in Table 4.8 below.

Table 4.8

Hydride Dissolution Temperature Measurements Q600. DSC (°C)

HTSS-1	Cycle-2	Cycle-3	Anneal	ZTSS-6	Cycle-2	Cycle-3	Anneal
PT	528.60	528.31	533	PT	391.90	394.16	530
Onset	527.22	526.97		Onset	389.47	390.39	
MST	534.26	533.81		MST	405.19	404.91	
HTSS-2	Cycle-2	Cycle-3	Anneal	ZTSS-7	Cycle-2	Cycle-3	Anneal
PT	429.57	429.48	422	PT	455.51	456.26	438
Onset	430.23	422.91		Onset	432.59	452.29	
MST	438.44	422.39		MST	443.43	466.88	
HTSS-3	Cycle-2	Cycle-3	Anneal	ZTSS-3	Cycle-2	Cycle-3	Anneal
PT	371.06	373.01	346	PT	354.56	351.49	345
Onset	352.08	355.73		Onset	355.68	352.25	
MST	363.71	364.94		MST	363.52	362.75	

Hydrogen free specimens of HANA-4 and Zircaloy-4 were measured under the same conditions, max temp 480 °C, 20 °C/min heating and cooling, for 3 cycles with 1 minute holds between dynamic segments, as HTSS-2Q and ZTSS-7Q. Analyzed heating curves for hydrogen charged and hydrogen free samples of each alloy are presented in Figures 4.20 – 4.23.

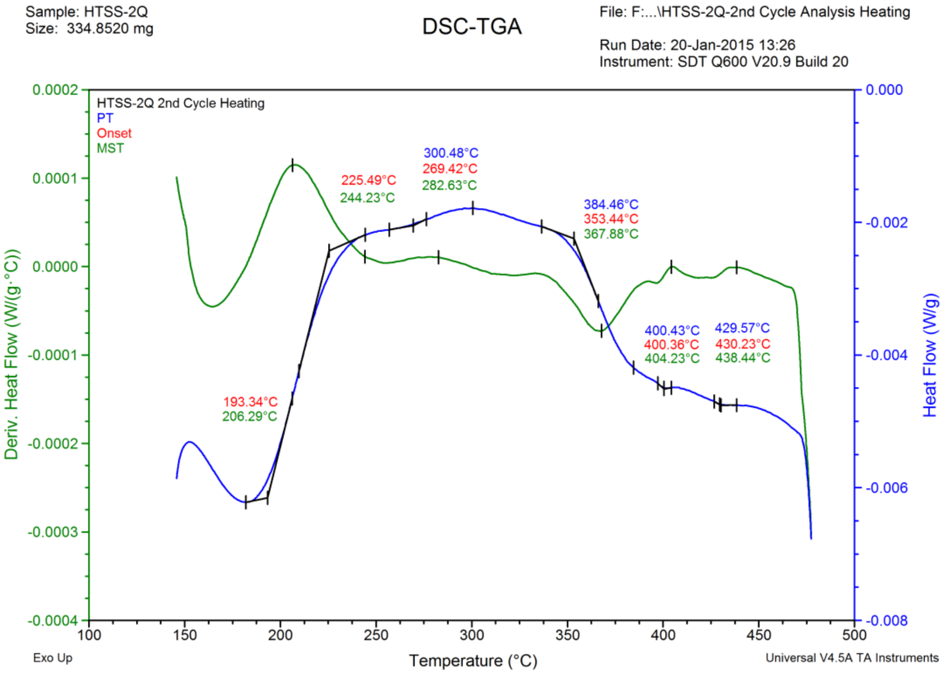

Fig. 4.20 HTSS-2Q: Heating curve, Max Temperature 480°C.

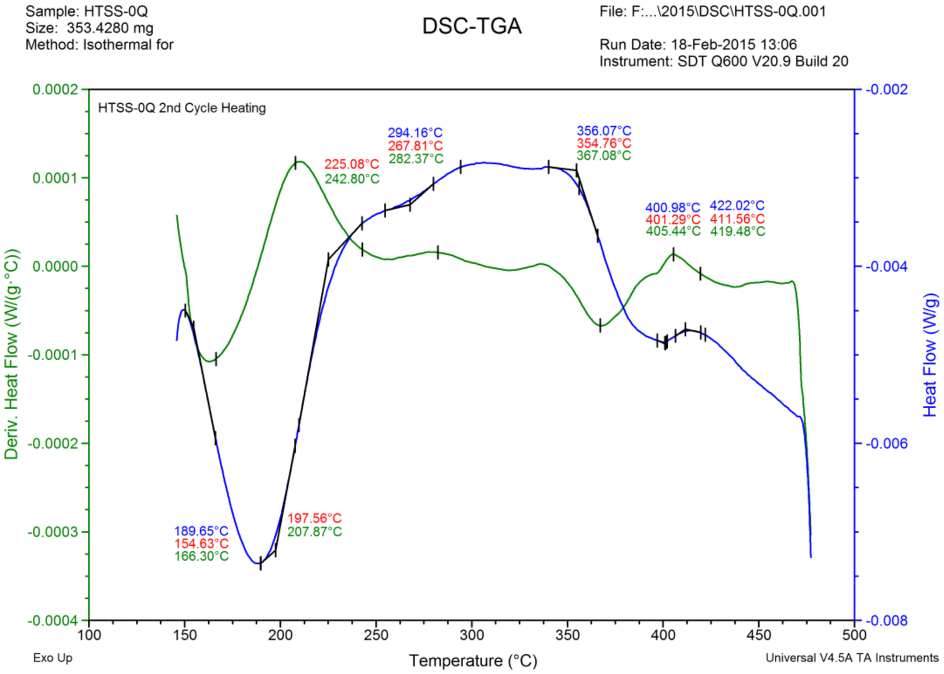

Fig. 4.21 HTSS-0Q: As received material: Heating curve, Max Temperature 480 °C.

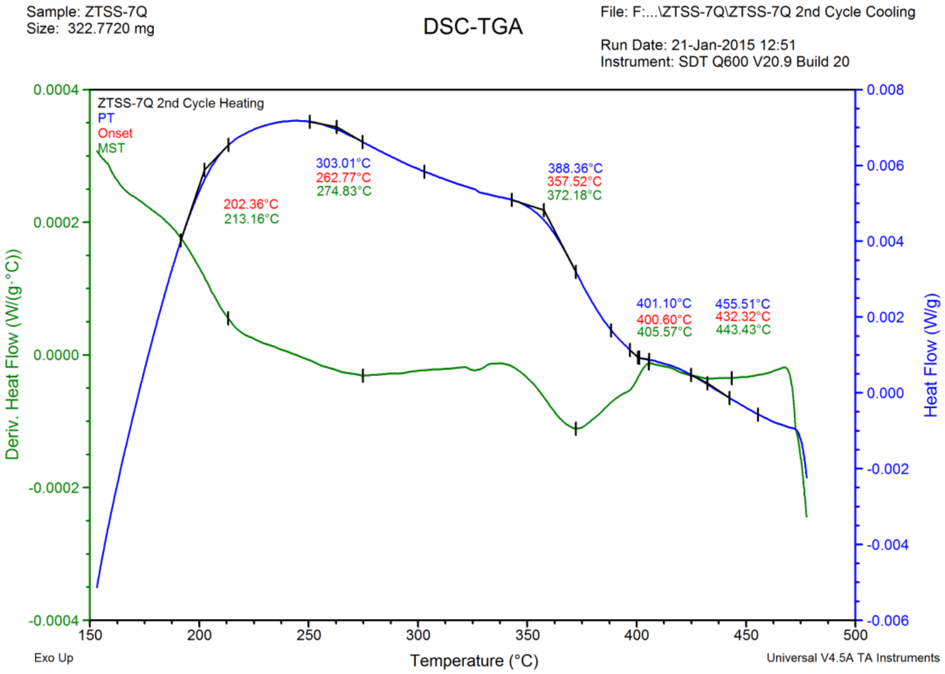

Fig. 4.22 ZTSS-7Q: Heating curve, Max Temperature 480 °C.

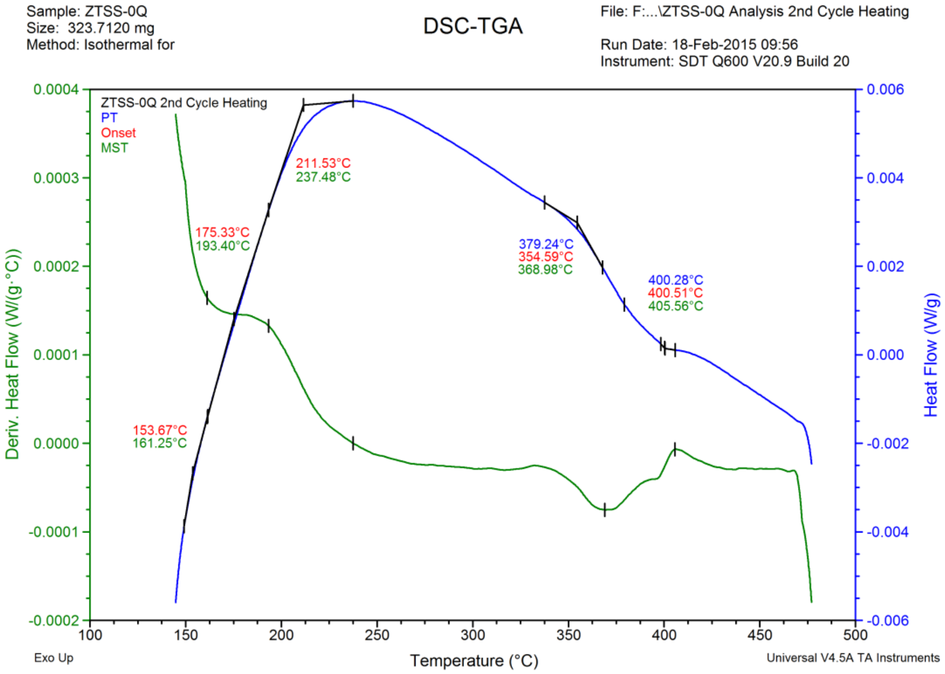

Fig. 4.23 ZTSS-0Q As received Material: Heating curve, Max Temperature 480 °C.

The above figures show that the general shape of the DSC curve is the same for hydrogen charged and hydrogen free specimens of the same alloy. The hydrogen charged specimens contain additional features, endothermic dips in the DSC signal potentially indicating a hydrogen related reaction. Though the DSC signal for the two alloys differ in appearance, in both the charged and uncharged specimens there is an endothermic event that begins at an onset temperature around 350 °C and finishes near 400 °C. This event is present in all samples, charged or uncharged, though it is truncated in the samples that only reached 380 °C.

CHAPTER V

DISCUSSION

Though the early attempts at cathodic charging were largely unsuccessful, they provided an opportunity to gain experience with the characterization methods employed in this study. Analysis of the inconclusive results led to modifications in the cathodic charging system and procedure; ultimately resulting in a system capable of consistently charging zirconium alloys with hydrogen concentrations above 1000 wppm.

5.1 Comparison and Analysis of Parametric Studies

A notable difference was observed in the post charging hydride rim thicknesses in the two alloys. In HANA-4 the observed rims were 30 – 50 μm thick, while in Zircaloy-4 the observed rims were only 10 – 20 μm thick. Samples HZrH-2 and Zr4H-3 were charged for an equivalent number of amp-hours, with the same target current density. Despite this, HZrH-2 had a 50 μm rim compared to the 12 μm rim of Zr4H-3. Estimating the mass of hydrogen contained in each sample using *Eq*(2.4) and *Eq*(2.5) suggests that HZrH-2 contained up to four times the mass of hydrogen as Zr4H-3.

However, the difference in rim thickness between Zr4H-3 and HZrH-2 may not be due entirely to a difference in materials or geometry. Zr4H-3 ran for twice as many *A*-*h*, at twice the current density of Zr4H-1. This should have resulted in a thicker rim on

Zr4H-3 than Zr4H-1, as both the run time and increased current density should have resulted in increased hydrogen content. Yet, as seen in Table 4.2, the hydrided region on Zr4H-3 is approximately 4 μm thinner than the one on Zr4H-1. Thus, while geometry likely plays a significant role in the effectiveness of hydrogen charging, as suggested by Figure 3.3, it also appears that some variation in charging conditions is introduced from run to run. This is in part due to difficulty with the level switch. On occasion, the level switch would fail to turn off the pump, resulting in a dilution of electrolyte concentration.

The annealing results of the HANA-4 samples, taken from HZrH-2 proved interesting. The first attempt at annealing, 540 °C for 60 minutes, had no measureable effect on the thickness of the hydride rim. However, X-ray diffraction measurements on the annealed sample revealed that the hydride in the rim had transformed from the hydrogen rich ε-hydride phase (ZrH_2) to the δ-hydride ($ZrH_{1.66}$) phase. This explains why some hydride platelets were observed in the bulk, even though the rim thickness appeared unchanged. When a second section was annealed (Figure 4.9), 550 °C for 240 minutes, electron microscopy revealed a uniform network of fine hydrides distributed throughout the matrix. This section was from the material that was measured by IMR Test Labs. In order to measure the concentration of hydrogen in the bulk, the surface layer is was removed after annealing. The hydride rim was originally 50 μm thick, and a minimum of 250 μm was removed from the surface post annealing. This would be sufficient to remove the rim and prevent excess hydrogen from impacting the measured concentration. Hydride rim removal was confirmed via BSE/SE imaging of a section of the sample sent to IMR, Figure 4.9. IMR Test Labs reported a hydrogen concentration in this sample of 1600 wppm. The terminal solid solubility limit of hydrogen in Zircaloy-4, *Eq* (2.1), at 550 °C is approximately 640 wppm [14]. If the TSS_d of HANA-4 is consistent with that of Zircaloy-4, then the measured hydrogen concentration is expected to be 640 wppm after annealing, but was measured to be 1600 wppm. This interesting result indicates that HANA-4 has a significantly higher terminal solid solubility under dissolution (TSS_d) than Zircaloy-4.

It was noted earlier, §2.2, that β-Zr has been shown to have a higher TSS_d than α-Zr [33]. Park *et al* [82], reported that HANA-4 is heat treated to retain some of the meta-stable β phase, although the β phase was not detected in XRD measurements of the as received HANA-4. This is likely due to the volume fraction being too low for the β phase to be distinguished in the XRD measurements. If the β phase is present, as HANA-4 is a niobium bearing alloy, a niobium stabilized β phase could be increasing the TSS_d of HANA-4, as reported by Khatamian [32] for other Zr-Nb alloys [7].

The annealing temperature, 550 °C, is the reported α→β transition temperature, at elevated hydrogen concentration, in the H-Zr system. This is the high temperature limit of the Kearns line [14]. Because the β phase is metastable, and its stability is impacted by temperature, it is unclear how annealing may have impacted the HANA-4 microstructure. Annealing may have caused decomposition of the β phase, as discussed by Khatamian [32], this is especially true for the first anneal of 60 minutes at 540 °C. As described in §2.2, Figure 2.8, aging at elevated temperatures decomposes the β phase, lowering TSS_d to be consistent with Zircaloy-4. Alternatively, as the second anneal, 240 minutes at 550 °C is at the transition temperature, it may have partially regenerated the β phase resulting in an increase in TSS_d.

Only a small piece of the sample sent to IMR was retained, and that piece was mounted and polished to produce the micrograph shown in Figure 4.9. Thus the author was unable check for the presence of β phase through XRD. Even if enough material had been available, the β-Zr peaks would be difficult to distinguish from neighboring peaks in the Zr-H system, particularly δ-hydride.

5.2 Analysis of Differential Scanning Calorimetry Results

During the heating cycle most samples had an endothermic peak close to the annealing temperature. At first this seemed a good indication that these peaks are associated with hydride dissolution. The peak temperature (PT), onset, and maximum slope temperature (MST) for these peaks are plotted against the annealing temperature for HANA-4, Figure 5.1, and Zircaloy-4, Figure 5.3.

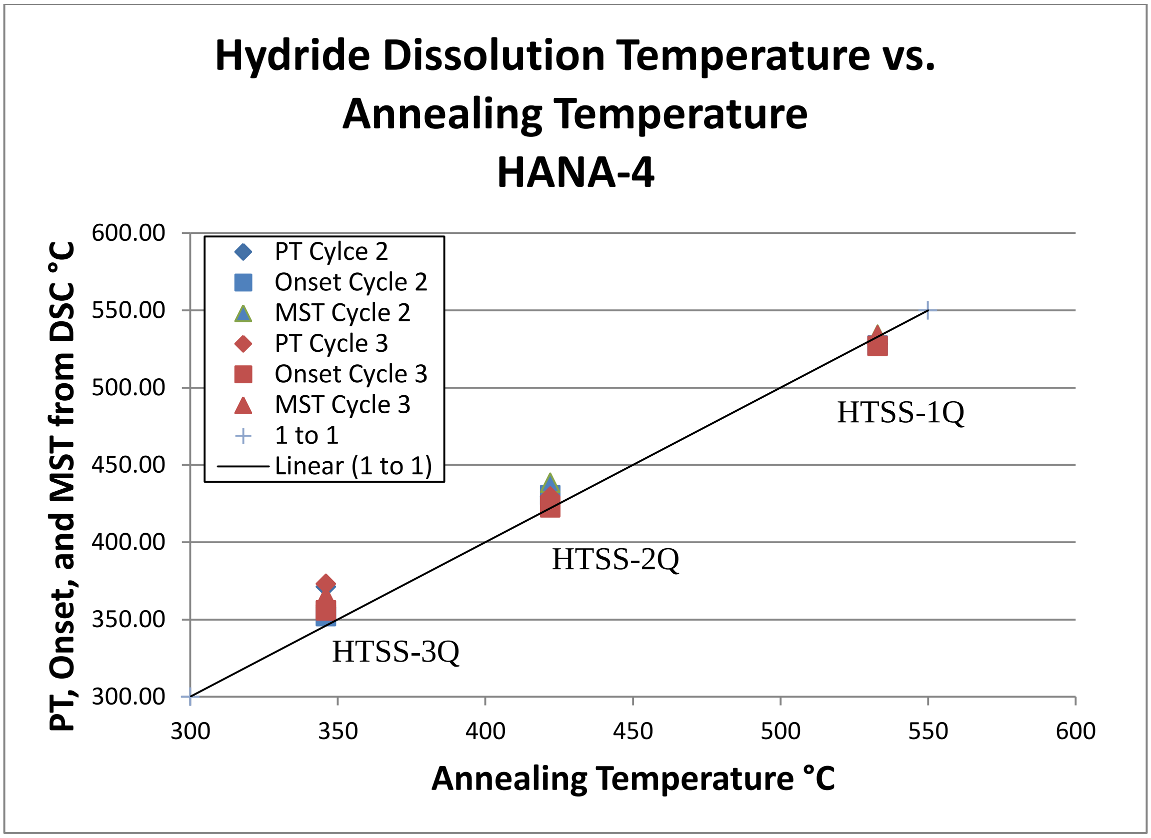

Fig. 5.1 HANA-4: Measured PT, Onset, and MST. Potential hydride dissolution peaks.

The plot shows a good agreement between the proposed hydride dissolution temperature and the annealing temperature. However, after comparison to peaks measured in a hydrogen free reference, §4.4.2 Figures 4.20 – 4.23, peaks associated with the uncharged alloys were removed (Figure 5.2).

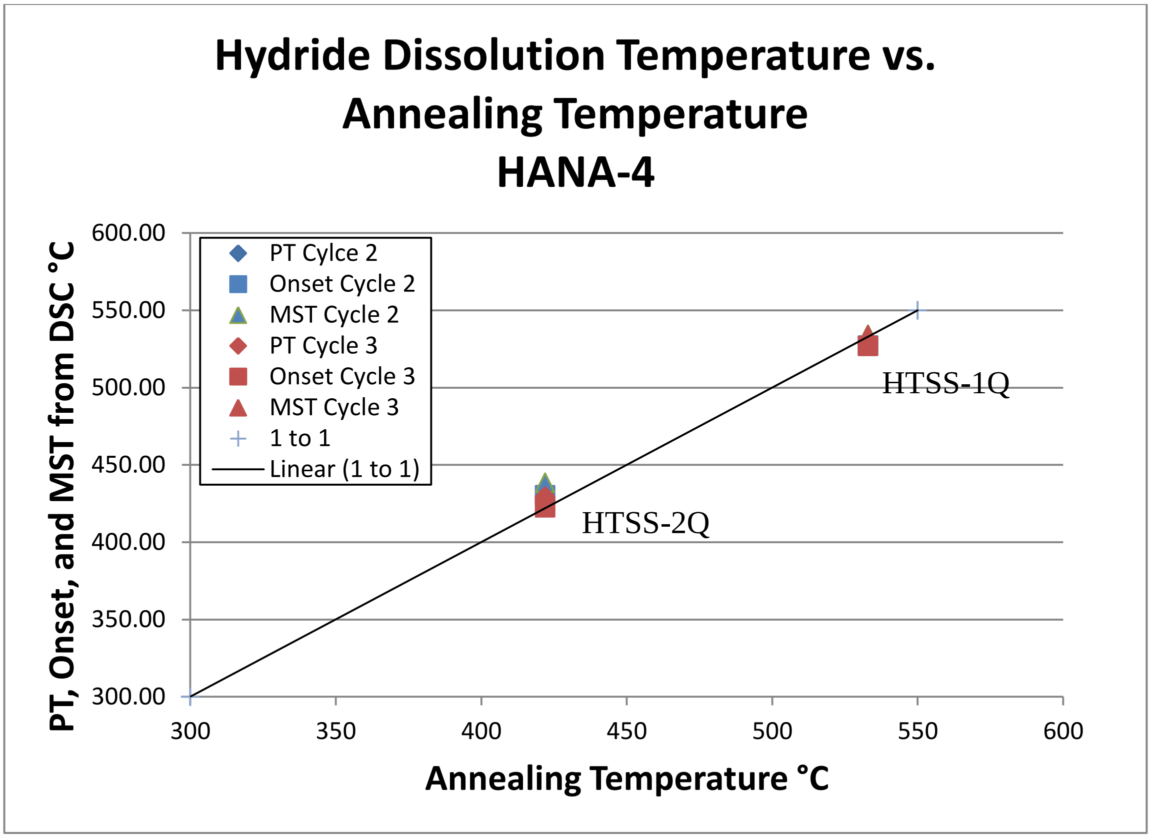

Fig. 5.2 HANA-4: Peaks attributable hydrogen dissolution.

Similarly, the potential hydride dissolution peaks observed in Zircaloy-4 are plotted against the annealing temperature (Figure 5.3), then peaks associated with the hydrogen free reference are removed (Figure 5.4).

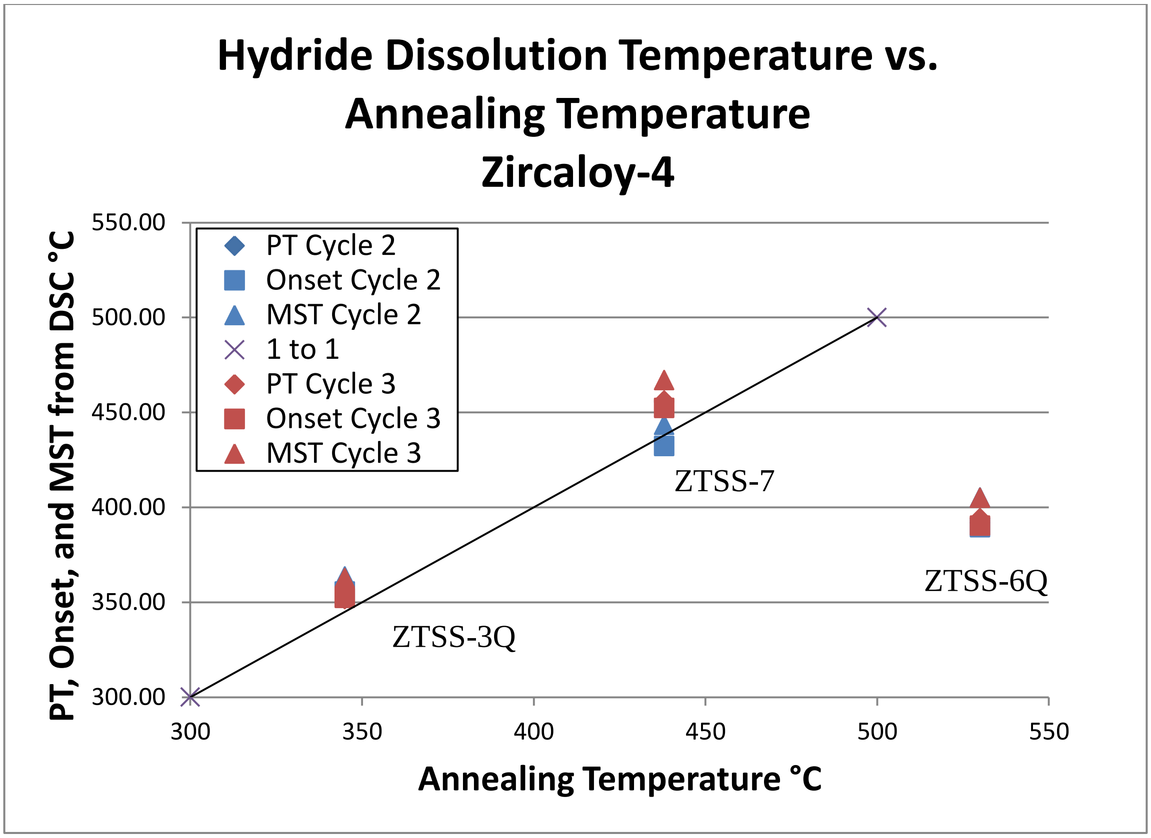

Fig. 5.3 Zircaloy-4: Measured PT, Onset, and MST. Potential hydride dissolution peaks.

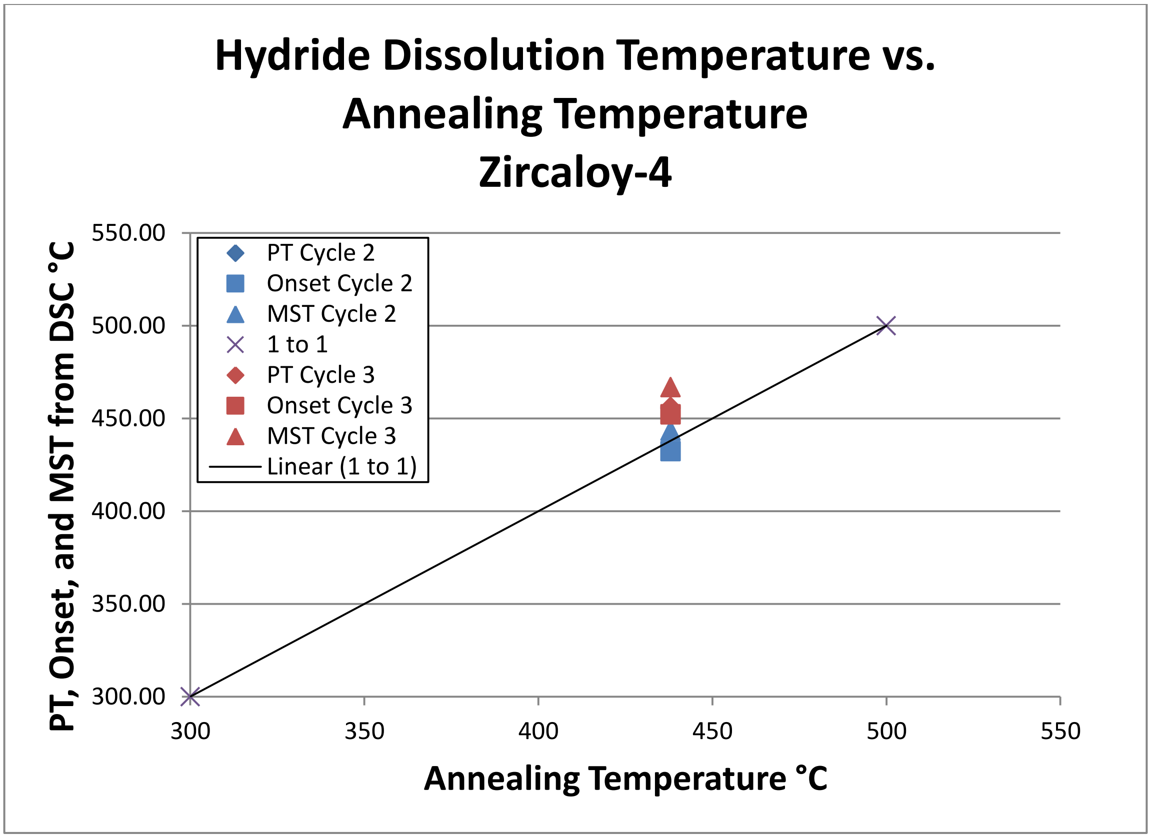

Fig. 5.4 Zircaloy-4: Peaks attributable hydrogen dissolution.

In ZTSS-6Q, which was annealed at 530 °C, the last peak is located near 390 °C. No peak corresponding to the annealing temperature is present. The last peak in this sample starts down at 359 °C (onset temperature) and levels off at 389 °C. This is similar to what is seen in HTSS-0Q and ZTSS-0Q, the as received reference samples. As would be expected, given their appearance in the reference samples, these features are present in all other samples. The feature is incomplete in HTSS-3Q and ZTSS-3Q, as the temperature program only went to 380 °C; short of the turning point at 400 °C. Sample HTSS-1Q does not have the sharp drop at 350 °C, but there are inflections in the curve at 353 °C and 400 °C, matching the behavior of the other samples. Therefore, although the dip at 355 °C corresponds to the annealing temperature of 345 °C used for HTSS-3Q and ZTSS-3Q, its appearance in all the samples, especially the as received references, is indicative of something intrinsic to the system, independent of hydrogen concentration and alloy. It is unclear to this author what this feature may represent. It is present in both alloys in the charged and uncharged condition, but seems absent in the work of other researchers K. Une *et al*, [18]. A complete list of onset temperatures for all features observed during heating and cooling is given in Appendix C, Table C.1 and Table C.2. The average onset temperatures of features, in each sample, that are not seen in the hydrogen free references are listed in Table 5.1. Table 5.1 excludes features that were only present in one cycle during heating.

Table 5.1

Average Onset Temperatures of Hydrogen Bearing Samples: Heating (°C)

HTSS-1Q	476	495	528
HTSS-2Q	427		
HTSS-3Q			
ZTSS-6Q	266		
ZTSS-7Q	262	442	
ZTSS-3Q	274	322	

Thermal analysis is a difficult technique to master [83, 84]. Though every attempt at care was made with these measurements, the results proved inconclusive. The importance of establishing a baseline for the system cannot be overstated [83, 84]. The difficulty with the Netzsch measurements was the manner in which the signal was dominated by the baseline behavior of the system. The baseline behavior of the system should be thoroughly recorded for each temperature profile using hydrogen free reference samples within 1 mg of the hydrided sample mass. It may be necessary to place such a hydrogen free reference in the reference sample cup, as reported by Khatamian [23] and Vizcaino *et al* [20]. This was attempted once using the Netzsch instrument, but the result proved inconclusive. However, it may help hydride peaks stand out if the difference in temperature between the two samples is due entirely to the presence of hydride in the sample.

Additionally, greater care should be taken to remove oxide layers formed on samples during previous heating runs. As noted in Gmelin and Sarge [84], oxide layers must be removed prior to measurement in metal samples. While the post annealing oxide layer was removed on samples before DSC measurement in the Netzsch, removal of any post measurement oxide was not attempted prior to measurement with the TA Q600 instrument.

CHAPTER VI

SUMMARY AND RECOMMENDATIONS

6.1 Summary

Zircaloy-4 and HANA-4 were successfully charged with hydrogen through low temperature cathodic charging. Enough hydrogen was inserted through cathodic charging to create samples with hydrogen concentrations up to 860 wppm in Zircaloy-4 and 1600 wppm in HANA-4. These concentrations are consistent with cladding from high burn up fuel, C_H 300 – 800 wppm, where C_H is hydrogen concentration. The charged specimens were annealed to create specimens with uniform bulk-hydrogen concentrations and hydride morphology. Annealing was carried out at 540 °C, 450 °C, and 350 °C, resulting in a range of bulk hydrogen concentrations, within the range of interest for nuclear fuel cladding in reactor and during dry storage.

During each phase of sample development, hydride morphology and hydride phases were characterized through back scattered electron imaging and x-ray diffraction. Hydride dissolution measurements, via differential scanning calorimetry, proved inconclusive, though there appeared to be a correlation between observed features and the annealing temperature in some specimens, in other specimens the observed features could not be distinguished from features in the uncharged alloys.

6.2 Future Work and Recommendations

A continuation of this effort requires the completion of the TSS measurements in HANA-4 and Zircaloy-4. The low temperature cathodic-charging system (LCS) has been shown to effectively insert hydrogen. Hydrogen charged zirconium alloy specimens are foundational to studying the impacts of hydrogen on zirconium alloys. Future work from this project could include the following.

1. Completion of the terminal solid solubility of hydrogen in HANA-4 and Zircaloy-4. To complete a measurement of TSS, the hydrogen concentrations of the DSC samples must be determined. Hydrogen concentration measurements are difficult with small sample sizes. IMR test labs required 2 g of material for hydrogen content analysis, and another lab required 6 g. With DSC coupons on the order of 50 mg or less, it is necessary to find a facility or instrument capable of measuring hydrogen in small samples.
2. The geometric difference between alloys should be removed. While it did not prevent charging, this additional variable made it difficult to determine the cause of differences in the materials charging behavior.
3. The low temperature cathodic charging system (LCS), would benefit from modifying or replacing the current level switch probe; in order to make the level control more reliable. The difference in rim thickness between the Zircaloy-4 samples is likely due to dilution of the electrolyte during the charging of Zr4H-3. This dilution resulted from a malfunction in the level switch probe, which caused

the pump overfill the reaction vessel. The probe was also prone to shorting the level switch circuit by making contact with the sample. In such situations, the electrolyte level was depleted, due to evaporation.

REFERENCES

[1] B. Cox, R. Peter, Hydriding Mechanisms and Impact on Fuel Performance, ZIRAT, Advanced Nuclear Technology, Uppsala, Sweden, 2000.

[2] International Atomic Energy Agency, Delayed Hydride Cracking in Zirconium Alloys in Pressure Tube Nuclear Reactors, IAEA TECDOC 1410, IAEA, Vienna, 2004.

[3] International Atomic Energy Agency, Delayed Hydride Cracking of Zirconium Alloy Fuel Cladding, IAEA TECDOC 1649, IAEA, Vienna, 2010.

[4] R.E. Einziger, H. Tsai, M. Billone, B.A. Hilton, Examination of Spent PWR Fuel Rods After 15 Years in Dry Storage, NUREG/CR-6838, Office of Nuclear Regulatory Research, U.S. Nuclear Regulatory Commission, Washington, DC, 2003.

[5] D.B. Rigby, Evaluation of the Technical Basis for Extended Dry Storage and Transportation of Used Nuclear Fuel, U.S. Nuclear Waste Technical Review Board, Washington DC, 2010.

[6] M.A. McKinnon, M.E. Cunningham, Dry Storage Demonstration for High-Burnup Spent Nuclear Fuel-Feasibility Study, Pacific Northwest National Laboratory, Richland, WA, 2003.

[7] K.W. Song, Y.H. Jeong, K.S. Kim, J.G. Bang, T.H. Chun, H.K. Kim, K.N. Song, Nuclear Engineering and Technology 40 (2008) 21-36.

[8] D. Khatamian, Z.L. Pan, M.P. Puls, C.D. Cann, Journal of Alloys and Compounds 231 (1995) 488-493.

[9] M. Billone, Y. Yan, T. Burtseva, R.S. Daum, Cladding Embrittlement During Postulated Loss-of-Coolant Accidents, NUREG/CR-6967, Office of Nuclear Regulatory Research, U.S. Nuclear Regulatory Commision, Washington, DC, 2008.

[10] C.L. Whitmarsh, Review of Zircaloy-2 and Zircaloy-4 Properties Relevant to N.S. Savannah Reactor Design, U.S. Atomic Energy Commission, Washington, DC, 1962.

[11] R. Krishnan, M.K. Asundi, Indian Academy of Sciences 4 (1981) 41-56.

[12] International Atomic Energy Agency, Waterside Corrosion of Zirconium Alloys in Nuclear Power Plants, IAEA TECDOC 996, IAEA, Vienna, 1998.

[13] D. Khatamian, J.H. Root, Journal of Nuclear Materials 372 (2008) 106-113.

[14] J.J. Kearns, Journal of Nuclear Materials 22 (1967) 292-303.

[15] R.S. Daum, Hydride-Induced Embrittlement of Zircaloy-4 Cladding Under Plane-Strain Tension, Materials Science, Ph.D Dissertation, Pennsylvannia State University, State College, Pennsylvania, 2007.

[16] R.N. Singh, R. Kishore, S.S. Singh, T.K. Sinha, B.P. Kashyap, Journal of Nuclear Materials 325 (2004) 26-33.

[17] S.-J. Min, J.-J. Won, K.-T. Kim, Journal of Nuclear Materials 448 (2014) 172-183.

[18] K. Une, S. Ishimoto, Y. Etoh, K. Ito, K. Ogata, T. Baba, K. Kamimura, Y. Kobayashi, Journal of Nuclear Materials 389 (2009) 127-136.

[19] S. Yamanaka, M. Miyake, M. Katsura, Journal of Nuclear Materials 247 (1997) 315-321.

[20] P. Vizcaíno, A.D. Banchik, J.P. Abriata, Journal of Nuclear Materials 304 (2002) 96-106.

[21] J.H. Baek, Y.H. Jeong, Journal of Nuclear Materials 361 (2007) 30-40.

[22] International Atomic Energy Agency, Behaviour of High Corrosion Resistance Zr-based Alloys, Proceedings of a Technical Meeting on the State of the Art in Zirconium Alloys Development, Buenos Aires, Argentina, 2005.

[23] D. Khatamian, Journal of Nuclear Materials 405 (2010) 171-176.

[24] K. Une, S. Ishimoto, Journal of Nuclear Materials 322 (2003) 66-72.

[25] R.S. Daum, Y.S. Chu, A.T. Motta, Journal of Nuclear Materials 392 (2009) 453-463.

[26] L. Lanzani, M. Ruch, Journal of Nuclear Materials 324 (2004) 165-176.

[27] W.M. Small, J.H. Root, D. Khatamian, Journal of Nuclear Materials 256 (1998) 102-107.

[28] E. Zuzek, J.P. Abriata, Bulletin of Alloy Phase Diagrams 11 (1990) 11.

[29] J.S. Bradbrook, G.W. Lorimer, N. Ridley, Journal of Nuclear Materials 42 (1972) 142-160.

[30] M.P. Puls, The Effect of Hydrogen and Hydrides on the Integrity of Zirconium Alloy Components: Delayed Hydride Cracking, Springer, London, 2012.

[31] B.A. Cheadle, S.A. Aldridge, Journal of Nuclear Materials 47 (1973) 255-258.

[32] D. Khatamian, Journal of Alloys and Compounds 293–295 (1999) 893-899.

[33] D. Khatamian, Journal of Alloys and Compounds 356–357 (2003) 22-26.

[34] D. Khatamian, V.C. Ling, Journal of Alloys and Compounds 253–254 (1997) 162-166.

[35] B. Nath, G.W. Lorimer, N. Ridley, Journal of Nuclear Materials 58 (1975) 153-162.

[36] Z.L. Pan, I.G. Ritchie, M.P. Puls, Journal of Nuclear Materials 228 (1996) 227-237.

[37] A. McMinn, E.C. Darby, J.S. Schofield, The Terminal Solid Solubility of Hydrogen in Zirconium Alloys, G. P. Sabol, G. D. Moan (Eds.), Zirconium in the Nuclear Industry: Twelfth International Symposium, ASTM STP 1354, West Conshohocken, PA, 2000, pp. 173-195.

[38] M.P. Puls, Metallurgical Transactions A 21 (1990) 2905-2917.

[39] M.P. Puls, Journal of Nuclear Materials 399 (2010) 248-258.

[40] A.D. Lepage, W.A. Ferris, G.A. Ledoux, Procedure for Adding Hydrogen to Small Sections of Zirconium Alloys, Materials and Mechanics Branch, Chalk River Laboratories, Chalk River, Ontario, 1998.

[41] B. Cox, Journal of Alloys and Compounds 256 (1997) 244-246.

[42] P.A.C. Raynaud, A.S. Bielen, Cladding Hydrogen Based Regulations in the United States, Water Reactor Fuel Performance Meeting, United States Nuclear Regulatory Commission, Chengdu, China, 2011.

[43] Y. Liu, Q. Peng, W. Zhao, H. Jiang, Materials Chemistry and Physics 110 (2008) 56-60.

[44] A.J. Parkinson, Hydride Production in Zircaloy-4 as a Function of Time and Temperature, Texas A&M University, College Station, Texas, 2010.

[45] P. Vizcaino, P.C. Fagundez, A.D. Banick, Engineering 2 (2010) 573-579.

[46] E.D. Hindle, G.F. Slattery, Journal of the Institute of Metals 94 (1966) 245-249.

[47] J.T. John, P.K. De, H.S. Gadiyar, High Temperature Cathodic Charging of Hydrogen in Zirconium Alloys and Iron and Nickle Base Alloys, B.A.R.C External, Bhabha Atomic Research Centre, Bombay, 1991.

[48] Y. Choi, J.W. Lee, Y.W. Lee, S.I. Hong, Journal of Nuclear Materials 245 (1998) 124-130.

[49] M.A. Martín-Rengel, F.J. Gómez Sánchez, J. Ruiz-Hervías, L. Caballero, A. Valiente, Journal of Nuclear Materials 429 (2012) 276-283.

[50] J. Wei, P. Frankel, M. Blat, A. Ambard, R.J. Comstock, L. Hallstadius, S. Lyon, R.A. Cottis, M. Preuss, Corrosion Engineering, Science and Technology 47 (2012) 516-528.

[51] J.J. Kearns, Journal of Nuclear Materials 43 (1972) 330-338.

[52] J.J. Kearns, Journal of Nuclear Materials 27 (1968) 64-72.

[53] K.B. Colas, A.T. Motta, M.R. Daymond, M. Kerr, J.D. Almer, S.W. Dean, Journal of ASTM International 8 (2011) 1-17.

[54] M.P. Puls, S.-Q. Shi, J. Rabier, Journal of Nuclear Materials 336 (2005) 73-80.

[55] J.J. Kearns, C.R. Woods, Journal of Nuclear Materials 20 (1966) 241-261.

[56] H.-G. Kim, I.-H. Kim, B.-K. Choi, J.-Y. Park, Y.-H. Jeong, K.-T. Kim, Corrosion Science 52 (2010) 3162-3167.

[57] A. Strassar, R. Adamson, F. Gararolli, The Effect of Hydrogen on Zirconium Alloys Properties, ZIRAT, vol I, Advanced Nuclear Technology International, Skultuna, Sweden, 2008.

[58] R.S. Daum, S. Majumdar, Y. Liu, M. Billone, Journal of Nuclear Science and Technology 43 (2006) 1054-1067.

[59] Interim Staff Guidance-11 Revision 3: Cladding Considerations for the Transportation and Storage of Spent Fuel, Nuclear Regulatory Commission, Washington, DC, 2003.

[60] G.A. McRae, C.E. Coleman, B.W. Leitch, Journal of Nuclear Materials 396 (2010) 130-143.

[61] M.P. Puls, Journal of Nuclear Materials 393 (2009) 350-367.

[62] Y.S. Kim, Materials Science and Engineering: A 490 (2008) 146-150.

[63] Y.S. Kim, S.B. Ahn, Y.M. Cheong, Journal of Alloys and Compounds 429 (2007) 221-226.

[64] Y.S. Kim, K.S. Kim, Y.M. Cheong, Journal of Nuclear Science and Technology 43 (2006) 1120-1127.

[65] Y.S. Kim, S.J. Kim, K.S. Im, Journal of Nuclear Materials 335 (2004) 387-396.

[66] S. Sagat, C.K. Chow, M.P. Puls, C.E. Coleman, Journal of Nuclear Materials 279 (2000) 107-117.

[67] D.A. Scarth, E. Smith, Modelling Delayed Hydride Cracking in Zirconium Alloys, Karihaloo, B. L. (Eds.), IUTAM Symposium on Analytical and Computational Fracture Mechanics of Non-Homogeneous Materials, vol 97, Springer, Netherlands, 2002, pp. 155-165.

[68] A.A. Shmakov, B.A. Kalin, Y.G. Matvienko, R.N. Singh, P.K. De, Materials Science 40 (2004) 764-771.

[69] R.N. Singh, S. Roychowdhury, V.P. Sinha, T.K. Sinha, P.K. De, S. Banerjee, Materials Science and Engineering: A 374 (2004) 342-350.

[70] S.-Q. Shi, M.P. Puls, Advances in the Theory of Delayed Hydride Cracking in Zirconium Alloys, Scientific Document Distribution Office, AECL Research, Chalk River, Ontario, 1994.

[71] Y. Choi, J.W. Lee, Y.W. Lee, S.I. Hong, Journal of Nuclear Materials 256 (1998) 124-130.

[72] H.-G. Kim, B.-K. Choi, S.-Y. Park, Y.-I. Jung, D.-J. Park, J.-Y. Park, Journal of Nuclear Materials 426 (2012) 173-181.

[73] J.-Y. Park, S.J. Yoo, B.-K. Choi, Y.H. Jeong, Journal of Alloys and Compounds 437 (2007) 274-279.

[74] J.-Y. Park, S.J. Yoo, B.-K. Choi, Y.H. Jeong, Journal of Nuclear Materials 373 (2008) 343-350.

[75] J. Wei, Effect of Hydrogen on the Corrosion Performance of Zirconium Alloys, School of Materials, Ph.D Dissertation, University of Manchester, Manchester, 2012.

[76] W.E. Berry, D.A. Vaughan, E.L. White, Corrosion 17 (1961) 109-117.

[77] S.H. Kuhr, An Electrolytic Method to Form Zirconium Hydride Phases in Zirconium Alloys with Morphologies Similar to Hydrides Formed in Used Nuclear Fuel, Texas A&M University, College Station, Texas, 2012.

[78] The Science Behind Materials Preparation, A Guide to Materials Preparation and Analysis, Buehler SUM-MET, United States, 2004.

[79] K.B. Colas, Kinetics of Zirconium Hydride Precipitation and Reorientation Studied Using Synchrotron Radiation, Mechanical and Nuclear Engineering, MS Thesis, Pennsylvania State University, State College, Pennsylvania, 2009.

[80] P.A.C. Raynaud, Crack Growth Through the Thickness of Thin Sheet Hydrided Zircaloy-4, Materials Science and Engineering, Ph.D Dissertation, Pennsylvania State University, State College, Pennsylvania, 2009.

[81] H.E. Swanson, H.F. McMurdie, M.C. Morris, E.H. Evans, Standard X-ray Diffraction Powder Patterns: Section 5. Data for 80 Substances, NBS Monograph Series, U.S Department of Commerce. National Bureau of Standards, Washington, DC, 1967.

[82] J.-Y. Park, B.-K. Choi, Y.H. Jeong, Special Issue on the Water Reactor Fuel Performance Meeting 2008 41 (2009).

[83] D. Chen, A. Green, D. Dollimore, Thermochimica Acta 284 (1996) 429-433.

[84] E. Gmelin, S.M. Sarge, Pure & Applied Chemistry 67 (1995) 1789-1800.

[85] H. Zou, G.M. Hood, J.A. Roy, R.J. Schultz, J.A. Jackman, Journal of Nuclear Materials 210 (1994) 239-243.

[86] H. Zou, G.M. Hood, H. Nakajima, J.A. Roy, R.J. Schultz, Journal of Nuclear Materials 223 (1995) 186-188.

[87] R.L. Hervig, F.K. Mazdab, G. Moore, P.F. McMillan, Analyzing Hydrogen (H2O) in Silicate Glass by Secondary Ion Mass Spectrometry and Reflectance Fourier Transform Infrared Spectroscopy, V. Benedetto De, R. J. Bodnar (Eds.), Developments in Volcanology, Volume 5, Elsevier, 2003, pp. 83-103.

APPENDIX A

ADDITIONAL X-RAY DIFFRACTION DATA

Table A.1

XRD Peaks for Zironium Hydrogen System

Zirconium and Zirconium Hydrides Peaks: Range 48-72 in 2θ								
Zr	Intensity	δ-$ZrH_{1.66}$	Intensity	γ-ZrH	Intensity	ε-ZrH_2	Intensity	ZrO
α-48.0	17	54.2	37	54.3	24	51.9	12	56.1
β-51.5	17	64.6	43	56.6	11	55.3	18	67.1
α-56.9	17	67.8	12	62.9	16	62.5	20	70.6
α-63.5	18			67.0	14	67.8	8	
β-64.3	33			69.0	13	68.6	8	
α-66.8	3							
α-68.5	18							
α-69.6	12							

Zirconium and Zirconium Hydrides Peaks: Range 48-72 in 2θ					
α-Zr	β-Zr	δ-$ZrH_{1.66}$	γ-ZrH	ε-ZrH_2	ZrO
48.0	51.5	54.2	54.3	51.9	56.1
56.9	64.3	64.6	56.6	55.3	67.1
63.5		67.8	62.9	62.5	70.6
66.8			67.0	67.8	
68.5			69.0	68.6	
69.6					

α-Zr	48.0	56.9	63.5	66.8	68.5	69.6
β-Zr	51.5	64.3				
δ-ZrH1.66	54.2	64.6	67.8			
γ-ZrH	54.3	56.6	62.9	67.0	69.0	
ε-ZrH2	51.9	55.3	62.5	67.8	68.6	
ZrO	56.1	67.1	70.6			

XRD Plots:

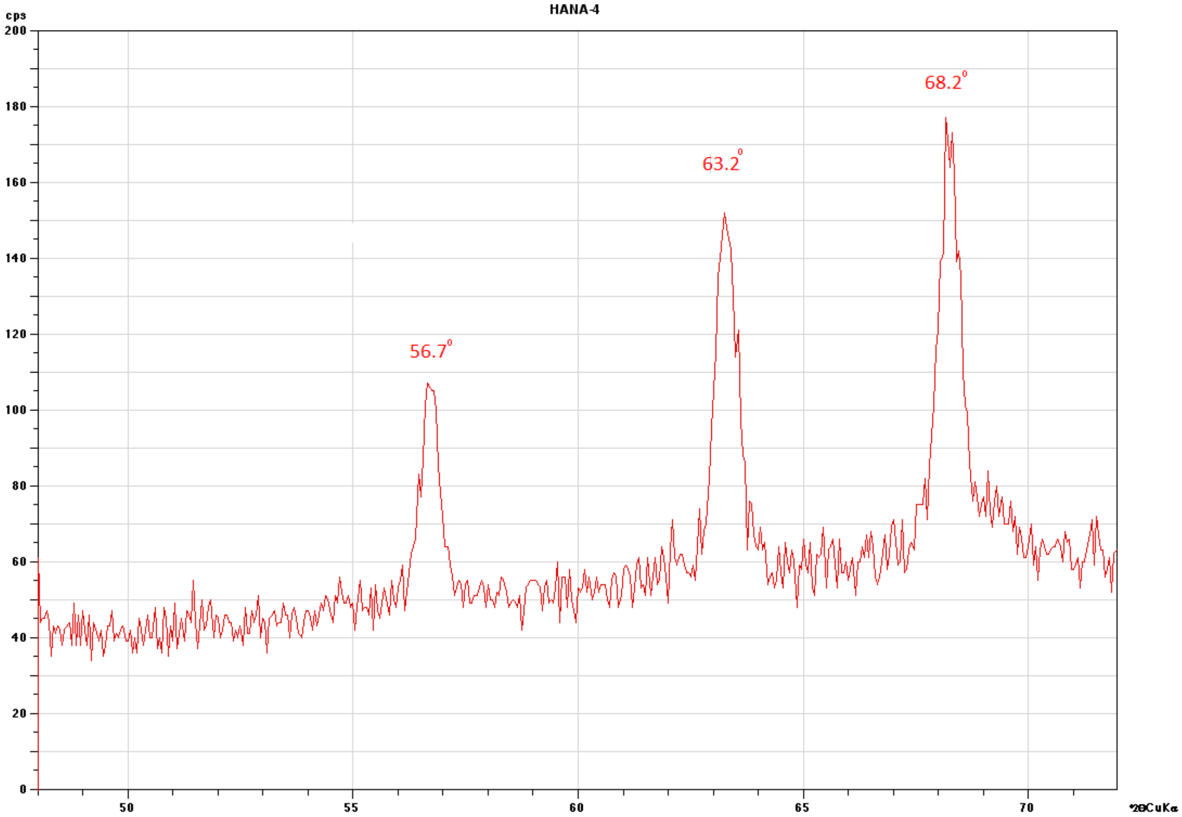

Fig. A.1 Uncharged HANA-4

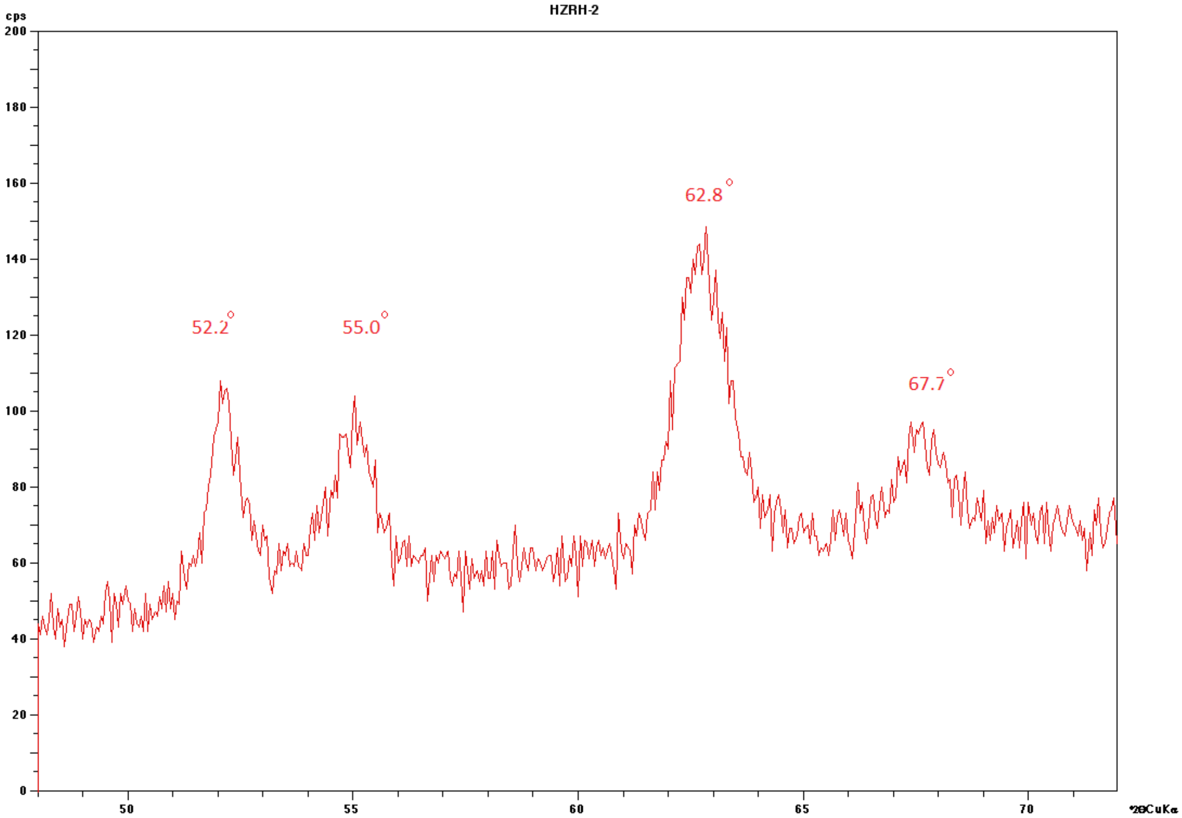

Fig. A.2 Charged HANA-4, HZrH-2.

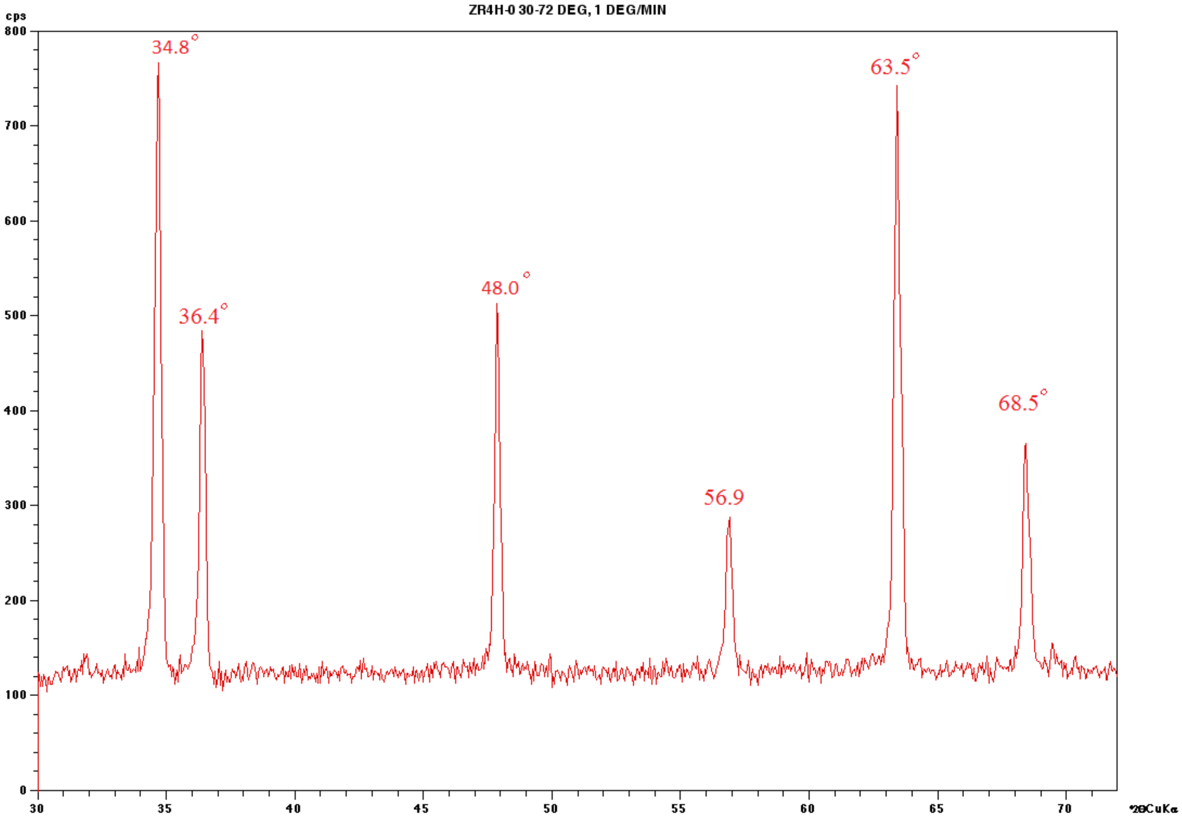

Fig A.4 Uncharged Zircaloy-4: 30°-72° in 2θ.

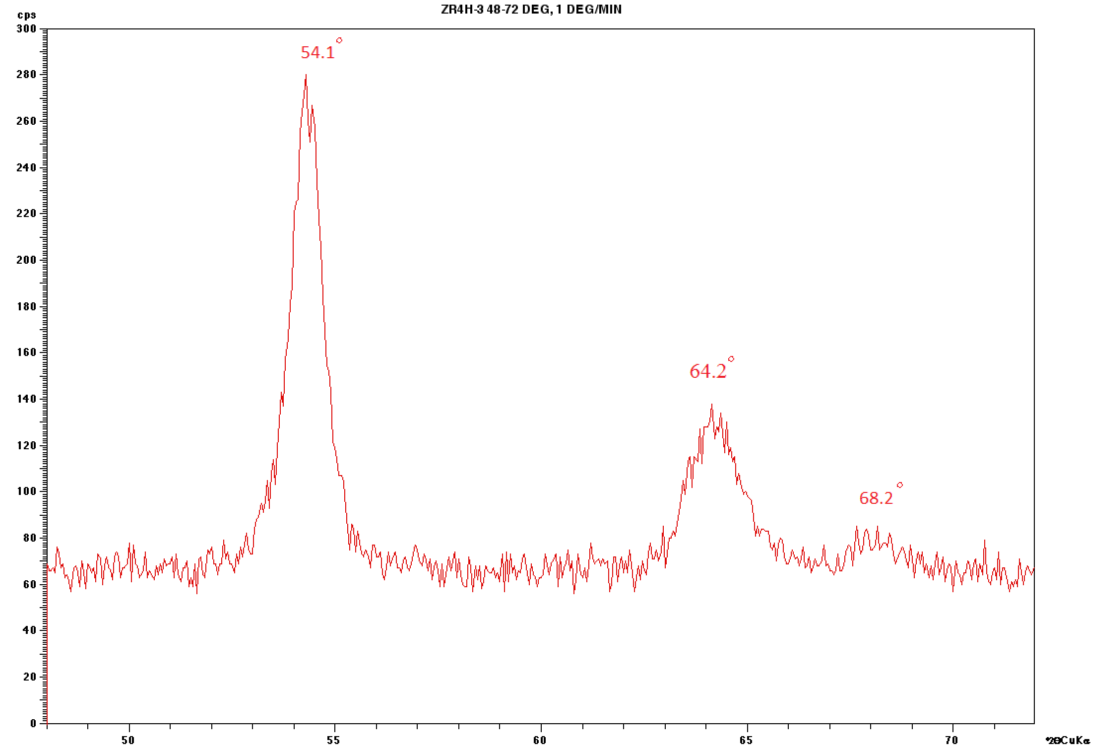

Fig. A.5 Charged Zircaloy-4, Zr4H-3.

APPENDIX B

IMR TEST LAB MEASUREMENTS

Table B.1

Elemental Analysis of Zircaloy-4

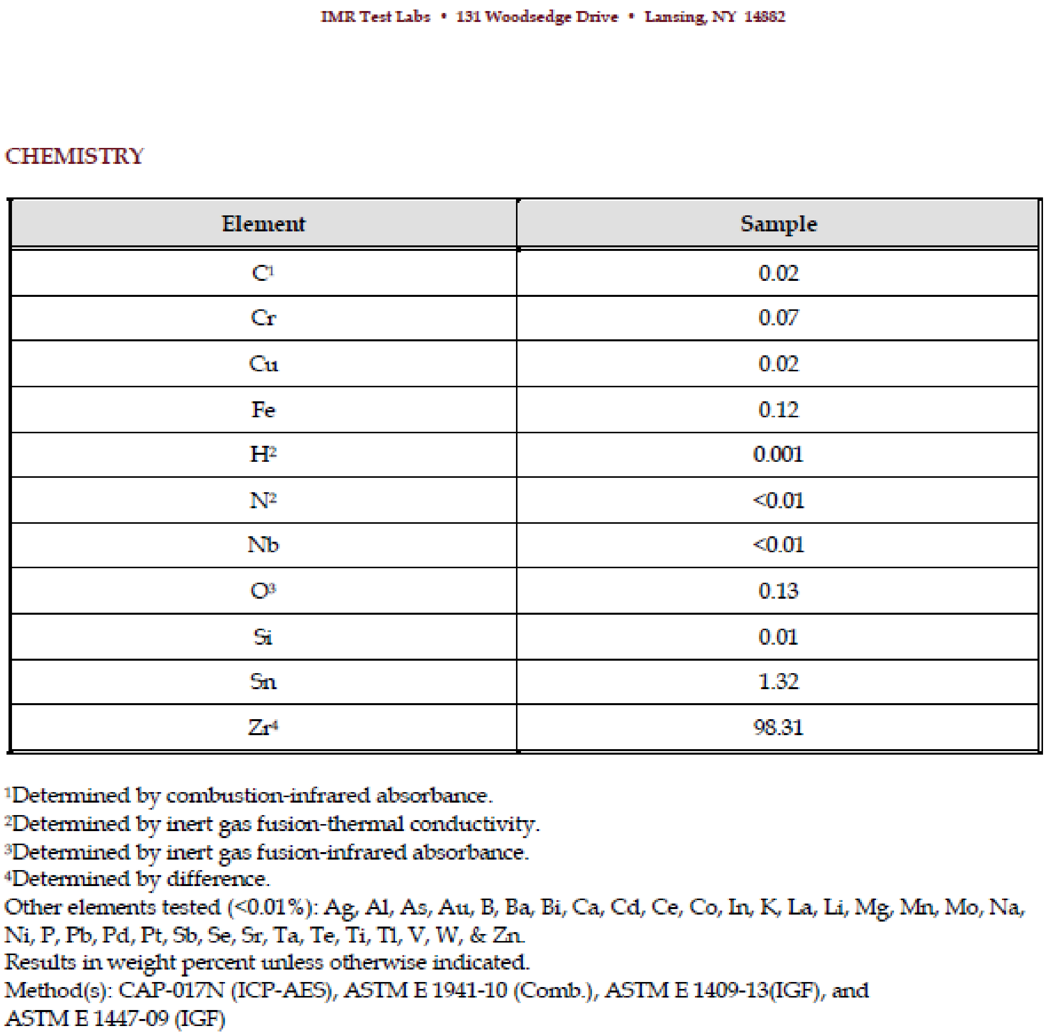

IMR Test Labs • 131 Woodsedge Drive • Lansing, NY 14882

CHEMISTRY

Element	Sample
C[1]	0.02
Cr	0.07
Cu	0.02
Fe	0.12
H[2]	0.001
N[2]	<0.01
Nb	<0.01
O[3]	0.13
Si	0.01
Sn	1.32
Zr[4]	98.31

[1] Determined by combustion-infrared absorbance.
[2] Determined by inert gas fusion-thermal conductivity.
[3] Determined by inert gas fusion-infrared absorbance.
[4] Determined by difference.

Other elements tested (<0.01%): Ag, Al, As, Au, B, Ba, Bi, Ca, Cd, Ce, Co, In, K, La, Li, Mg, Mn, Mo, Na, Ni, P, Pb, Pd, Pt, Sb, Se, Sr, Ta, Te, Ti, Tl, V, W, & Zn.
Results in weight percent unless otherwise indicated.
Method(s): CAP-017N (ICP-AES), ASTM E 1941-10 (Comb.), ASTM E 1409-13(IGF), and
ASTM E 1447-09 (IGF)

Table B.2

Hydrogen Content Measurement Zr4H-3

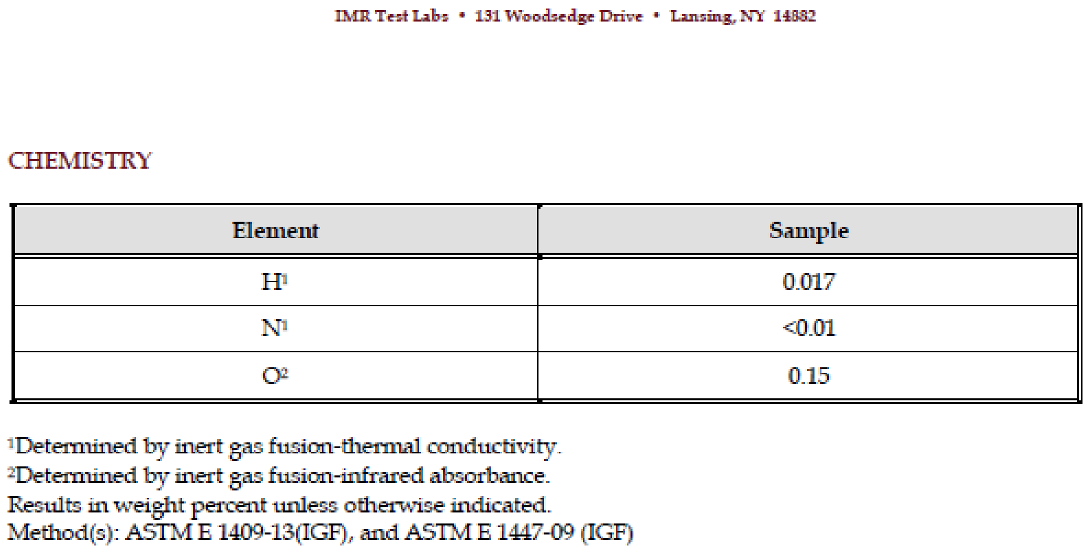

IMR Test Labs • 131 Woodsedge Drive • Lansing, NY 14882

CHEMISTRY

Element	Sample
H[1]	0.017
N[1]	<0.01
O[2]	0.15

[1] Determined by inert gas fusion-thermal conductivity.
[2] Determined by inert gas fusion-infrared absorbance.
Results in weight percent unless otherwise indicated.
Method(s): ASTM E 1409-13(IGF), and ASTM E 1447-09 (IGF)

Table B.3

Elemental Analysis HANA-4

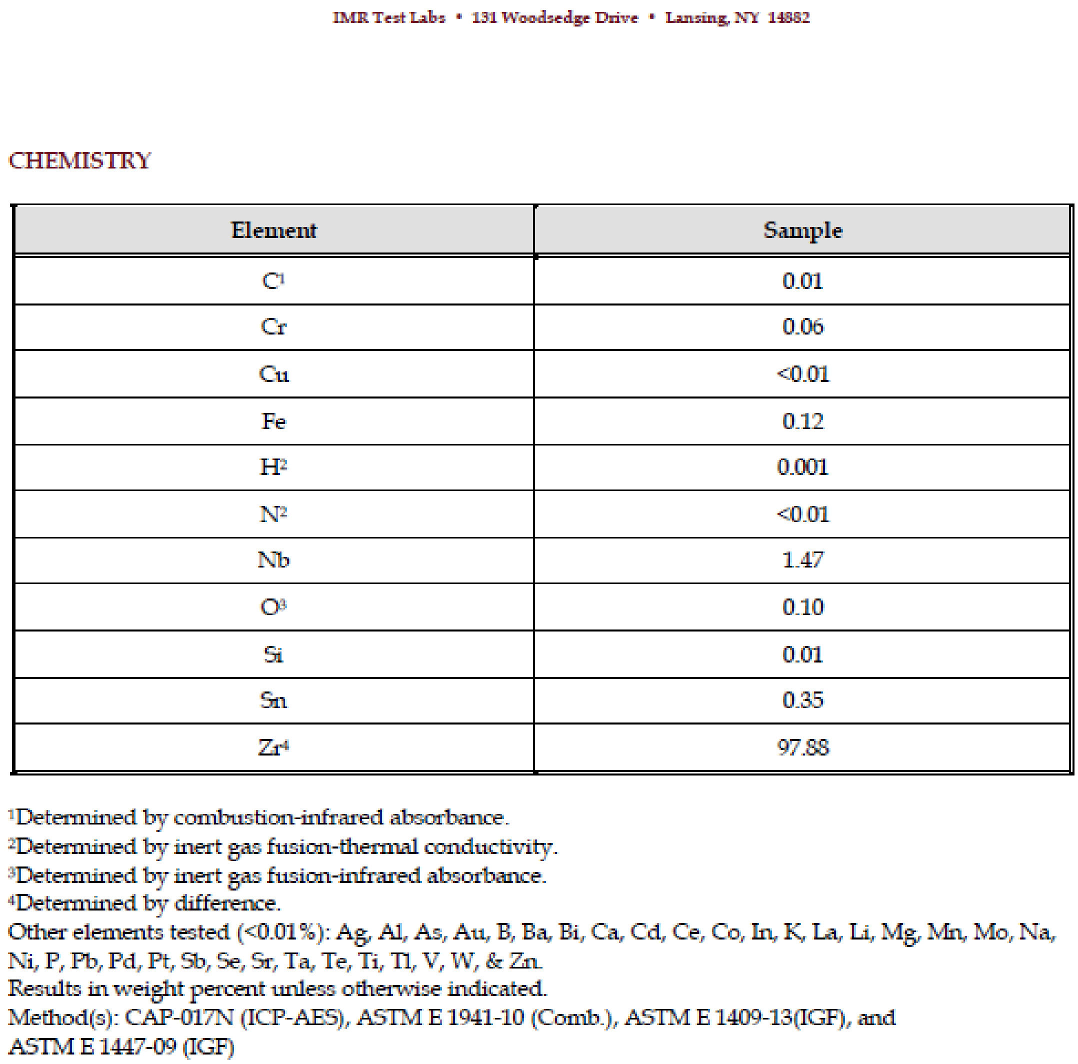

IMR Test Labs • 131 Woodsedge Drive • Lansing, NY 14882

CHEMISTRY

Element	Sample
C[1]	0.01
Cr	0.06
Cu	<0.01
Fe	0.12
H[2]	0.001
N[2]	<0.01
Nb	1.47
O[3]	0.10
Si	0.01
Sn	0.35
Zr[4]	97.88

[1] Determined by combustion-infrared absorbance.
[2] Determined by inert gas fusion-thermal conductivity.
[3] Determined by inert gas fusion-infrared absorbance.
[4] Determined by difference.
Other elements tested (<0.01%): Ag, Al, As, Au, B, Ba, Bi, Ca, Cd, Ce, Co, In, K, La, Li, Mg, Mn, Mo, Na, Ni, P, Pb, Pd, Pt, Sb, Se, Sr, Ta, Te, Ti, Tl, V, W, & Zn.
Results in weight percent unless otherwise indicated.
Method(s): CAP-017N (ICP-AES), ASTM E 1941-10 (Comb.), ASTM E 1409-13(IGF), and ASTM E 1447-09 (IGF)

Table B.4

Hydrogen Content Measurement HZrH-2

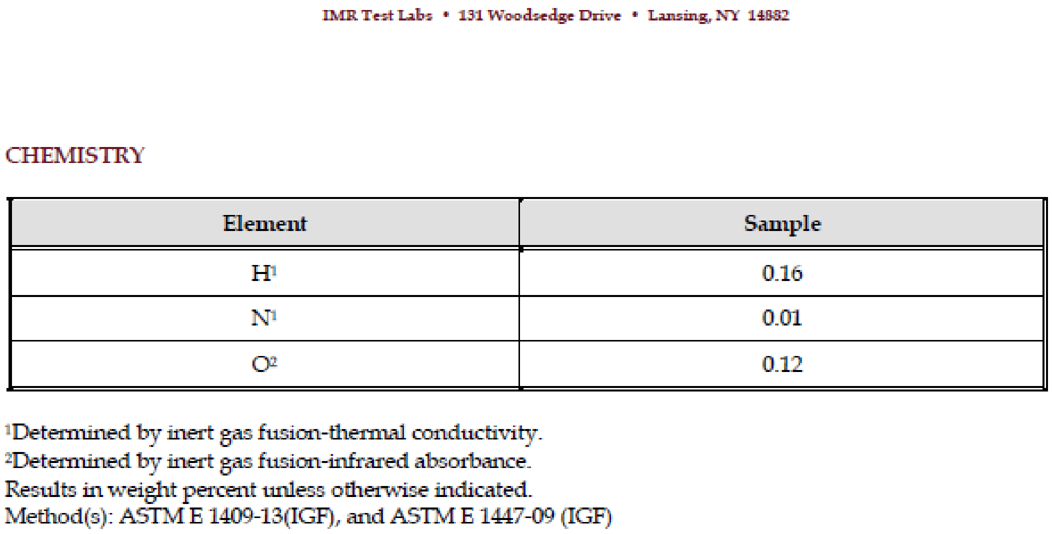

IMR Test Labs • 131 Woodsedge Drive • Lansing, NY 14882

CHEMISTRY

Element	Sample
H[1]	0.16
N[1]	0.01
O[2]	0.12

[1] Determined by inert gas fusion-thermal conductivity.
[2] Determined by inert gas fusion-infrared absorbance.
Results in weight percent unless otherwise indicated.
Method(s): ASTM E 1409-13(IGF), and ASTM E 1447-09 (IGF)

APPENDIX C

DIFFERENTIAL SCANNING CALORIMETRY RESULTS

Table C.1

Onset Temperatures for Features Observed During Heating (°C)

HTSS-1Q	1st	2nd	3rd	4th	5th	6th	7th	8th
Cycle 1	180.24	214.88	353.29	372.18	400.53	476.85	496.33	527.22
Cycle 2	180.27	215.30	352.29	375.33	400.80	474.19	495.41	526.97
HTSS-2Q								
Cycle 1	193.34	225.49	269.42	353.44	400.36	430.23		
Cycle 2	194.54	225.94	280.46	354.65	396.43	422.91		
HTSS-3Q								
Cycle 1	149.12	173.04	208.88	352.08				
Cycle 2	151.62	176.19	211.55	355.73				
HTSS-0Q								
Cycle 1	154.63	197.56	225.08	267.81	354.76	401.29	411.56	
Cycle 2	162.01	202.85	231.60		356.03	401.27	419.71	
ZTSS-6Q								
Cycle 1	154.97	175.35	224.26	272.06	359.37	389.47		
Cycle 2	162.33	178.88	221.17	260.43	360.50	390.39		
ZTSS-7Q								
Cycle 1	202.36	262.77	357.52	400.60	432.32			
Cycle 2	205.29	262.15	357.66	420.46	452.29			
ZTSS-3Q								
Cycle 1	151.15	180.40	215.89	264.03	277.82	296.94	327.13	355.68
Cycle 2	150.69	183.42	219.85	DNE	270.04	DNE	316.20	352.25
ZTSS-0Q								
Cycle 1	153.67	175.33	211.53	354.59	400.51			
Cycle 2	162.73	183.05	218.63	356.02	400.77			

Table C.2
Onset Temperatures for Features Observed During Cooling (°C)

HTSS-1Q	1st	2nd	3rd	4th	5th	6th	7th	8th
Cycle 1	487.20	462.33	426.90	342.88	309.27	292.23	238.13	198.75
Cycle 2	485.88	460.66	435.68	398.72	356.87	323.44	306.96	264.28
HTSS-2Q								
Cycle 1	429.90	366.85	323.38					
Cycle 2	411.27	366.28	333.01					
HTSS-3Q								
Cycle 1	323.28	313.19						
Cycle 2	323.95	315.47						
HTSS-0Q								
Cycle 1	468.04							
Cycle 2	467.12							
ZTSS-6Q								
Cycle 1	480.80	450.68	435.84					
Cycle 2	501.91	449.48						
ZTSS-7Q								
Cycle 1	381.75	339.99						
Cycle 2	377.64	339.21						
ZTSS-3Q								
Cycle 1	355.61	307.90	278.33					
Cycle 2	357.06	309.30	298.95	240.26				
ZTSS-0Q								
Cycle 1	469.93	442.21	399.35	337.43	269.03			
Cycle 2	469.65	426.65	399.18	337.34				

Most of the features identified during cooling are inflection points or step transitions. The only events that seem to be related to exothermic peaks are those at 431 °C, in HTSS-1Q, and at 480 °C, in ZTSS-6Q. The cooling data from the Netzsch instrument showed a cooling peak in HTSS-2, PT 365 °C, in agreement with the feature at 367 °C measured here. However, the lack of agreement between other peaks measured with the Netzsch and those measured here precludes drawing conclusions from one agreement. In the absence of sharp readily observed exothermic peaks, no definite claims regarding precipitation can be made. The absence of precipitation peaks is troubling, and indicates that these measurements were insensitive to precipitation, calling into question the veracity of the HDT measurements.

While some of the features measured during heating may correspond to hydride dissolution, none of the measured curves contained an obvious hydride precipitation peakS upon cooling. Hydride dissolution is expected to be spread over a wide temperature range, precipitation; however, should produce a sharp exothermic peak [20]. Though numerous features on each cooling curve have been characterized, there is no criterion that can be consistently applied across samples to determine the hydride precipitation temperature.

Table C.3

Average Onset Temperatures of Hydrogen Bearing Samples: Cooling (°C)

HTSS-1Q	487	461	431	350	308
HTSS-2Q	421	367	328		
HTSS-3Q	314				
ZTSS-6Q	491	450			
ZTSS-7Q	380				
ZTSS-3Q	309				

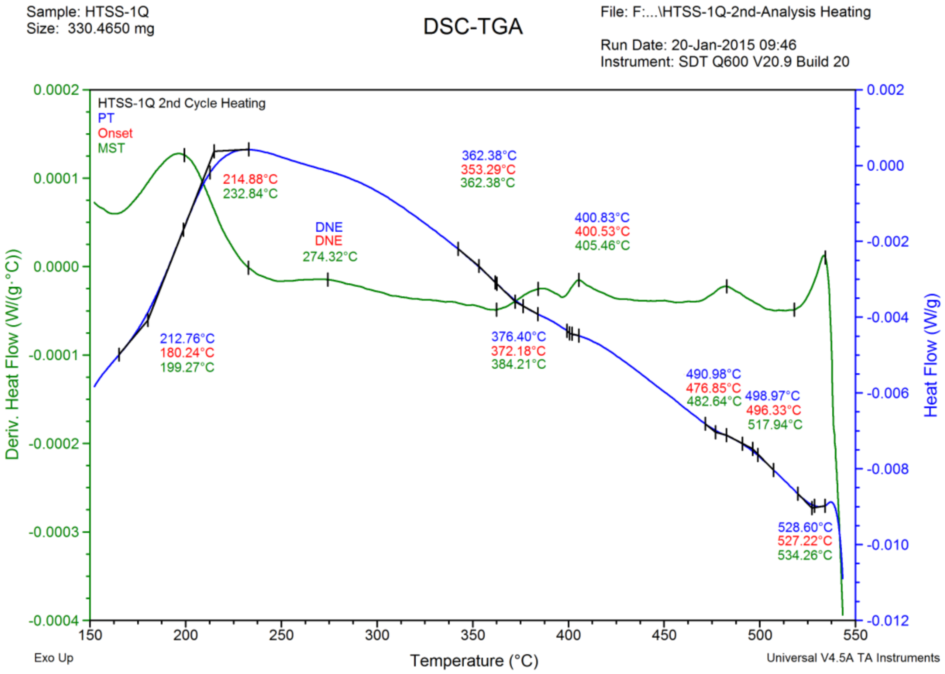

Fig. C.1 HTSS-1Q: Heating curve, Max Temperature 545 °C.

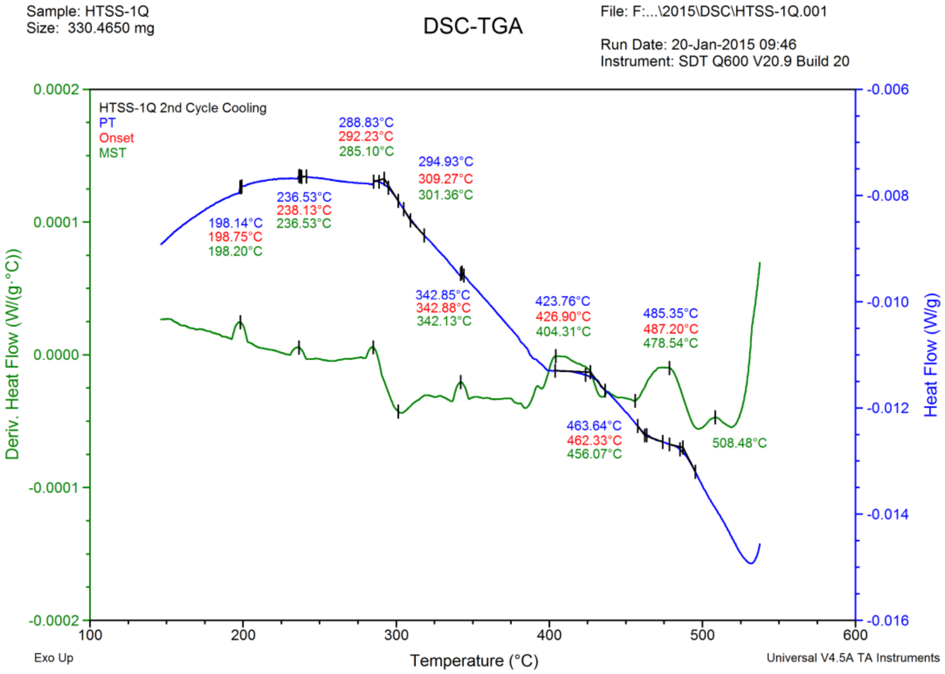

Fig. C.2 HTSS-1Q: Cooling curve, Max Temperature 545 °C.

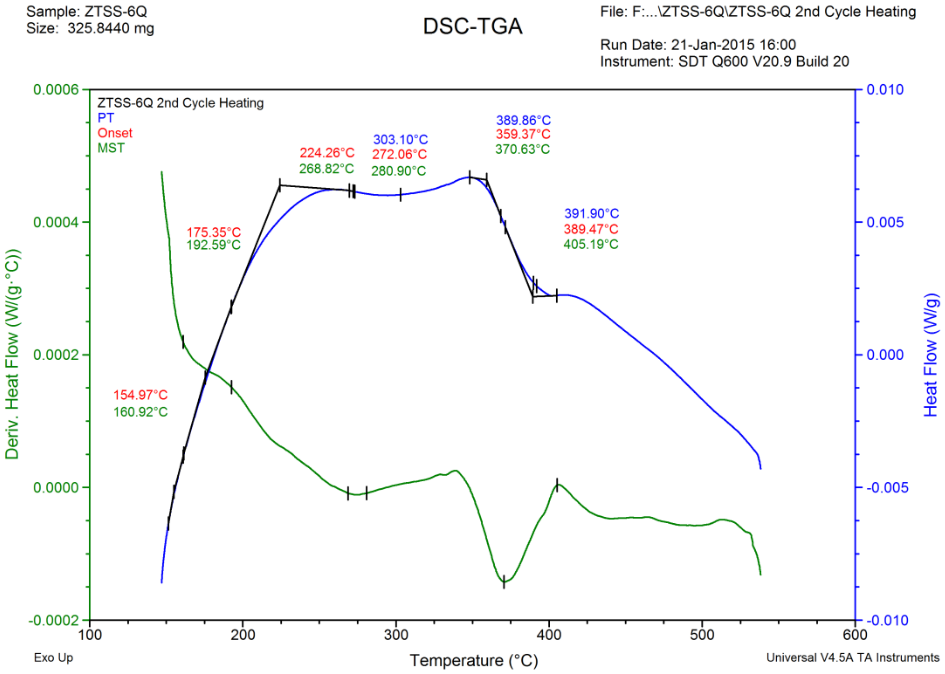

Fig. C.3 ZTSS-6Q: Heating curve, Max Temperature 545 °C.

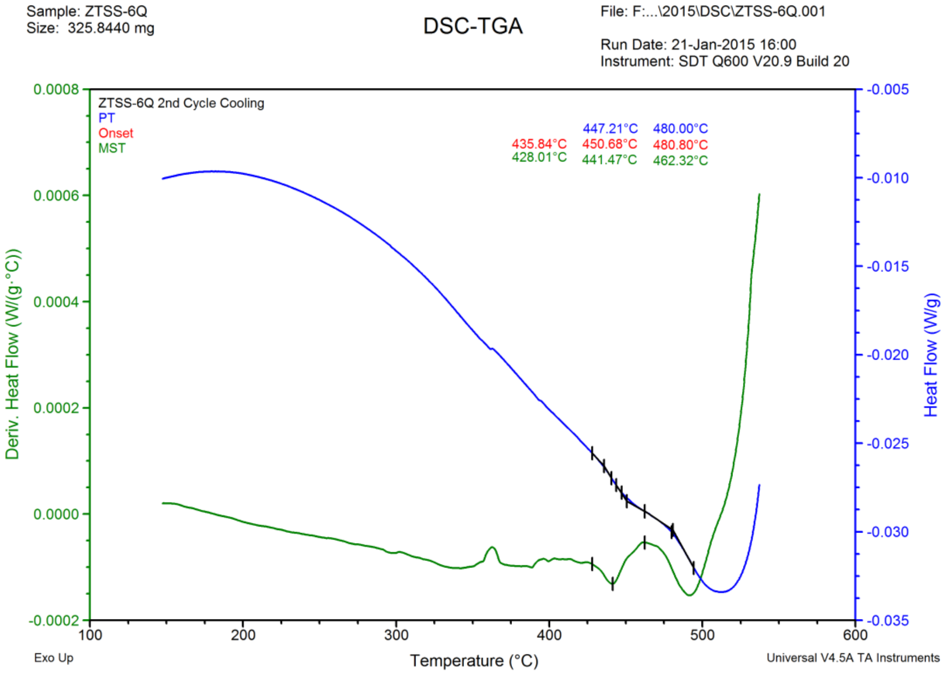

Fig. C.4 ZTSS-6Q: Cooling curve, Max Temperature 545 °C.

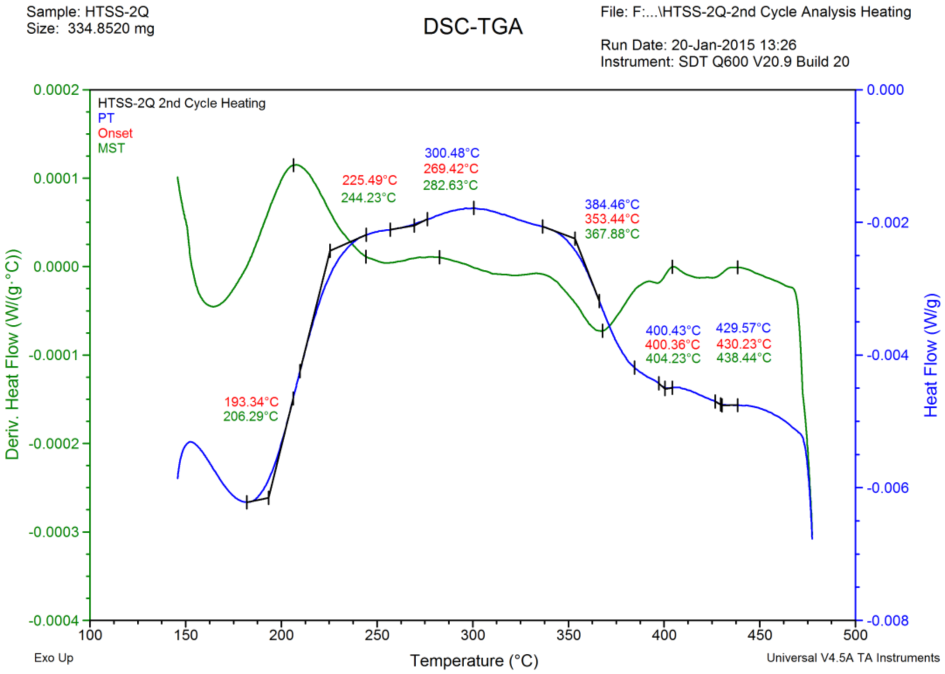

Fig. C.5 HTSS-2Q: Heating curve, Max Temperature °C.

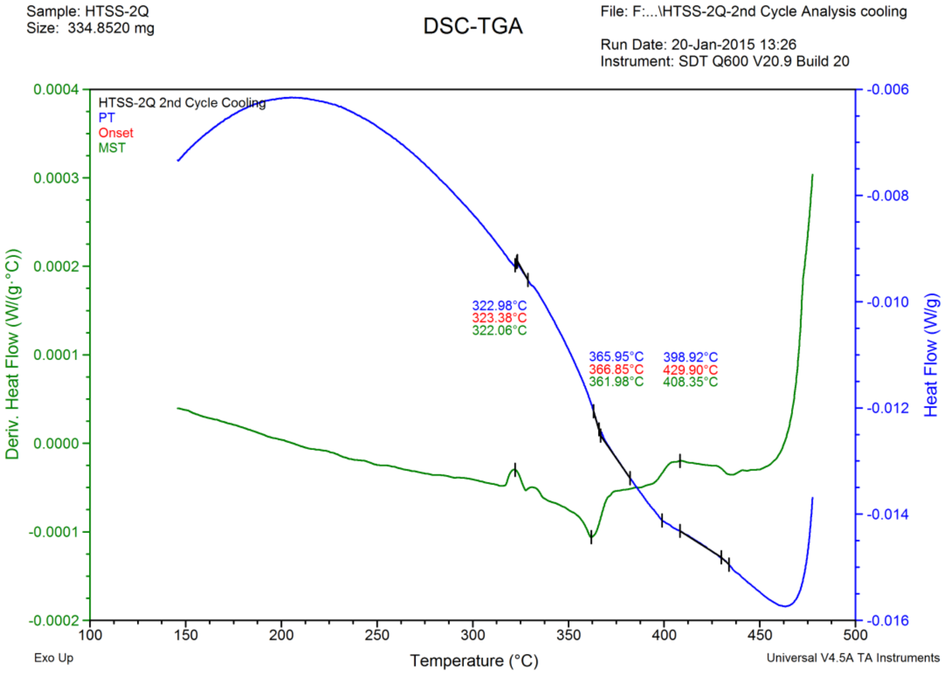

Fig. C.6 HTSS-2Q: Cooling curve, Max Temperature °C.

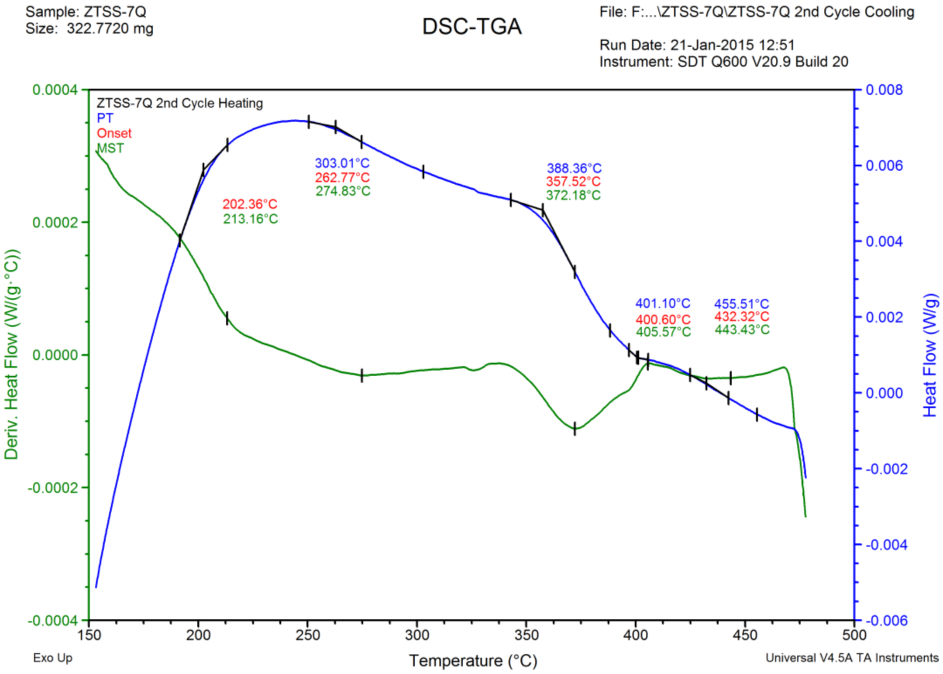

Fig. C.7 ZTSS-7Q: Heating curve, Max Temperature 480 °C.

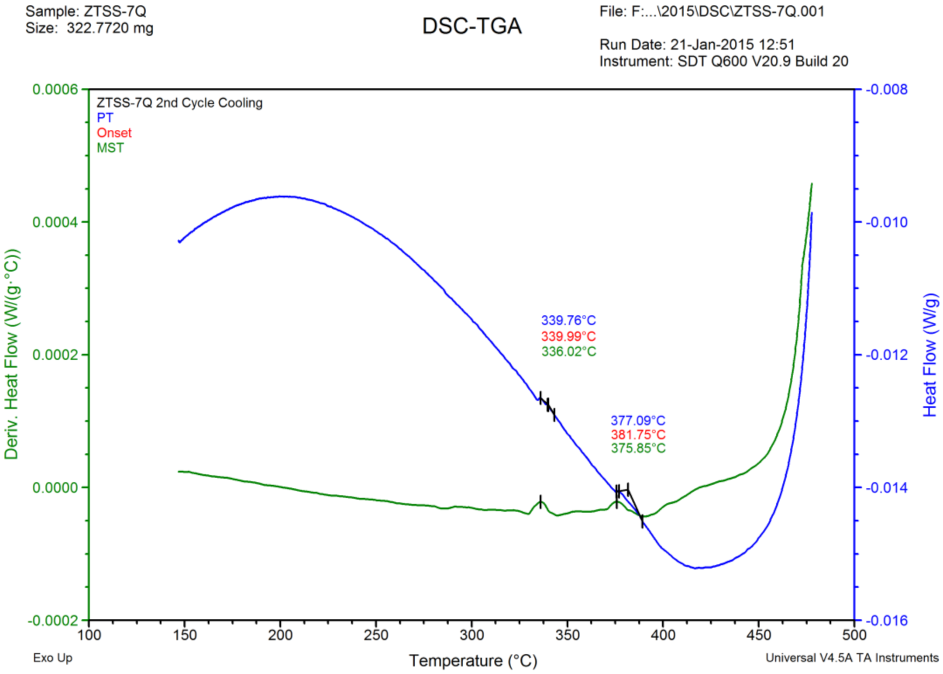

Fig. C.8 ZTSS-7Q: Cooling curve, Max Temperature 480 °C.

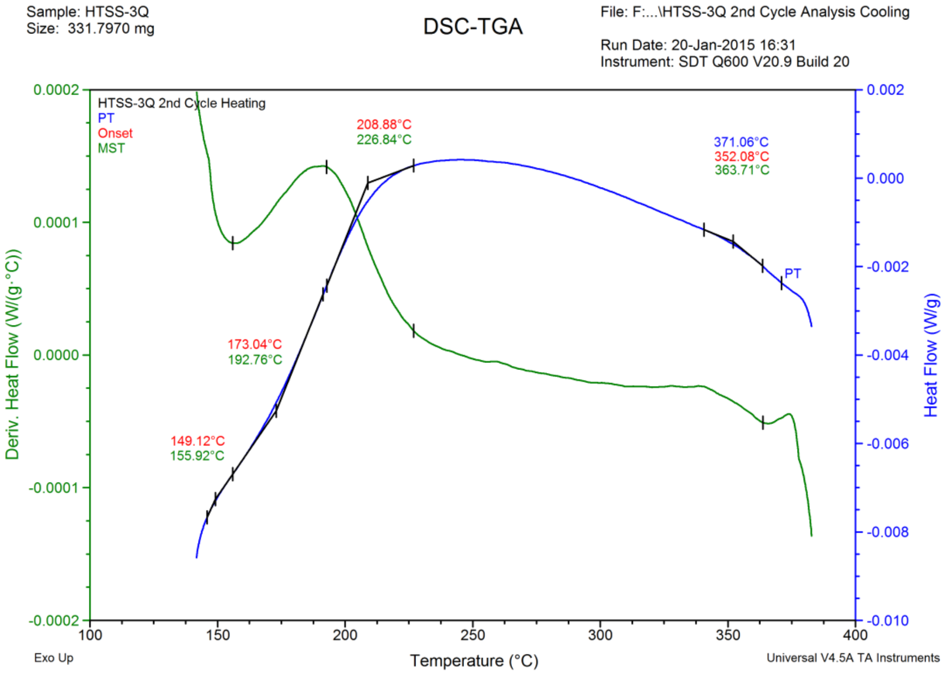

Fig. C.9 HTSS-3Q: Heating curve, Max Temperature 380 °C.

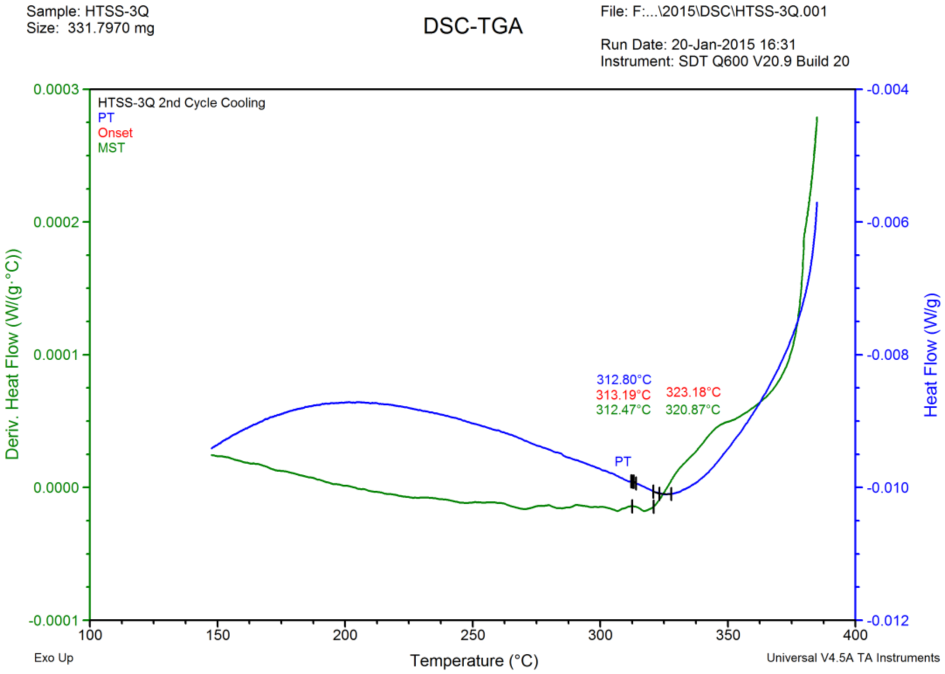

Fig. C.10 HTSS-3Q: Cooling curve, Max Temperature 380 °C.

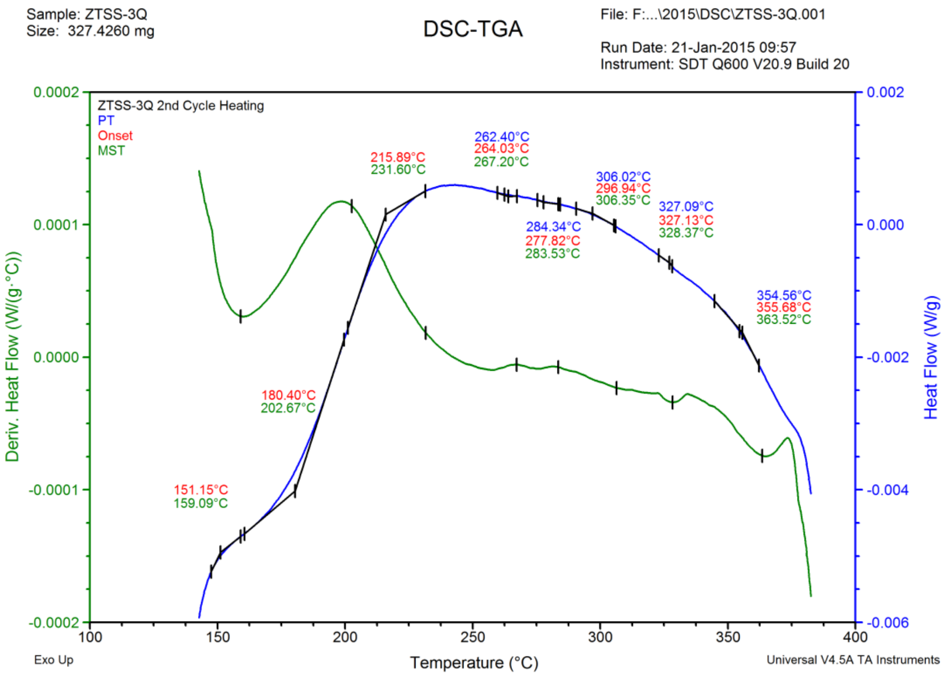

Fig. C.11 ZTSS-3Q: Heating curve, Max Temperature 380 °C.

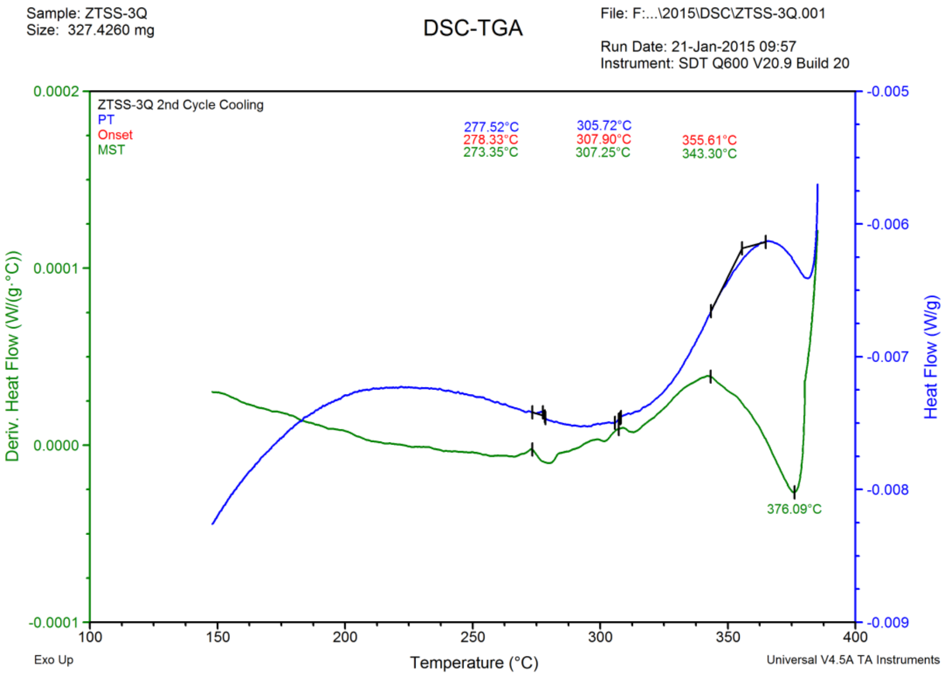

Fig. C.12 ZTSS-3Q: Cooling curve, Max Temperature 380 °C.

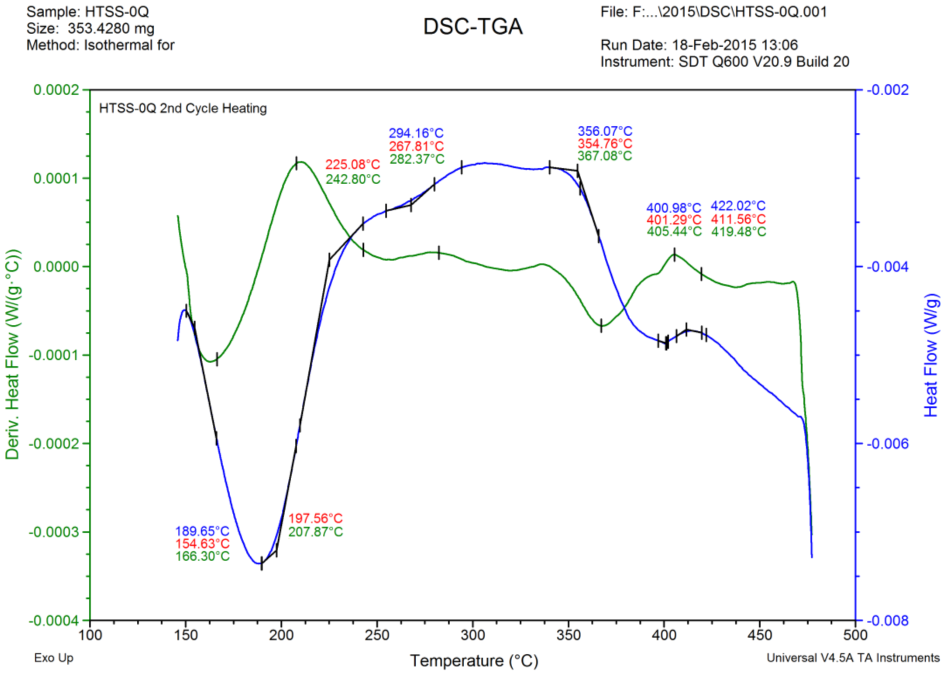

Fig. C.13 HTSS-0Q As received material: Heating curve, Max Temperature 480 °C.

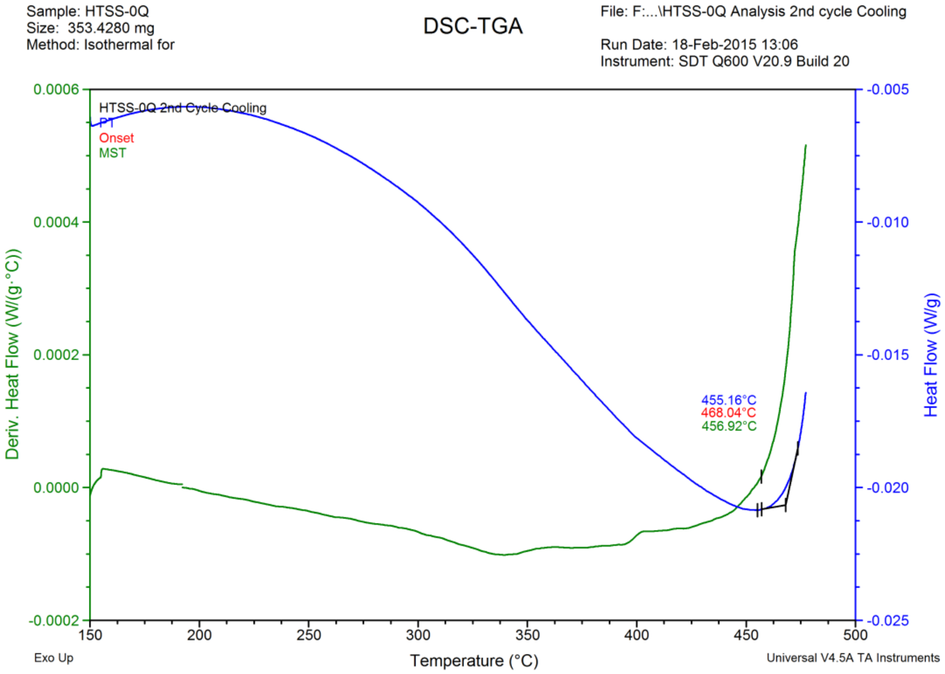

Fig. C.14 HTSS-0Q As received material: cooling curve, Max Temperature 480 °C.

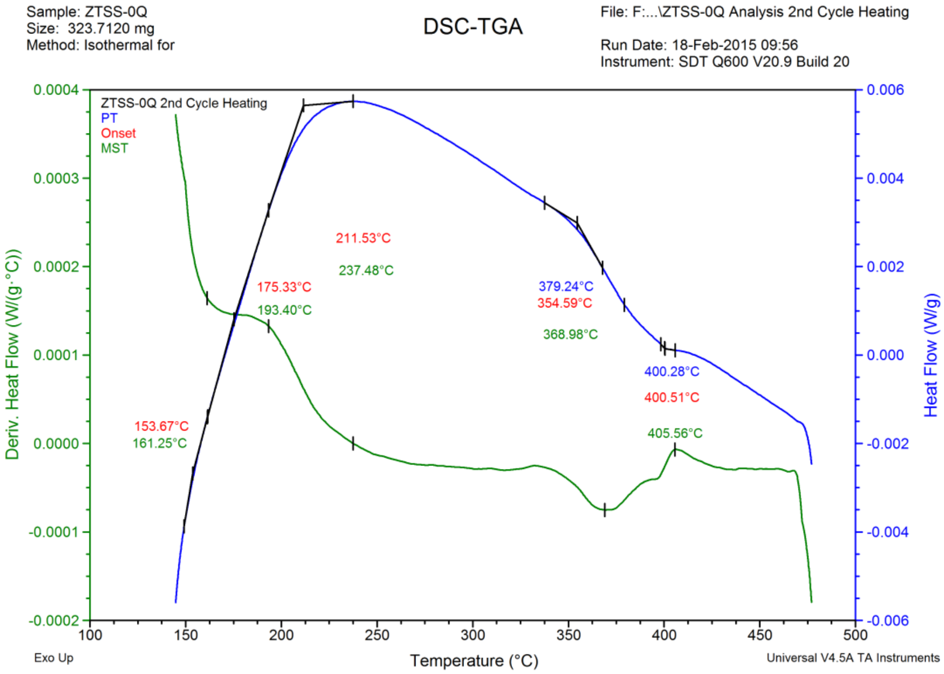

Fig. C.15 ZTSS-0Q As received Material: Heating curve, Max Temperature 480 °C.

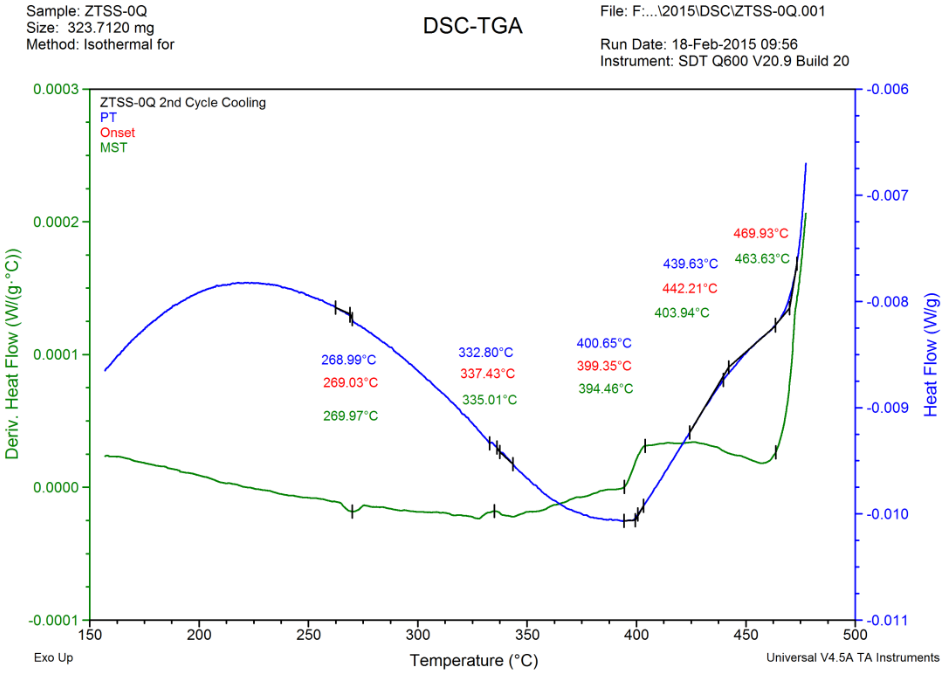

Fig. C.16 ZTSS-0Q As received Material: Cooling curve, Max Temperature 480 °C.

APPENDIX D

SECONDARY ION MASS SPECTROMETRY

Secondary ion mass spectrometry is a useful technique for measuring the concentration of impurities or alloying elements in a material [85]. Zou *et al* used SIMS to measure the solid solubility of iron, nickel, and cobalt in zirconium [85, 86]. Secondary ion mass spectrometry measures the relative intensities of secondary ions, released from material during sputtering. Because it measures relative intensities, correlation to concentration requires standards, of known concentration, throughout the range of measurement. For the hydrogen concentration measurements, the relative intensities measured were the intensities of hydrogen (H) and zirconium-90 (Zr-90). The Zr-90 isotope was chosen because of its low natural abundance, preventing the zirconium signal from overwhelming the spectrometer. Unknown to this author, at the time, is that while SIMS has the capability to detect hydrogen, it is more difficult to measure than other elements. Calibrating SIMS for hydrogen is difficult; because, the yield of H^+ ions from sputtering decreases with increasing sample mass [87]. This increases the necessity for reliable standards to make quantitative SIMS measurements.

The lack of proper calibrations contributed to the failure of the hydrogen concentration measurements, attempted via SIMS. The need for standards was recognized, and prior to attempting the measurements, an attempt was made to procure certified zirconium hydride standards from another laboratory. This attempt failed as certified standards were not available. As a substitute, reference samples were created from our own material. Uncharged material would be used as a low hydrogen reference, and a small piece the sample sent to IMR for hydrogen measurement was reserved as a high hydrogen reference. It was assumed that this section contained an equivalent hydrogen concentration to the specimen measured by IMR, from which it was taken just prior to measurement. Based on the hydrogen measurements by IMR, the reference samples had hydrogen concentrations as shown in Table D.1.

Table D.1

Hydrogen Concentration of SIMS Refereces

Reference	Wt%	wppm
Low Hydrogen	0.001	10
High Hydrogen	0.16	1600

The SIMS measurements were carried out in the HANA-4 HDT samples, after HDT measurements with the Netzsch DSC. Two samples were measured in separate sessions, later all three samples were measured together under the same beam conditions. The two separate measurements were performed on HTSS-1 and HTSS-2. In both cases, the sample recorded a significantly lower relative intensity of H/Zr_{90}, than the low hydrogen reference. As hydride formation and the presence of hydride phases were confirmed in these samples prior to SIMS measurement, it is not possible for the samples to have a lower H concentration than the uncharged reference sample. This would require removing some of the residual H left over from initial fabrication, as well as all the hydrogen that was charged into the sample with the LCS. Results from these two measurements are given in Table D.2.

Table D.2

Results of Early SIMS Measurements.

HTSS-1	I_H	I_{Zr90}	I_H/I_{Zr90}	H wppm
High Ref	23969.6	696.1	34.4	
Low Ref	2993.0	273.3	10.9	
Sample	593.4	1741.2	0.341	
HTSS-1	I_H	I_{Zr90}	I_H/I_{Zr90}	H wppm
High Ref	8207.2	383.9	21.4	
Low Ref	1500.7	183.1	8.2	
Sample	233.2	1558.2	0.15	

When all three samples were measured together, HTSS-2 was measured twice, once returning a lower H concentration than the low reference, and once a higher concentration. This sort of inconsistency resulted in the SIMS measurements being discarded. Data for these measurements are given in Table B.3, and plots of measurement results are given in Figure D.1 and Figure D.2. The lower value for

HTSS-2 was plotted, as a concentration for the higher result was not calculated by the SIMS operator.

Table D.3

Final SIMS Measurements

Sample	I_H	I_{Zr90}	I_H/I_{Zr90}	H wppm
High Ref	320,000	750	426.7	1600
Low Ref	3900	200	19.5	10
HTSS-1	7200	2850	2.5	18
HTSS-2 I	1700	1800	0.94	4
HTSS-2 II	3300	1800	1.8	N/A
HTSS-3	7500	2200	3.4	19

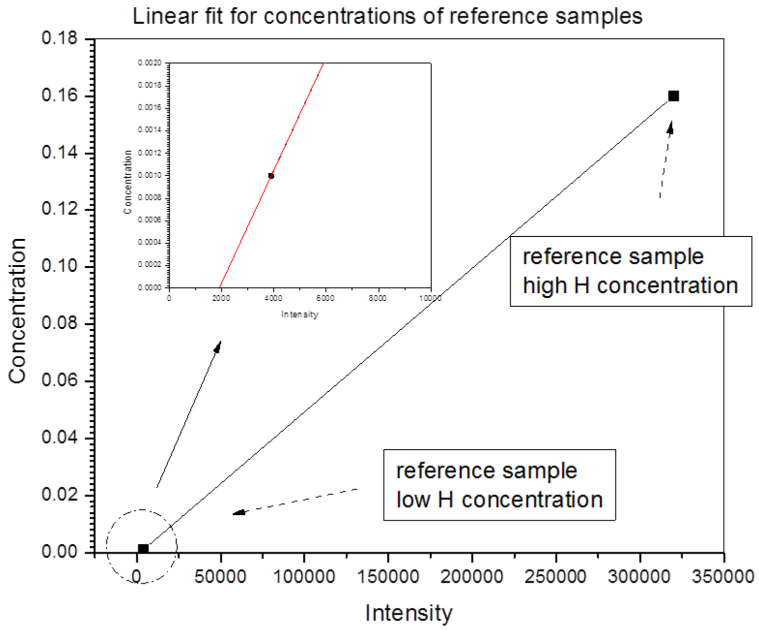

Fig. D.1 Low and high hydrogen references.

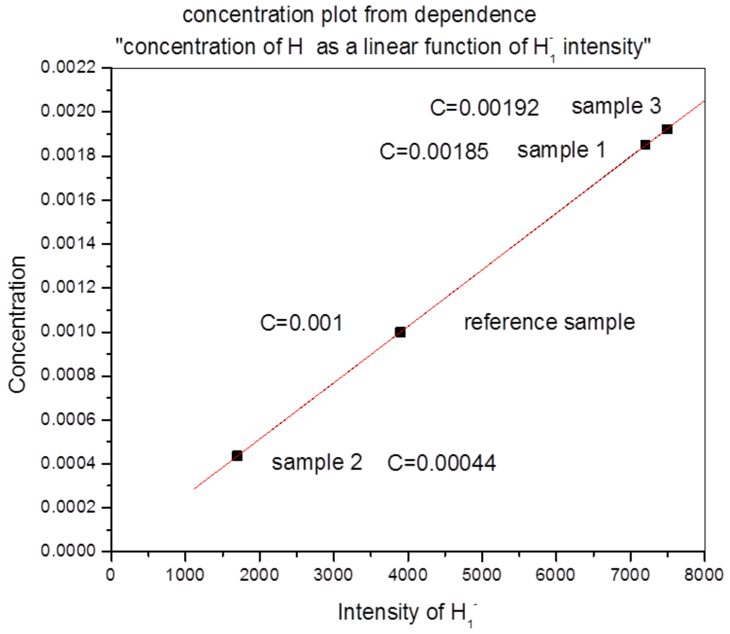

Fig. D.2 Measured intensity for samples.

APPENDIX E

LEVEL SWITCH DIAGRAM

E.1 Level Switch Design